DEFECT CHARACTERIZATION IN AISI 316 L SS USING PULSED AND LOCK IN THERMOGRAPHY

By

SHARATH D
(Enrolment Number: ENGG02200804030)

From

Indira Gandhi Centre for Atomic Research, Kalpakkam

A thesis submitted to the
Board of Studies in Engineering Sciences

In partial fulfillment of requirements

For the Degree of

DOCTOR OF PHILOSOPHY

of

HOMI BHABHA NATIONAL INSTITUTE

February, 2014

Homi Bhabha National Institute

Recommendations of the Viva Voce Board

As members of the Viva Voce Board, we certify that we have read the dissertation prepared by **Sharath D** entitled " **Defect characterization using Pulsed and Lock in Thermography**" and recommend that it may be accepted as fulfilling the dissertation requirement for the Degree of Doctor of Philosophy.

Date: 10 Sept. 2015

Chairman – **Prof. T. Jayakumar**

Date: 25/8/15

Convener – **Prof. U. Kamachi Mudali**

Date: 25/8/15

Technical Advisor – **Prof. B. Venkatraman**

Date: 25/8/15

Member - **Prof. Shaju K. Albert**

Date: 25/08/2015

Member – **Prof. Saroja Saibaba**

Date: 24/Sep/2015

External Examiner – **Prof. Suneet Tuli**

Final approval and acceptance of this dissertation is contingent upon the candidate's submission of the final copies of the dissertation to HBNI.

I hereby certify that I have read this dissertation prepared under my direction and recommend that it may be accepted as fulfilling the dissertation requirement.

Date: 25/8/15

Guide - **Prof. U. Kamachi Mudali**

STATEMENT BY AUTHOR

This dissertation has been submitted in partial fulfillment of requirements for an advanced degree at Homi Bhabha National Institute (HBNI) and is deposited in the Library to be made available to borrowers under rules of the HBNI.

Brief quotations from this dissertation are allowable without special permission, provided that accurate acknowledgement of source is made. Requests for permission for extended quotation from or reproduction of this manuscript in whole or in part may be granted by the Competent Authority of HBNI when in his or her judgment the proposed use of the material is in the interests of scholarship. In all other instances, however, permission must be obtained from the author.

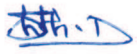

(Sharath D)

DECLARATION

I, hereby declare that the investigation presented in the thesis has been carried out by me. The work is original and has not been submitted earlier as a whole or in part for a degree / diploma at this or any other Institution / University.

(Sharath D)

List of Publications arising from the thesis

Journal

1. "Defect depth quantification using Pulsed Thermography", D. Sharath, M. Menaka and B. Venkatraman, *Advanced Materials Research,* **2012,** *585***,** 72-76
2. "Defect characterization using Pulsed and Lock in Thermography: A comparative study", D. Sharath, M. Menaka and B. Venkatraman, *Journal of Non Destructive Testing and Evaluation***, 2012** *11,* 58-63
3. "Defect characterization using Pulsed Thermography", D. Sharath, M. Menaka and B. Venkatraman, Journal of Non Destructive Evaluation**, 2013,** *32,* 134-141
4. "Effect of defect size on depth quantification in Pulsed Thermography", D. Sharath, M. Menaka and B. Venkatraman, *Measurement Science and Technology,* **2013,** *24*, 125205 1-7
5. "Defect depth quantification using lock-in thermography", Delanthabettu Sharath, Murugesan Menaka, Balasubramanian Venkatraman, and Baldev Raj, Quantitative InfraRed Thermography Journal, **2015,** *12,* 37-52
6. "Debond detection in coatings using advanced imaging techniques", D. Sharath, M. Menaka, Saju T. Abraham, B. Venkatraman and U. Kamachi Mudali Communicated to *Journal of Non Destructive Evaluation*
7. "Lock in Thermography for defect sizing", D. Sharath, M. Menaka and B. Venkatraman, Communicated to *Infrared Physics and Technology*

Conferences

1. **D. Sharath**, M. Menaka, B. Venkatraman and N. Raghu, “Quality assurance of micro coatings using Lock in Thermography”, Presented at **National Seminar and Exhibition on Non Destructive Evaluation**, Dec 7-10, 2011, Chennai
2. **D. Sharath**, M. Menaka and B. Venkatraman, “Defect depth quantification using Pulsed Thermography,”, Presented at **International Conference on Advances in Materials and Processing – Challenges and Opportunities**, Nov 2-4, 2012, IIT Roorkee
3. **D. Sharath**, M. Menaka and B. Venkatraman, “Effect of defect size on depth quantification using Pulsed Thermography”, Presented at **National Seminar and Exhibition on Non Destructive Evaluation**, Dec 10-12, 2012, Delhi
4. **D. Sharath**, M. Menaka and B. Venkatraman, “Quantitative characterization of coatings using Pulsed Thermography”, Presented at **OPE 2013**, Feb 13-16, 2013 Mahabalipuram
5. **D. Sharath**, M. Menaka and B. Venkatraman, “Lock in Thermography for Defect Detection and Depth Quantification”, Presented at **Asia Pacific Conference on Non Destructive Testing**, Nov 18-22, 2013, Mumbai
6. Menaka, M., **D. Sharath**, B. Venkatraman, and Baldev Raj, "Defect Depth Detectability in Austenitic Stainless Steel by Lock in Thermography”, Present at The **12th International Conference on Quantitative InfraRed Thermography**, July 7-11, 2014, Bordeaux, France
7. **Sharath D**, Ajay Rawat, Menaka M and Baldev Raj, “Effect of Air-Gap Thickness on Debond Detection in Coatings using Pulsed Thermography: A

Numerical Study", Presented at **The 1st QIRT-Asia 2015 Conference**, July 07-10, 2015, Mahabalipuram, India

(Sharath D)

DEDICATED TO MANKIND

(Sharath D)

ACKNOWLEDGEMENTS

My first debt of gratitude must go to my technical advisor, *Prof. B. Venkatraman,* for his valuable guidance and making this research possible. The freedom given by him to put forward my idea and work on it, his advice and continuous support throughout the research work is much appreciated.

I would like to express my immense gratitude to my convener, *Prof. U. Kamachi Mudali*, for his continuous support and guidance. He has been strong and supportive supervisor to me throughout the research work.

I convey my sincere gratitude to my doctoral committee chairman, *Prof. T. Jayakumar* for his constructive criticism, extensive discussion and valuable advice regarding my work. I also thank my doctoral committee members *Prof. Shaju K. Albert* and *Prof. Saroja Saibaba* for their continuous support and valuable suggestions during the research work.

I would like to thank *Dr. Baldev Raj, Shri S. C. Chethal* (Former Directors, IGCAR) and *Dr. P. R. Vasudev Rao*,(Director, IGCAR) for their constant encouragement and support during the research work.

My sincere thanks to *Shri. Anandapadmanabhan* (Head QAD) for his constant support and encouragement during the research work.

I would like to thank *Prof. M. Saibaba* for his support and providing pleasant accommodation facility.

I would like to express my immense gratitude to *Mrs. Menaka M*, whose advice and insight was invaluable to me. The time she has spent on my thesis correction is much appreciated.

I take this opportunity to thank *Mr. N. Raghu, Mr. K. Krishna Chaitanya* and *Mr. C. Muniyandi* for their help in radiographic experiment and interpretation and *Mr. Saju T. Abraham, Mrs. D. Chitra, Mr. D. Kuppusamy* and *Mr. Murugan* for helping me in ultrasonic testing.

My sincere thanks to my fellow friend *Mr. Siva Srinivas Kolukula* whose valuable inputs and help in developing MATLAB program is much appreciated. I also thank

Mr. Santosh Pandya and *Dr. Govindaraj* from IPR, Gandhinagar for their valuable discussion on thermal imaging.

I would like to thank my lab mates *Mr. Srinivasan N, Mrs. Kani* and *Miss K. Vani* who made friendly working environment. I would like to thank other Quality Assurance Division colleagues who gave good support.

The support from friends is important for happy and enjoyable life. I take this opportunity to thank my batch mate friends, *Mr. Bubathi Muruganantham, Mr. Sri Mahavishnu, Mr. P. Ilaiyaraja, Mr. Laxmoji, Dr. Jammu Ravi, Mr. Mariyappa, Mr. Jagadeesh Sure, Mr. Naveen, Mr. Herojit, Mr. Sudhanshu, Mr Pradeep Kumar Samantaroy, Dr. Maneesha, Dr. Priyada, Miss. Prawathi and Mrs. Debasmitha*. I also like to thank my friends, *Mr. Shashwath, Mr. Subrato, Mr. Manas, Dr. V. Srihari, Dr. Pandian, Mr. Arunbabu, Mr. Navtesh, Mr. Santhan, Mr. Srijan, Mr. Ravikirana, Mr. Anil, Mr. Ashutosh, Mr. Ravi,* and *Mr. Shailesh* for their constant support and encouragement. I also thank other senior and junior friends for being there with me and making lively environment.

At last, but not the least, I express by sincere and deep gratitude to my father, *Mr. D. Narayana Rao,* my mother *Mrs. Usha N. Rao,* my sister *Mrs. Shilpa R. Rao* and my wife *Mrs. Anusha Rao* for their unconditioned love and care. Without the encouragement, care and help of my parents, I would have not finished this thesis. A special thanks to my dear wife for her support and patience during the final stage of my thesis.

(Sharath D)

CONTENTS

SYNOPSIS

It is well realized that all the engineering materials have defects and one of the principle uncertainties is the performance of material/ component in the presence of defects. The defects can be present in the raw materials itself or can be introduced during various stages of processing and fabrication or environmental and loading conditions during transport, storage and service. While some defects are harmful and hence unacceptable, some are harmless and can be permitted. It is quite possible that few of the unacceptable defects if left undetected can prove to be catastrophic. Thus the quality of the product should be monitored at every stage of manufacturing and during service to make sure that it is free from unacceptable defects. This monitoring should be done in such a way that it does not impair the functionality or service performance of the product. Non Destructive Testing (NDT) or Non Destructive Evaluation (NDE) as the name imply, is the technology of assessing condition and performance of material, component or structure without impairing its functional properties.

In the early days, the primary purpose of NDT was detection of defects and components identified with defects were often removed from service. The advent of fracture mechanics concepts in 1970's changed this scenario. A new design philosophy called damage tolerant design came into existence. In this, components having known defects could continue to be used as long as it could be established that these defects would not grow to a critical size that could result in catastrophic failure. It thus became possible to accept structures with defects provided defect size could be monitored to ensure that it is well within the safe limits. Hence mere detection of flaw was not enough. It was necessary to characterize the defect and obtain quantitative information about its size, shape, and location so that this could serve as an input to fracture mechanics calculations for predicting the remaining life of the component. This need was particularly strong in the nuclear, defense and space

industries. This led to evolution of Non Destructive Testing (NDT) to Non Destructive Evaluation (NDE) as a new discipline. NDE refers to quantitative inspection in which the defect is not only detected but also characterized with respect to its size, shape, and orientation. Today a number of research programs have evolved all over the world in the field of NDE.

The main advantages of applying NDT for material inspection during manufacturing process and for in service inspection are that it ensures product quality, reliability and safety, aids in optimum product design, controls manufacturing process to within specified tolerances, ensures uniform quality levels and customer satisfaction, predicts impending failures, thus preventing costly shutdowns and aids in plant life extension.

A wide range of industries/professionals use NDT methods. To name a few: nuclear, aerospace, automotive, chemical, defense, electronics, electrical, fabrication, fertilizers, food processing, marine, medical, metals, petrochemicals, power, security, surface transport. The success of NDT depends on the combination of qualified personnel, calibrated equipments, documented practices, standard procedures and codified acceptance criteria.

Forming the core of NDE are six basic methods: Visual Testing (VT), Liquid Penetrant Testing (LPT), Magnetic Particle Testing (MPT), Radiography Testing (RT), Ultrasonic Testing (UT) and Eddy Current Testing (ECT) [1].

It is well-established that temperature and its distribution is one of the most important manifestations of the state of components and plants in service. The magnitude and distribution of the temperature are indicators of departure from normal / acceptable performance. This non-destructive test method, which maps the temperature of the object, is referred to as infrared (IR) imaging or thermal imaging or thermography. Thermal imaging or thermography is the mapping of temperature profiles on the surface of

the object or component. It makes use of the infrared band of the electromagnetic spectrum. Infrared refers to a region of the electromagnetic spectrum between the visible and microwave. The IR spectrum extends from 0.75 μm to 1000 μm. The properties of infrared radiations are similar to other electromagnetic radiation such as light. They travel in straight lines; propagate in vacuum as well as in liquids, solids and gases. They can be optically focused and directed by mirrors and lenses. The laws of geometrical optics are valid for these also. The energy and intensity of infrared radiation emitted by an object primarily depend on its temperature and can be calculated using the analytical tools such as Wien's law, Planck's law and Stefan Boltzmann law. Detailed review of the physical principles and the varied applications can be had from references [2-5].

IRT as a nondestructive test method evolved after World War II when industries recognized this as a potential tool for condition monitoring applications. Method was qualitative, used for judging the state of bus bars in electrical industries, to inspect refractory lines in process industries etc. Advent of IR sensors, coupled with advances in instrumentation and electronics saw the transformation of this method to a quantitative one. Advances in active techniques led to its wide spread applications in the field of defect detection and materials characterization. Today IR imaging NDE is one of those few NDE methods that have applications cutting across all industries, research and society, ranging from astronomy, military, medical, energy audit, surveillance, condition monitoring, materials characterization etc.

The main advantage of IRT is that it is non contact method. It enables the inspection of in service components which are not accessible. The output is an image which is easy to interpret. Inspection rate is fast in IRT and it gives real time information. Despite these advantages, like other techniques, it has limitations. The main limitation is the emissivity. To get the absolute temperature and accurate information, the emissivity of

inspecting component should be known. Also IRT is limited for subsurface defect detection.

IR imaging basically exploits the non – equilibrium thermal state within a material for the detection of defects. This non equilibrium state can be achieved through the use of sources which can heat or cool the body. Such sources can be located within the material itself or can be external to it. Thus, two approaches or techniques are generally recognized in thermal NDE – passive and active.

Passive technique involves applications where the material already contains its own internal source of heat. Majority of the condition monitoring applications where the component themselves get heated up due to a variety of reasons fall under this category.

Active techniques involve the application of an external thermal perturbation (heating or cooling) to the object as a whole or of a small area of interest within the object. While both heating and cooling can be applied, it is heating, which is generally preferred. A variety of stimulation sources has been used such as hot air guns, incandescent and flash lamps, lasers, plasma arcs, inductive heating, heating strips, etc.

Main techniques in active thermography are Pulsed Thermography (PT), Lock in Thermography (LT), Pulse Phase Thermography (PPT), Vibrothermography, Step Heating or Time Resolved Infrared Radiometry (TRIR).

In PT, a short and high energy pulse from a flash lamp impinges on the surface of the object. The surface absorbs the light energy and surface temperature increases instantaneously. After the impulse, decrease in surface temperature is recorded using an IR camera. Defects present inside the object will have different thermal signatures from those of the surrounding area due to the thermal resistance offered by defects for heat flow which could be detected using IR camera. PT has been successfully applied for defect detection and depth quantification in ceramics, polymers and composites. PT also finds

application in coating thickness evaluation and debond detection in coatings. In particular, Thermal Barrier Coatings have been successfully evaluated using PT [6]. Several methods have been proposed for defect depth prediction using PT. Most commonly used methods are temperature contrast method [7], contrast derivative method [8], log first derivative method [6] and log second derivative methods [9]. All these methods involve measuring the peak time of temperature response curve which is a function of defect depth.

In LT, a continuous and modulated light source is used to heat the surface of the testing object. The resultant surface temperature variation is monitored using an IR camera. The defective area will have change in amplitude as well as time lag (phase) when compare to sound area. The amplitude and the phase information at each pixel are extracted to get the amplitude and phase image using Four Bucket Method or Fast Fourier Transform. Generally, phase image gives better depth information and is independent of emissivity and surface roughness variation [10]. Blind frequency is one of the issues which need to be addressed carefully. Blind frequency, is the frequency where the phase lag of defective and sound area becomes equal. Hence one cannot differentiate the defect from the sound region. But blind frequency could be used for depth quantification since this frequency is a function of defect depth [11]. Another method used for depth quantification is phase contrast method, where phase angle difference of sound and defective area is computed. Phase contrast is a function of defect depth.

In UT, near surface defects, which falls under the ‘dead zone’ cannot be detected and in RT the depth quantification is an issue. IRT can detect surface and subsurface defects and IRT has the advantage of being non contact technique, which makes it possible to inspect components which are not accessible and components which are in hazardous area. Safety is an important issue in nuclear and other industries. Codal specifications are more stringent in nuclear industries, since components have to work in harsh environment

like high temperature, pressure and radiation. Hence there is a need to inspect the structural materials before and after manufacturing and during the service of the component. IRT is a suitable technique for such inspections.

India has adopted 3 stage nuclear programs to overcome the energy crisis where closed fuel cycle is adopted instead of open fuel cycle. As a part of 2^{nd} stage program, fast breeder reactors are being commissioned in India. Breeder reactors generate new fissile or fissionable material at a greater rate than it consumes such material. In fast breeder reactor fast neutrons are used and sodium, gas or lead is used as coolant. In the commissioned Fast Breeder Test Reactor (FBTR) and upcoming Prototype Fast Breeder Reactor (PFBR), sodium is used as coolant. The operating temperature of the reactor varies between 673 K and 973 K [12]. Sodium imposes a potential corrosion problem where as high temperature operating condition imposes creep, fatigue and mechanical strength problems on the structural materials used in the reactor. Hence, a suitable candidate structural material has to be used for FBRs. Stainless Steels are most preferred due to their excellent corrosion resistance and good high temperature mechanical strength and creep resistant properties. These steels are widely used as structural materials in nuclear and process industries. In a reactor, Stainless Steel materials of different grades (AISI 304 L, 304 L(N), 316 L, 316 L(N), Alloy D9) are used as structural materials for components like, vessel, heat exchanges, clad and wrapper [13].

During fabrication, conventional and advanced NDE methods and techniques such as radiography, conventional ultrasonic, phased array, liquid penetrant testing etc are adopted for defect detection. In cases of thin walled weldments such as Hexcan, apart from the subsurface defects, defects open to surface, such as tight cracks that can be formed due to a variety of reasons, needs to be detected. Conventional techniques like fluorescent penetrant testing are time consuming and if penetrants are not cleaned,

residues can cause corrosion. Pulse echo UT cannot detect due to dead zone and immersion UT is the solution. However with the fuel inside, this is not recommended. Hence, an alternate and reliable technique is needed which can characterize the defect completely. IR imaging offers an excellent possibility for detection of surface and subsurface defects.

A review of literature reveals that extensive work has been carried out on the application of PT and LT for defect detection and depth quantification in composite, concrete, ceramic [14-17]. Defects such as impact damage, cracks etc have been evaluated using PT and LT in these materials. However, its application for metals especially stainless steel is very limited.

The present work focuses on a systematic study of defect detection, depth quantification and defect sizing in AISI type 316 L SS material using PT and LT through modeling and experimental validation. The experimental aspects of PT and LT, defect detectability limits, depth quantification method, their efficiency, limitations of the techniques are discussed in detail. The effect of defect size and shape plays an important role in thermal NDE, as the defect size has direct relation to defect detectability limit. Hence study of effect of defect size and shape on defect detectability and depth quantification has been studied which has not been reported earlier. Hence this study focuses on complete defect characterization in AISI type 316 L SS using PT and LT.

The thesis is organized into 6 chapters. Chapter 1 dwells briefly on defects, their significance, role of NDE and NDE methods. A detailed literature review of IR imaging, especially PT & LT, motivation of the study and scope is also presented. In Chapter 2, theoretical aspects of thermal imaging, PT & LT techniques, experimental set up and numerical tools used in the present work are discussed. In chapter 3 and 4 defect characterization using PT and LT is discussed in detail. Chapter 5 gives the comparative

study of PT and LT for defect detection and few case studies are discussed. Chapter 6 focuses on conclusion and future direction.

Chapter 1: Introduction

In this chapter a brief introduction to materials process and defects is given. Different types of defects and their cause are discussed. The role of NDE in the industry with some application is discussed. A detailed discussion of methods in NDE, their abilities and limitation are given. Then a review on passive and different techniques in active IRT is done. A detailed literature survey is provided quoting the important works carried out using PT and LT by the peers and the current international scenario. Based on the literature review, the motivation of the work is discussed.

Chapter 2: Thermal Imaging: Theory And Experimental Approach

In this chapter, the basic governing laws in IR radiometry, the instrumentation of IR camera, factors affecting the measurement, principle and theoretical background of PT and LT are discussed. Details of material chosen for characterization and the experimental set up details are discussed. The material chosen for experimental study is AISI type 316 L SS. The parent material is qualified using radiography and UT techniques. Then defects of different depth, size and shape are machined using Electro Discharge Machining (EDM). The technical specification of IR camera and the software used are discussed. An IR camera (Silver 420) is used for recording thermal images and Altair software is used for analysis. For theoretical calculations, MATLAB software is used and for numerical simulations ThermoCalc 6L software is used. ThermoCalc 6L software is developed by Prof. Vavilo to solve active thermography problems using finite difference scheme. Using

ThermoCalc 6L software one can solve only parallelepiped shaped defects. The detailed experimental aspects of PT and LT are discussed.

Chapter 3: Defect Characterization using Pulsed Thermography

In this chapter detailed study of defect characterization using PT is discussed. Four commonly used methods for depth prediction, Temperature contrast, Contrast derivative, Log first derivative and Log second derivative methods are considered for analysis. Principle of each method is discussed in detail. Since the analysis involves taking second derivative, which leads to noisy data, a noise reduction technique is required. Thermal Signal Reconstruction (TSR) technique [18] is adopted for noise reduction in PT data. In PT, the appearance of defect in thermogram is a function of time, i.e. near surface defects appear earlier than the deeper defects. This principle is used in to quantify defect depth by measuring the peak time of response curve which is a function of defect depth. Calibration plot in each method is generated with defects of known depth. Then efficiency of the methods for depth prediction is evaluated by predicting the depth of unknown defect using the calibration plot. Then the effect of defect size and shape on the peak time is studied. A one dimension analytical modeling is carried out to understand the heat diffusion around the defect, which is an important parameter which affects the peak time measurement. Another aspect of defect characterization is defect sizing. In PT, as the time passes defect size, in the thermogram, decreases due to the diffusion of heat around the defect. Hence correction factor needs to be considered to measure the accurate size of defect [19].

Chapter 4: Defect Characterization Using Lock in Thermography

LT is carried out on the sample at different frequencies to evaluate the defects which are present at different depths. The concept of phase contrast, blind frequency and phase

inversion is discussed in detail. Phase contrast and blind frequency are used for depth quantification. A one dimensional analytical modelling is carried out using Bennett and Patty model [20]. This model is used to obtain the proportionality constant which is used to predict the depth using blind frequency. Good correlation is not observed between analytical and experimental results. Study of effect of defect size and shape revealed that blind frequency varies depending upon defect size and shape. Another method discussed for depth quantification is phase contrast method, where phase contrast is computed by taking phase angle difference between sound and defective area, which is a function of defect depth. This calibration plot is used to predict the depth of unknown defect. Effect of defect size and shape on phase contrast is studied and it is observed that defect size and shape affects phase contrast. Then a new method is evolved for depth quantification which is independent of defect size and shape. Then sizing of defect is discussed which is done by plotting a line profile over defect and by measuring the Full Width at Half Maximum (FWHM).

Chapter 5: Defect Characterization Using PT and LT – A Comparative Study and Case Studies

In this chapter a comparative study of PT and LT is done. The defect detectability limit in both the techniques is compared. The important parameters compared are Signal to Noise Ratio (SNR) which defines the visualization of defects and defect sizing. Two important case studies related to nuclear industry have been discussed. First the debond detection in coatings using PT and LT are discussed. Debond is a common defect in coating systems. Both the techniques successfully detected debond. The quality of bonding and quantitative information on debond area is obtained from experimental results. Results are validated using UT immersion C scanning technique. Another study taken up is brazing quality

inspection of Plasma Facing Components (PFC) which is used in fusion reactor. The specimen is inspected using PT, LT, Eddy current Thermography and hot and cold simulation. LT gives more information regarding the brazing quality while PT did not give all the information. To get more details, TSR is carried out on PT data and second derivative image is reconstructed which reveals all defected tiles.

Chapter 6: Conclusion and Future Direction

In this chapter, the thesis is concluded and the future direction is discussed. In PT, Contrast derivative method and Log second derivative method are most suitable for depth quantification since in these cases, the peak time does not affect by defect size and shape. But contrast derivative method needs a reference area hence log second derivative method is best for depth quantification in PT. In LT, blind frequency and phase contrast are used for depth quantification. Blind frequency as well as phase contrast is affected by defect size and shape. A more generalized method is discussed using phase contrast where more generalized parameter, defect depth to defect area, is defined for depth quantification which is independent of defect size and shape. Future direction should focus on the application of PT for in service inspection of components for defect detection based on the experience got through lab scale experiments. In LT, further study has to be done for understanding the blind frequency and more generalized inverse method for depth quantification. Numerical studies also should be carried out on LT technique.

REFERENCES

[1] R. Halmshaw, Non Destructive Testing, Edward Arnold, London (1987)

[2] Xavier P. V. Maldague, Patrick O. Moore, Infrared and Thermal Testing, Series: Non Destructive Testing Handbook, Vol 3 (2001)

[3] B. Venkatraman, M. Menaka, P. Kalyanasundaram, Baldev Raj, Journal of Non Destructive Testing & Evaluation, 5 (2006) 54-67

[4] Richard D. Hudson Jr., Infrared System Engineering, John Wiley and Sons (1969)

[5] M. Vollmer, K. P. Mollmann, Infrared Thermal Imaging Fundamentals, Research and Applications, Wiley-VCH (2010)

[6] S. K. Lau, D. P. Almond, P. M. Patel, J. Phys. D: Appl. Phys. 24 (1991) 428-436

[7] S. K. Lau, D. P. Almond, J. M. Milne, NDT&E Int. 24 (1991) 195-202

[8] Harry I. Ringermacher, Raymond J. Archacki Jr, William A. Veronesi, US Patent No. 5,711,603 (1998)

[9] Steven M. Shepard, US Patent No. 6,516,084 (2002)

[10] G. Busse, Appl. Phys. Lett. 35 (1979) 759-760

[11] G. Giorleo, C. Meola, A. Squillace, Res. Nondestr. Eval. 12 (2000) 241-250

[12] Baldev Raj, Energy Procedia 7 (2011) 186-198

[13] S. C. Chetal, P. Chellapandi, P. Puthiyavinayagam, S. Raghupathy, V. Balasubramaniyan, P. Selvaraj, P. Mohanakrishnan, Baldev Raj, Energy Procedia 7 (2011) 64-73

[14] V. Vavilov, X. Maldague, B. Dufort, F. Robitaille, J. Picard, NDT&E Int. 26 (1993) 85-95

[15] J. G. Sun, J. Heat Tranf. 128 (2006) 329-338

[16] G. Busse, D. Wu, W. Karpen, J. Appl. Phys. 71 (1992) 3962-3965

[17] Takahide Sakagami, Shiro Kubo, Infrared Phys. Techn. 43 (2002) 311-316

[18] Steven M. Shepard, James R. Lhota, Bruce A. Rubaduex, David Wang, Tasdiq Ahmed, Opt. Eng. 42 (2003) 1337-1342

[19] M. B. Saintey, D. P. Almond, J. Phys. D: Appl. Phys. 28 (1995) 2539-2546

[20] C. A. Bennett. Jr., R. R. Patty, Appl. Opt. 21 (1982) 49-54

List of Figures

List of Tables

List of Abbreviations

BP	Bannet and Patty
ECT	Eddy Current Testing
FFT	Fast Fourier Transform
FMTWI	Frequency Modulated Thermal Wave Imaging
FOV	Field Of View
FPC	Four Point Correlation
FWHM	Full Width at Half Maximum
IR	Infrared
IRT	Infrared Thermography
LPT	Liquid Penetrant Testing
LT	Lock in Thermography
MPT	Magnetic Particle Testing
NDE	Non Destructive Evaluation
NDT	Non Destructive Testing
NEP	Noise Equivalent Power
PPT	Pulsed Phase Thermography
PFC	Plasma Facing Component
PFM	Plasma Facing Material
PT	Pulsed Thermography
RT	Radiographic Testing
UT	Ultrasonic Testing
VT	VibroThermography

List of Symbols

A_d	Sensitivity Area of the Detector
B	Spectral Radiance
c	Velocity of Light
c_p	Specific Heat
D	Defect Size
D^*	Specific Detectivity
e	Thermal Effusivity
f	Frequency
h	Plank's Constant
h_{cv}	Convection Heat Transfer Coefficient
H	rms Value of Fundamental Component of the Irradiance on the Detector
k	Boltzmann Constant
K	Thermal Conductivity
L	Defect Depth
Q	Heat Flux
R	Reflection Coefficient
Rs	Responsivity
S	Square Root of Defect Area to Depth Ratio
t	Time
t_c	Peak Contrast Time
t_s	Peak Contrast Derivative Time
t_p	Peak Log First Derivative Time
t_2	Peak Log Second Derivative Time
T	Temperature
V_s	Rms Value of the Fundamental Component of the Signal Voltage
x	Depth
α	Thermal Diffusivity
ε	Emissivity
λ	Wavelength

μ	Thermal Diffusion Length
ρ	Density
σ	Stefan Boltzmann Constant
ω	Angular Frequency

CHAPTER 1
INTRODUCTION

1.1 Materials and Defect

Materials form an inseparable part of our day to day life. Apart from metals, various kinds of materials like, polymers, ceramics, composites and semiconductors, have been innovated and being used for a wide variety of applications. The materials are extracted from the ore and then the desired property and shape are given to them through various fabrication processes to enable its use as structural components. Any structural material and component has limited life. At the end of this life period, the component deteriorates and ultimately fails. No material is perfect. All materials have defects some of which are inherent (present in the raw material), some induced due to the fabrication (processing defects) and some due to service (service defects). Defects can be either linear such as cracks, lack of penetration, lack of fusion etc or volumetric such as porosities, voids, blow holes etc. They can be either near the surface or deep within. While volumetric defects are primarily considered as reducing the wall thickness, linear defects such as cracks are considered to be the most dangerous as they can propagate under service conditions. The life of the material or component is primarily influenced by the type, size, shape and number of defects. With greater stringency of specifications coupled with lower safety factors and longer expectations of life, detection of defects through appropriate inspection technologies at various stages right from raw material through fabrication, pre service inspection and in-service inspection has thus gained importance. This inspection should be done in such a way that it does not impair the functionality or service performance of the product but ensures its fitness for purpose. This is best

achieved through the judicious application of Non Destructive Testing and Evaluation methods.

1.2 Non Destructive Testing and Evaluation

Non Destructive Testing (NDT) is a method of inspecting the material to ensure its fitness for purpose without impairing its usefulness. The primary purpose of NDT is to evaluate the existing state or quality of a material with a view to acceptance or rejection. While NDT can be considered to be age old (potters used tapping methods – acoustic emission to ensure integrity of pots), emphasis on NDT developed more during the Second World War for military applications. With the rapid advent of industrialization, NDT gradually found its application in the field of medical and industries for condition management and inspection of materials. Over the years, the science and technology of NDT has matured to greater extent. In the early days, the primary purpose of NDT was detection of defects. Critical parts were manufactured with design concept of "Safe Life" design. The detection of defects during service was automatically a cause for removal of component from the service. The advent of fracture mechanics concepts in 1970's changed this scenario. A new design philosophy called damage tolerant design came into existence. In this, components having known defects could continue to be used as long as it could be established that these defects would not grow to a critical size that could result in premature or catastrophic failure. It thus became possible to accept structures with defects provided defect size could be monitored to ensure that it is well within the safe limits. A new demand was thus placed on NDT community. Mere detection of defect was not enough. It was necessary to characterize the defect and obtain quantitative information about it's size, shape, and location so that this could serve as an input to fracture mechanics calculations for predicting the remaining life of the component. This need was

particularly strong in the nuclear, defense and space industries. This led to emergence of Non Destructive Evaluation (NDE). NDE refers to quantitative inspection in which the defect is not only detected but also characterized with respect to its size, shape, and orientation. The advances in sensor technology coupled with modeling and simulation helped the evolution of NDE from NDT which was mere go no go test. NDE today is a multi disciplinary technique finding wide application in almost all facets of science, engineering, technology and society. The typical applications sector is depicted in fig. 1.1.

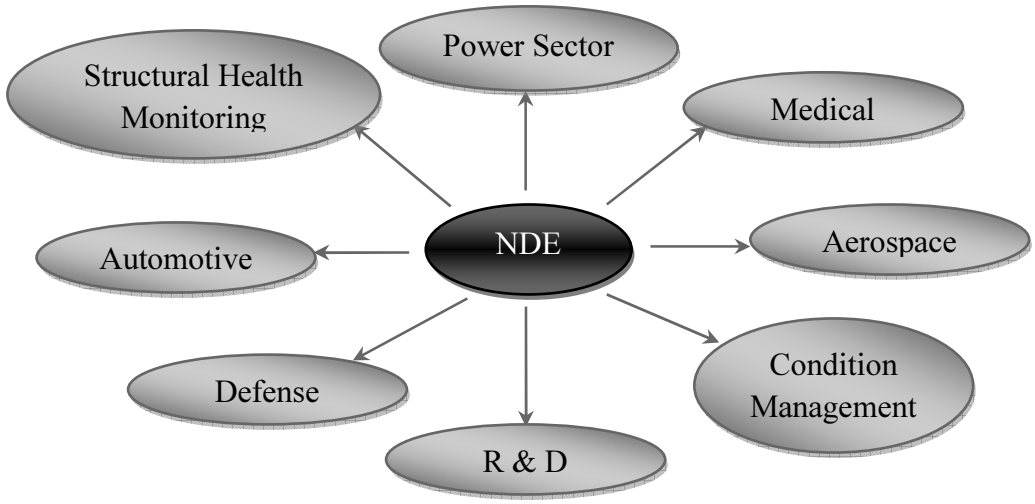

Figure 1.1: Schematic diagram of the application of NDE in different fields

Apart from application areas, within a particular sector such as manufacturing, NDE is applied right from design validation stage through fabrication, pre-service and in-service inspection. In short right from the cradle to retirement NDE is an indispensable tool. Any NDE technique should be cost effective, must detect defects, their type, size and location and distinguish between those which are harmful, bearing in mind the service condition involved. In NDE, the defects we are talking are micro and macro defects only. We are not primarily concerned about dislocations and lattice imperfections. The principle of any NDE technique involves the application of inspection medium (acoustic, magnetic,

radiation etc) to the testing object. The applied medium is modified by interacting with the discontinuities in the object which is detected using suitable sensors. The detected medium is converted into suitable signals which are processed, evaluated and interpreted by the inspector. The schematic diagram of the NDE principle is shown in fig. 1.2.

The benefits of NDE are listed below.

- NDE methods and techniques help in preventing wastage of material, manpower and shop time.
- NDE identifies the region of mechanical stress, fatigue failures and helps in preventing failure of vital equipments thus increasing the service life of components.
- Safety: Using NDE helps in preventing accidents, loss of life and property.

NDE also helps in sorting different materials, differentiating physical and metallurgical properties of materials.

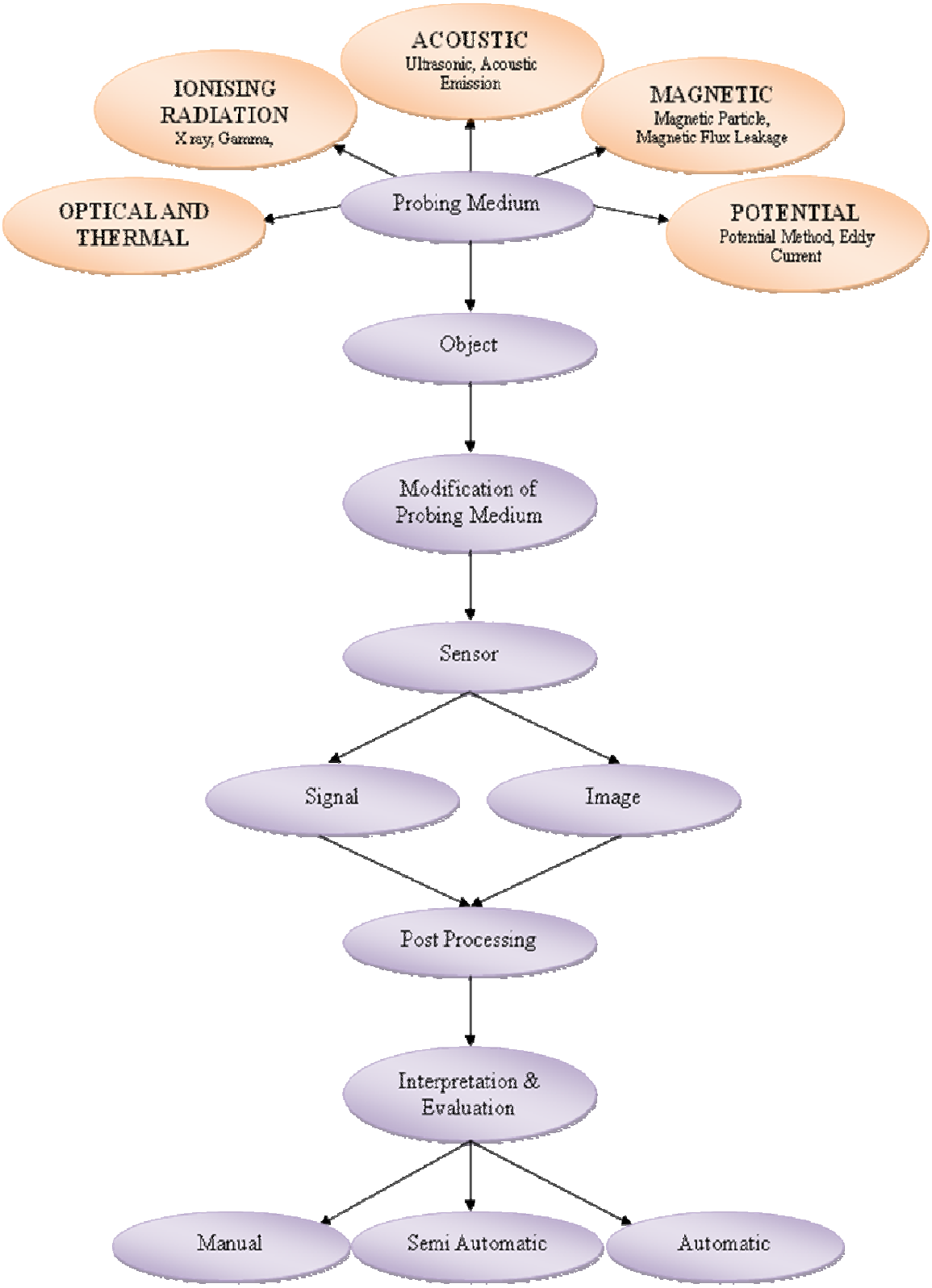

Figure 1.2: Schematic diagram of principle of general non destructive inspection

1.3 NDE Overview

The most commonly used NDE methods are Ultrasonic Testing (UT), Radiographic Testing (RT), Liquid Penetrant Testing (LPT), Visual Testing, Magnetic Particle Testing (MPT) and Eddy Current Testing (ECT). Each technique is based on a different principle and it has its own advantages, limitations and specific applications. Table 1.1, summarizes the principle, advantage and limitations of some of the widely used NDE methods [1-4].

NDE Technique	Principle	Advantage	Disadvantage
Visual Testing	Illumination of the object with light and examination of the reflected light. Optical aids are used	Simple, Non-Contact, Cost effective	Limited to surface defects only
Liquid Penetrant Testing	Applying dye (penetrant) on the cleaned object surface, after the dwell time, dye is removed, then developer is applied to draw the penetrant out of discontinuity (bleed out). The surface is examined with eye and / or with the aid of visible or ultraviolet light	Simple. Capable of detecting tight surface cracks. Portable. Can be used in field also. Cost effective	Suitable for defects open to surface only. Qualitative. Rough and porous materials cannot be examined.
Magnetic Particle Testing	Magnetic flux is confined inside the material, when a ferromagnetic material is magnetized. The discontinuity (surface and sub surface) causes local magnetic flux leakage which is detected by sprinkling finely divided magnetic particles	Suitable for surface and subsurface defects. Cost effective and portable,	Only ferromagnetic materials can be inspected, Demagnetization required
Ultrasonic Testing	Ultrasound, generated using transducers, travels through the material and reflects from the back side with reduced energy. Discontinuity will reflect the ultrasonic wave	Detects linear defects, Real time results, Good accuracy	Contact technique, Dead zone limits the detection of near surface defect, Interpretation of

	back to surface which is detected using a receiver		signal requires skill
Radiographic Testing	It is based on the application of X ray or Gamma ray on the testing object, the intensity of the outgoing radiation is modified due to the absorption in material. Defects will have different absorption property than surrounding causing differential absorption of radiation which is detected on the other side of the sample	Good for volumetric defects. No surface preparation.	Hazardous, Both side access required, Depth quantification is difficult
Eddy Current Testing	Alternate current in coil (probe) generates alternate magnetic field, when another conductor is brought near the coil, the alternate magnetic field induces current in conductor (Eddy Current). EC produces its own magnetic field which opposes the primary magnetic field causing changes in resultant field thus coil impedance which is read in CRT. Defect present in material affect the resultant magnetic field.	Minimum sample preparation, Non contact technique	Only conducting materials can be examined, Low penetration depth

Table 1.1: List of NDE techniques, principle, advantage and disadvantage

Each method and technique has its own advantage and limitation. LPT is limited for surface defects, UT is contact technique, dead zone limits the near surface defect detection and output is signal which is tedious to interpret, RT is hazardous and depth quantification is not possible, MPT, MFL and ECT are limited for particular type of materials. It should be emphasized here that no single NDE method is capable of detecting all types of defects. That is why in industries complementary NDE methods are adopted. This thesis focuses on infrared thermography (IRT).

1.4 Infrared Thermography

Infrared Thermography (IRT) has become popular NDE technique due to its ability to inspect non invasively, fast inspection rates and provide a visual image which is easy to interpret. IRT started as a condition monitoring tool in electrical and process industry. The advances in sensors, electronics and imaging devices resulted in equipments with better resolution and thermal sensitivity, leading to wider range of application such as material characterization, tensile deformation studies, online weld monitoring, thermal diffusivity measurements, defect detection etc. While predictive condition management using IRT is based on passive thermography, materials characterization utilizes active thermography. Passive technique involves applications where the material already contains its own internal source of heat. Majority of the condition monitoring applications where the component themselves get heated up due to a variety of reasons fall under this category. Active techniques involve the application of an external thermal perturbation (heating or cooling) to the object as a whole or of a small area of interest within the object. While both heating and cooling can be applied, it is heating, which is generally preferred. A variety of stimulation sources have been used such as hot air guns, incandescent and flash lamps, lasers, plasma arcs, inductive heating, heating strips, etc. Active thermography is mainly used for defect detection and depth estimation, coating thickness evaluation etc. Pulsed Thermography (PT), Lock in Thermography (LT), Pulsed Phase Thermography (PPT), Vibro Thermography and Step Heating are the some of the techniques used in active thermography [5]. The external stimuli used to excite the material are optical, mechanical, ultrasound, eddy current, hot and cold simulation etc. Figure 1.3 shows a typical classification of IRT techniques.

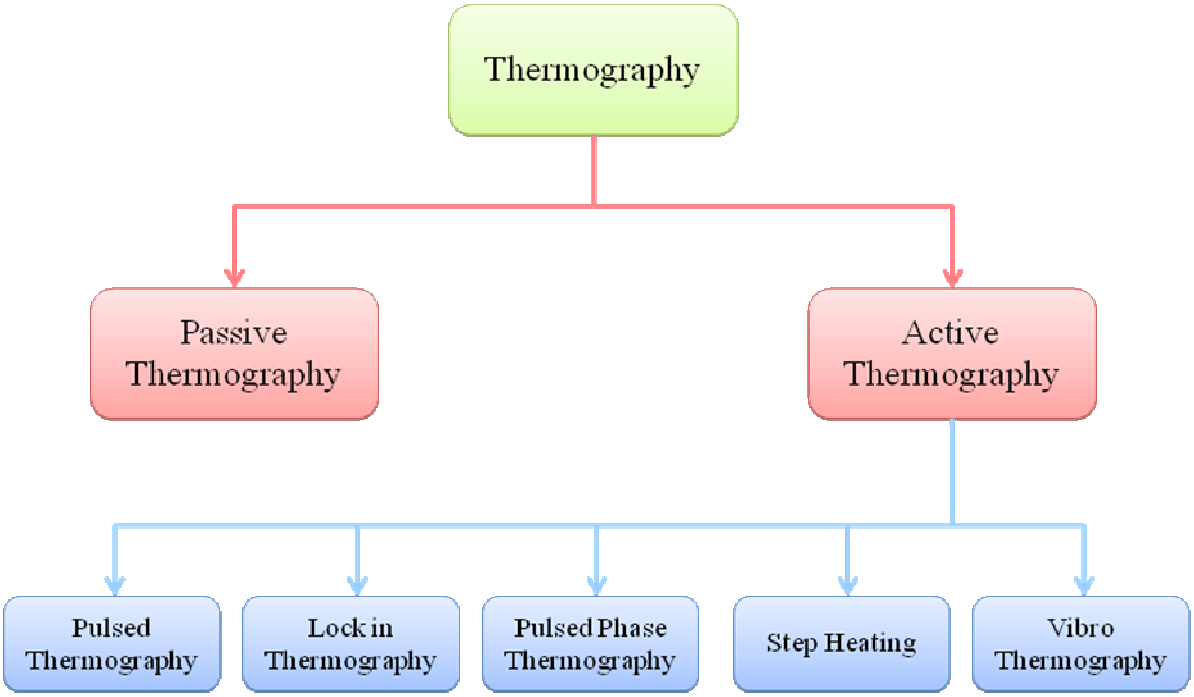

Figure 1.3: Infrared Thermography Techniques

In the following section, the principles of IRT techniques are discussed briefly.

1.4.1 Passive Thermography: In passive thermography, the natural heat distribution of the object is mapped using an IR camera. The inspecting component must be at higher temperature than the ambience. This is used mainly in electrical industries for inspecting the electrical transformers, energy audit, military applications, liquid level measurements, leakage detection etc. In passive thermography one should take care of emissivity variation, reflections from the surrounding, sunlight, relative humidity and ambient temperature which influence temperature measurement.

1.4.2 Active Thermography: In active thermography external stimulus is applied to disturb the equilibrium of the object with the ambience. The external stimulus could be optical light, mechanical vibration, hot or cold air and water jet etc. The defective area has different thermal response when compared to non defective area thus making it to detect

using an IR camera. Techniques used in active thermography, their principle are discussed in brief [5-7].

1.4.2.1 Pulsed Thermography: In Pulsed Thermography (PT), a short and high energy light pulse is impinged on the testing material. The front surface of the material absorbs the light energy causing instantaneous increase in surface temperature. The surface temperature is recorded using and IR camera either from same side (reflection mode) or from back side (transmission mode). The front surface temperature decreases continuously while increase in temperature is observed at back side. When a defect is present, it alters the diffusion of thermal waves causing change in surface temperature which can be detected using the camera.

Advantage: Fast inspection rate and easy

Limitations: Non uniform heating

Emissivity variation

1.4.2.2 Lock in Thermography: In Lock in Thermography (LT), a continuous, sinusoidal light source of single frequency is used to heat the surface of testing object. The surface temperature of the object also modulated with the same frequency as the heating source. This change in temperature is monitored using an IR camera. Then the input and output waves are compared to get the amplitude and the time lag information. The defective area will have different amplitude and phase value when compared to non defective area. To get the amplitude and phase images, algorithms like Fast Fourier Transform (FFT) or Four Point Correlation (FPC) are used. Phase image is not sensitive to emissivity variation and surface irregularities and it gives more depth information than amplitude image.

Advantage: Phase image is independent of surface roughness and emissivity

More depth information

Limitation: Long inspection time

1.4.2.3 Pulsed Phase Thermography: Pulsed Phase Thermography (PPT) combines the advantages of both PT and LT. In PPT, the testing material is exposed to short pulse, like PT and the temperature decay is recorded using IR camera. Mathematically, a pulse can be decomposed into a multiple of individual sinusoidal components. Hence, when a specimen is pulse heated, thermal waves of various amplitude and frequencies are launched into the specimen at a time. Using mathematical tools such as Fourier transforms, one can go back and forth between temporal frequency domains. one can perform the FFT on the temperature history and phase and amplitude information can be obtained for the desired frequency. Thus one can get the advantage of PT (fast inspection) as well as LT (more depth information and independent to emissivity variation).

Advantage: Fast inspection rate

More depth information

Limitation: Application of oscillatory basis functions to represents the transient response

1.4.2.4 Vibro Thermography: In Vibro Thermography (VT), mechanical or ultrasonic vibration is applied to the material and the mechanical energy is converted into heat energy leading to increase in surface temperature which is detected using an IR camera. In VT, the heat is generated within the material. The mechanical vibration activates the heat sources near the damaged regions, making it possible to image tight cracks (Defect select imaging). The excitation in Vibrothermography could be done in two ways, pulsed and frequency modulated excitation.

Advantage: Closed and narrow cracks could be detected

SNR over defect would be very good, since heat is generated in defect

Limitation: Mechanical vibration may lead to the damage of material

SNR of non defective region is poor since no heat is generated

1.4.2.5 Step Heating: In Step Heating, sometimes referred to as long pulse thermography or time resolved infrared radiometry (TRIR), the sample is heated using a step heating pulse and the resultant surface temperature response is recorded using an IR camera. The heating source could be optical, microwave or induction sources.

1.4.2.6 Frequency Modulated Thermal Wave Imaging: In Frequency Modulated Thermal Wave Imaging (FMTWI), the heat sources are modulated at low frequency and the frequency is gradually changed over time creating a chirp signal which leads to non stationary signals. The images are recorded during the modulation. The desired frequency is selected during the post processing and amplitude and phase images are then obtained. The wavelength varies as a function of frequency in FMTWI which leads to variation in the depth resolution which helps in detection of defects at different depths, in one frequency modulation cycle.

1.5 Infrared Thermography: International Scenario

It was Sir Frederick William Herschel's curiosity that led to the discovery of infrared rays in 1800. In his historic experiment, Herschel was trying to measure the temperature of individual colors of visible light. He used a prism to split the light into constituent colors and placed blackened thermometer on each color. It was observed that the temperature increased from violet to red. Just out of curiosity, he placed the thermometer beyond the red light and for his surprise he observed the temperature was higher than any of the color. Herschel concluded that there exists energy band beyond red wavelength and he called it as Infra (beyond) red radiations. The research carried out showed that IR radiations, though invisible to human eye, obeys the laws of reflection, refraction and diffraction as visible light [8, 9]. Though the IR rays were detected in early

19th century, they have been utilized for NDE applications in late 20th century. This was possible due to the development in detectors and instrumentation.

Passive Thermography: Many works have been reported on application of IRT in condition monitoring, medical, military and civil material inspection etc.

Abnormal temperature profiles, in any structural material, indicate a potential problem which must be fixed in order to maintain the controlled process under valid operating conditions.

Passive thermography is widely used for inspecting faulty parts in electrical and machines [10-12]. Since the faulty components offer more resistance to electrical flow or the vibration in machines causes deposition of heat in faulty parts which could be detected using an IR camera. Based on the experience a guide has been developed by American Society for Testing and Materials (ASTM) for inspecting electrical and mechanical equipments [13]. Printed Circuit Board (PCB) inspection is another area where IRT finds application. The faulty parts of the PCB, which has higher temperature, can be detected using an IR camera, during the fabrication as well as during service [14, 15]. IRT has been used for inspecting the variation in blade temperature and delamination in turbine blades [16, 17]. Online welding monitoring using IRT has been successfully studied. IRT has been used for sensing, in process control of heat affected zone and cooling rate in arc welding process [18-20]. The depth penetration study and bead width measurement in different type of welding process using IRT has been reported [21-23]. IRT has been used for determining the quality of weld in different welding techniques [24-26]. Inspection of civil structures like, bridges and building using IRT is well reported in literature. The inspection of bridges for delamination detection using IRT has been carried out and ASTM procedure has been developed for this purpose [27-29]. IRT has also been used for

insulation inspection of building, locating wet areas in insulated roofing, inspection of cultural heritages etc [30, 31]. IRT finds important application in the medical field. The metabolic activity in human body causes temperature rise in body. Deviation in temperature from average human body temperature is the indication of abnormality. IRT is widely used for detection of breast cancer at early stage [32, 33]. The cancerous cells will have higher metabolic activities than the normal cells leading to higher temperature of cancerous cells. Worldwide, IRT is used as screening tool in breast cancer detection. Another important application of IRT in medical industry is in the area of early detection of diabetes [34, 35]. The other application of IRT in medical field involves screening tool for SAARS detection, to study tear film in dry eye, to study diseases related to skin (dermatology), to study the healing rate of wounds etc [36-38]

Pulsed Thermography: PT was initially used to measure thermal properties of different materials. Then this technique was used to evaluate coating thickness and defect detection and depth quantification.

Thermal Diffusivity Measurement: Parker et al has proposed a new method for measuring the thermal properties (conductivity, diffusivity) of materials using flash method [39]. Analytical modeling was carried out and the result showed that time for half temperature rise and thermal diffusivity are related. The sample which was coated with black paint was heated using a short heat pulse and the temperature is recorded at the rear surface using a thermocouple and oscilloscope. The temperature time plot was used for determining the thermal diffusivity of the material. Research has been carried out on the application of flash method for determining the thermal diffusivity of materials at high temperature by considering the effect of heat loss due to convection and radiation which are effective at high temperature [40]. Further research was carried out for correction of finite pulse time

effects and a mathematical model was proposed for correcting the errors due to finite duration of pulse and application of it on thin sample with high diffusivity [41]. Many other works has been reported on thermal diffusivity measurement using PT [42-45].

Coating Characterization: Another important application of PT is coating thickness evaluation and debond assessment. Much work has been reported on coating thickness evaluation of Thermal Barrier Coatings (TBC).

P. Cielo has proposed a method for evaluating layered materials using pulsed photothermal technique [46]. The authors have discussed the mechanism in evaluating the well bonded coatings and delaminated coatings. D. L. Balageas et al have explained the theory of pulsed photothermal technique applied to layered materials [47]. The analytical theories of both two and three layered sample were discussed. Then the results of the model were compared with the existing data. A coating thickness quantification method was proposed by S. K. Lau et al using PT [48]. Log first derivative plot was considered for analysis and the peak derivative time, which is a function of thickness, was used for coating thickness measurement. Experimental aspects of determining thin metallic coatings were discussed by U. Netzelmann et al [49]. The authors have used frame rate of more than 1 KHz for inspecting Copper and MCrAlY coatings, on Nickel based alloys, of thickness 37 to 300 μm ranges. For thin coatings pulse of short width with fast shut off behavior have to be used.

Number of work has been reported on the application of PT for delamination detection in coating system. Golam Newaz et al have assessed the progressive damage of thermal barrier coatings using PT [50]. The authors have subjected the TBC to different thermal cycles and the PT experiment was carried out after some range of cycles to identify the delaminated regions. The study showed that PT could detect the early damage of TBC system. Similar study was carried out by Jeffery I. Eldridge et al. The authors have

used mid wave infrared reflectance imaging for monitoring delamination progress in TBC [51] and observed that imaging at wavelength 4 μm takes advantage of relatively high transmittance. MIR reflectance imaging showed great potential as a diagnostic tool for investigating delamination progress in TBC.

Defect Characterization: Defect detection is another important application of PT. Initially PT was used as qualitative tool to detect defects. Later with better understanding of theory and mechanisms and with improvement in detectors and IR cameras, PT has evolved to quantitative method. Many methods have been developed to quantify defect depth as well as defect size.

Otto Renius has reported the use of Infrared NDT as tool to detect defects in composite, prior to which IRT was used only in military applications [52]. The author has used laser source for heating the sample for short time and recorded the front surface temperature using an IR detector. The work demonstrated the ability of PT for qualitative detection of defects. The author also explained the theoretical aspects. P. V. McLaughlin et al have used thermal NDE technique to evaluate the composite structures [53]. Different aspects which affect the temperature measurement of IR camera like emissivity, conductivity were discussed. A detailed aspect of theory and practice of IR NDT for bonded structure was discussed by V. Vavilov [54]. The author has focused on the sensitivity issues in thermal NDT. The work showed that for deeper defect two sided method is preferable while for near surface defects one sided approach is better. C. M. Sayers has worked on theoretical part of defect detection by thermal NDT [55]. The author has carried out theoretical and numerical analysis of defect detection in one sided as well as two sided inspection. One sided inspection is good for depth quantification while two sided inspection is good for defect sizing.

Many numerical codes have been developed for modelling transient thermography problems. S. F. Burch et al have developed two finite difference codes to model heat transfer in materials by transient thermography [56]. The work focused on the variation of temperature contrast as a function of defect depth and time. The numerical modelling was compared with analytical model and experiment. P. Cielo et al have worked on thermographic NDE of industrial materials [57]. The study includes the defect detection in graphite epoxy laminates, inspection of adhesive bond in aluminium structure, high temperature industrial structures etc. To extract more information, authors have used signal processing techniques in both spatial and time domains. D. L. Balageas et al have used pulsed photothermal method for characterization of carbon epoxy composites [58]. The authors have proposed new method for determining the depth and thermal resistance of defect in composite materials. W. N. Reynolds has carried out study of inspection of laminates and adhesive bonds by pulse-video thermography [59]. Theoretical analysis was done by thermal wave approach which was inspired by Wong et al [60]. Theoretical basis of both two sided and single sided methods were discussed. S. K. Lau et al have studied the quantitative nature of pulsed video thermography on mild steel samples [61]. The authors have considered basic one dimensional approach for understanding the temperature response. To model the response of defects of finite size, an analytical first order theory was developed. V. Vavilo et al have reported the detailed analysis and data processing of carbon epoxy composites using Thermal NDT (TNDT) [62]. The authors have considered both analytical and numerical approach for solving TNDT problems in composites. Based on these modelling the first order and second order parameters which affect the TNDT were derived. The detailed study of depth prediction using PT was carried out by J. G. Sun [63]. His work has been on the ceramic materials. The author has discussed the analytical and experimental part of different methods used to predict the

defect depth which are reported in literature. The efficiency of each method was discussed with merits and demerits. Apart from these, many more works have been reported on defect detection and depth prediction using PT [64-67].

Another important application of PT is defect sizing. A detailed numerical and analytical study was carried out by D. P. Almond et al for defect sizing using PT [68, 69]. The authors have observed that the defect size decreases as time elapses and derived an analytical relationship between Full Width at Half Maximum (FWHM), defect size as a function of time. The detailed experimental investigation of defect sizing by transient thermography and the edge effect on defect sizing is carried out by the same author [70, 71].

Noise is an inseparable part of a signal, the thermal signal are no exceptions. To reduce these noises different methods have been discussed in literature. The most commonly used method is Thermal Signal Reconstruction (TSR) proposed by Shepard et al [72]. In this method a polynomial of higher order is fitted to the temperature data in logarithmic domain at each pixel. The temperature values could be reconstructed by taking exponential of fitted value which is noise free. This method acts as low pass filter and it reduces the storage memory since we required storing only polynomial coefficients. Shepard has proposed a reference free detection method of sub surface defects [73]. In this method the second derivative of log temperature time plot is the computed and plotted as a function of log time. The zero crossing time is a function of defect depth which does not require any reference area. Other works include the application of TSR for turbine blade inspection [74] and defect detection study in ceramic composites [75].

Another method for noise reduction is Principle Component Thermography (PCT). This method was initially proposed by N. Rajic [76]. In this method empirical orthogonal functional analysis is used to decompose the pulsed thermographic data. Singular Value

Decomposition is used to reduce the matrix of observation to a highly compact statistical representation of the spatial and temporal variations relating to contrast information associated with underlying structural flaws. N. Rajic has used PCT for flaw contrast enhancement and flaw depth characterization in composite materials [77]. Vavilov et al have discussed the basics of Principal Component Analysis (PCA) and used it for thermal testing [78]. The application of PCA involved the data averaging over time. The thermograms are simulated using ThermoCalc-3D software and then PCA is carried out over the simulated (pure) thermogram. The analysis showed that the PCA does not ensure the complete separation of noise caused by uneven heating, emissivity variation and directionality of material but it improves the visual perception of IR thermogram by increasing the Signal to Noise Ratio (SNR). PCT has been used to inspect composite materials, corrosion detection in aluminium and hidden moisture determination on microwave heating. C. Ibarra-Castanedo et al have discussed various image processing and data analysis techniques in PT technique [79]. The data analysis methods such as thermal contrast computation, normalization, pulsed phase thermography, PCT and thermal signal reconstruction methods were discussed in preprocessing and post possessing stages. Other works on PCT could be referred here [80-82].

Lock in Thermography: The LT technique has evolved from photoacoustic method.

Photoacoustic Method: This techniques deal with propagation and detection of photoacoustically generated thermal waves inside the material and their interaction with subsurface flaws.

Theory of photoacoustic effect with solids is widely discussed in literature [83-87]. The photoacoustic spectroscopy was used to detect the surface and subsurface defects in silicon nitride ceramic material, which is used in turbine blade manufacture, by Y. H.

Wong wt al [88]. The authors have reported good correlation between the observed photoacoustic signal and surface microstructure. Y. H. Wang et al have given experimental evidence for non destructive detection of surface and subsurface structures in ceramic materials using scanning photoacoustic microscopy (SPAM) [89]. The thickness of the surface layer probed is dictated by thermal diffusion length which is inversely proportional to square root of modulation frequency. R. L. Thomas et al have used SPAM for flaw detection in Aluminium [90]. The experimental results were compared with calculations based on 3 D thermal diffusion model. G. Busse et al have used photoacoustics to image the subsurface flaws [91]. The authors have used piezoelectric device for photoacoustic thermal wave imaging, instead of conventionally used gas microphones. The authors also demonstrated the frequency dependency of phase and amplitude images. G. Busse has used optoacoustic phase angle measurement for probing metal [92]. The author has shown that the optoacoustic phase angle scanning enables precise measurements of subsurface structure in metal. C. A. Bennett et al have discussed the theoretical aspects of interference of thermal waves and photoacoustic effects [93]. The authors have discussed the procedure to extract the thickness or thermal properties of thin film layers using photoacoustic technique. Analytical model was developed to calculate the relative phase and amplitude of thermal waves in thermally thin materials.

Photothermal Method: The above mentioned methods depend on the detection of photoacoustic signals caused by thermal waves propagating inside the material. G. Busse has used photothermal method for probing a metal in transmission mode [94]. In photothermal method, instead of photoacoustic signal, the temperature variation of sample is monitored using Golay cell, which detects the IR radiation. The main advantage of photothermal technique is that, it is non contact technique.

The theoretical and experimental aspects of photothermal radiometry were discussed in detail by Per-Erik Nordal and Svein Otto Kanstad [95, 96]. The physics of thermal waves, theoretical background and experimental part with SNR analysis was discussed in detail. The comparison between optoacoustic and photothermal techniques was studied by G. Busse [97]. In photothermal transmission imaging, the physical contact of detector and sample is not required. But depth resolved analysis is not possible since all parts of the sample contribute equally to the signal. On the other hand, in optoacoustic imaging mostly near surface regions contribute to the signal thus allowing depth profile. But there is loss of depth range and resolution. The photothermal technique was used to inspect adhesives, coatings and fiber reinforced polymers by G. Busse et al [98].

Mirage Effect: Apart from optoacoustic and photothermal techniques, another method used for measuring the optical and thermal properties of material is photothermal deflection (Mirage Effect). This method was initially proposed by A. C. Boccara et al [99]. When a sample is periodically irradiated by a beam of monochromatic light, its surface exhibits a periodic change in temperature. This temperature gradient gives rise to a refractive index gradient suitable for periodically deflecting a probe beam propagating along the surface temperature field. The magnitude of deflection is then related to the absorption coefficient of material. The detailed theoretical aspects of Mirage effect was discussed by J. C. Murphy et al [100]. The authors have discussed both thermal and optical aspects in Mirage effect and used this effect for photothermal spectroscopy and to measure the thermal diffusivity of gases. Further work on photothermal measurement using Optical Beam Deflection (OBD) was carried out by L. C. Aamodt et al [101]. The authors have developed a criterion for photothermal saturation appropriate to localized optical absorption. The application of photothermal spectroscopy and photothermal imaging using OBD on heterogeneous sample was studied by L. C. Aamodt et al [102].

The work focused on heterogeneous samples whose thermal and optical properties vary slowly relative to a sample thermal diffusion length. The effect of thermal conductivity, optical absorption coefficient and thermal capacity on photothermal signal was studied. The spatial resolution aspect of thermal wave microscopes for non destructive applications using mirage effect was discussed by L. J. Inglehart et al [103]. It is shown both theoretically and experimentally that the resolution of thermal wave microscope is not necessarily limited by the thermal wavelength. If the subsurface features are close to the surface as compared to the thermal wavelength, the intrinsic resolution is independent of wavelength and determined by depth of features. Mirage effect was successfully used for defect detection in welding [104]. A simple 1 D theoretical model was carried out for understanding the variation of phase and amplitude with normalized thickness and the results were confirmed by 3 D modeling.

Lock in Thermography: The advances in IR detector technology have led to the Focal Plane Array based detectors, which has reduced the job of raster like scanning.

Lock in thermography was initially developed by Busse et al [105], where the sample is heated using halogen lamps and the temperature modulation caused by periodic input light, is recorded using IR camera. Then a Four Point Correlation method is used to obtain the phase and amplitude information at each pixel. The authors have used this method for finding delamination in Carbon Fiber Reinforced Plastic (CFRP).

The advantage and limitations of Standard Lock in Method (SLIM), the 4 Bucket Method (4BM), Variance Method (VM) and Least Square Method (LSM) were discussed by J. C. Krapez [106]. The performances of the algorithm were evaluated through Monte Carlo simulation. Another work, reported by Liu Junyan et al, is focused on the investigation of thermal wave signal processing algorithm to obtain information on subsurface defects [107]. The authors have discussed the Fourier Transform Method (FTM), Four Point

Correlation Method (FPCM), Digital Lock in Correlation Method (DLCM) and a newly proposed Time Constant Method (TCM). The experiment was carried out on ANSI 1045 steel plate as well as CFRP plates with defects. The time required for computation and the SNR in each method were computed and compared. The analysis showed that FPCM is the fastest when compared to others and SNR is better in FTM and TCM.

Apart from analytical modeling many works have focused on numerical modeling of photothermal inspection [108-110].

Coating Thickness Evaluation: Aithal et al have initially reported the use of photoacoustic technique for detection of subsurface defects in coating system [111]. Thermal resistance at the coating-substrate was used to characterize the photoacoustic effect. The thermal effusivity and diffusivity were measured from phase and amplitude information. D. P. Almond et al have applied thermal wave interferometry technique for coating thickness evaluation [112]. The detailed theoretical analysis was carried out using photothermal modeling and correlation with microstructure of coatings was carried out. The particular combination of substrate and coating materials determines the magnitude of the thermal wave reflection coefficient which dictates the overall sensitivity of the technique [113, 114]. P. M. Patel et al have analyzed the air gap and thermal contact resistance defects in steel material [115]. The effect of air gap thickness in both uncoated and coated samples was discussed in detail. The experimental results showed that the 1 D heat flow does not hold good for small defects which are buried deep inside the material. Also for adhesion defects in coatings, the sensitivity becomes more and more complex function involving the thermal properties of both coating and substrate material.

Defect Characterization: The application of LT for CFRP, aircraft material and wood was carried out by D. Wu et al [116]. Defect detection in CFRP, inspection of welded metals, delamination, hidden corrosion in aircraft materials are some of the examples. The work

by G. Giorleo et al is focused on the analysis of defective carbon epoxy by means of lock in thermography [117]. LT could detect the different kind of defects but defects which are located at a depth not exceeding the defect diameter were detected. The authors have proposed method for depth quantification using blind frequency, provided the thermal diffusivity of material is known.

The non destructive evaluation of joints using IRT was reported by Carosena Moela et al [118]. The system considered for study was aluminum adhesively bonded joint, stainless steel laser welded joints and Glare mechanical fastened joints which are used in aeronautical industries. The results were compared with PT results. The study of evaluation of delamination defects in concrete using LT was carried out by Takahide Sakagami et al [119]. Initially the experiment was conducted on artificial delamination defects and then on actual delamination defects. The quantitative estimation of size and location of subsurface defects in AISI 304 SS using LT was done by Manyong Choi et al [120]. The shearing phase technique was employed to measure the size and location of defects accurately. In this method, the image is shifted by certain number of pixels to get a shifted image while the subtraction of one image from the other gives the shearing phase distribution. The difference in the maximum and minimum in shearing phase distribution gives the size of defect while the zero crossing gives the location of defect. Further work was carried out by Liu Junyan et al on the defect size, location and depth estimation using LT [121]. To reduce the noise in phase image, first the phase values are normalized by using the maximum and minimum phase values. Then a heat transfer partial differential equation model is used to filter the noise of normalized phase image, which is then used to perform differential normal phase analysis. For depth quantification ANN approach is used. Stainless Steel and CFRP samples were considered for experiment and defect size, location and depth could be estimated with good accuracy. The effect of defect size on

phase angle measurement in LT was studied by C. Wallbrink et al [122]. Steel specimen with circular defects of varying size and depth was chosen for experiment. It was observed that phase contrast varies as a function of defect size and defect depth. The detectability of defects in phase images was associated with the noise in the image. A finite element analysis was carried out considering the 3 D heat flow effect to provide more accurate results than the analytical models which does not account for convective and 3 D heat loss. The most of the work reported does not account for heat loss due to convection. W. Bai et al have developed the photothermal models for LT under convection condition [123]. The authors have developed the analytical model for single layer and multilayer systems, considering heat loss due to convection. A new parameter is defined called combined coefficients which is the sum of convective and radiation heat transfer coefficient. This model was then used to evaluate defects in CFRP composite material and validated with experimental results [124]. In LT, the signal in steady state is considered for analysis. Work carried out by Sung Quek et al focuses on the utilization of transient signal for defect detection using LT [125]. A robust thermal wave signal reconstruction (TWSR) technique was developed where the hybrid polynomial function is fitted to each pixel in thermographic sequence and the fitted coefficients were used to reconstruct phase and background leveled images. The experiment was conducted on 3 mm thick CFRP sample. Apart from conventional phase image, the 1^{st} and 2^{nd} derivative images were analyzed and it was observed that they probe 43% deeper than phase image. The SNR in transient regime is better than the steady state which gives possibility of early detection of defects. A comparison between PT and LT with matched excitation energy was carried out by Simon Pickering et al [126]. A signal to noise ratio was performed to compare the techniques. Carbon fiber reinforced composites plate containing back drilled flat bottom holes was chosen for experiment. It was observed that for shallower defects PT gave better

SNR than LT but for deeper defects both techniques produces same SNR. Increasing the excitation energy used will increase the SNR in raw data. In PT it has direct effect on defect detectability and it has no effect in case of LT. Further work was carried by Krishnendu Chatterjee et al on comparison of PT, LT and Frequency Modulated Thermography with matched excitation energy [127].

Other Techniques: Vibrothermography is mainly used for detecting tight cracks like fatigue cracks [128]. Debonds or delamination and hidden corrosion also could be detected by Vibrothermography. The mechanisms of vibration energy dissipation on damage are not yet fully understood and the recent work focused on the understanding the source of heat in Vibrothermography [129, 6]. Lock in Vibrothermography was used to inspect the polymer materials for detecting delamination and defects [130]. In this study, water coupled ultrasonic excitation method was used to generate modulated heat. Also Vibrothermography is applied for welding inspection, quantitative assessment of damage in aircraft structure.

PPT was proposed by Maldague et al to combine the advantage of PT and LT and demonstrated its ability to probe deeper defects and its least sensitivity to optical and IR surface disturbance [131]. The experimental aspects of PPT and influence of three-dimensional heat diffusion was discussed in detail [132, 133]. PPT technique was successfully used for depth quantification in different materials like plexiglass, aluminium, CFRP and steel [134-137]. Many methods have been proposed for depth quantification and blind frequency method is most commonly used.

Step heating thermography finds many applications such as for two layers as well as multilayered coating thickness evaluation, inspection of coating to substrate bond or evaluation of composite structures. Inspection of zirconia thermal barrier coating on a super alloy rod was carried out using TRIR. The spallation of the coating was clearly seen

in thermal image. Coating thickness evaluation of yttria stabilize zirconia coating was successfully carried out using step heating and analytical relationship between coating thickness and the peak time is derived which could be used to quantify coating thickness [138]. Hidden corrosion could be detected using step heating thermography. This corrosion limits the life of military and civil aircraft structures. TRIR was used for inspecting the steel plate with epoxy coating using microwave heating. The debond region filled with air and water was inspected and it was easier to detect debond with air gap rather than filled with water. Step heat was used to detect and quantify defects in composite materials [139].

Frequency Modulated Thermal Wave Imaging (FMTWI) has been evolved in the recent years, proposed by Ravibabu Mulaveesala and Suneet Tuli [140, 141]. Work has been reported explaining the theoretical aspects of FMTWI [142]. FMTWI was successfully applied for interface inspection of bonded wafers, defect detection composites and other applications [143-145]. Recent studies focused on improving FMTWI using barker coding, quadratic frequency modulation [146-148].

1.6 Motivation of the Study

Infrared imaging, thermal imaging or thermography is the terms that are used for this fascinating and growing field. No matter what we call it, IR imaging has achieved a status, which very few inspection methods and techniques have attained – a diversity of applications ranging from defect detection to condition management, healthcare applications for early diagnosis to heritage conservation and research. Compared to other NDE techniques, the unique advantages of IR imaging include

a) It is a non-contact method of thermal measurement

b) Online mapping is possible. Thus, with fast scan rate it is possible to map the dynamic thermal transients that occur during testing.

c) It provides a full field thermal image making it possible to visualize specific events and effects

d) Large areas can be scanned easily with high reliability and precision

e) It can be directly applied on engineering components.

Two main areas that have been identified by the author for experimental work in this thesis are

a) Defect detection and characterization by pulsed technique of infrared imaging in austenitic stainless steel, its modeling, validation through experimentation and correlation with complementary NDE methods

b) Comparison of the pulsed method with lock in thermography and validation of the observations through specific case studies

Defects as indicated in the introductory part play a significant role and can be considered as the prime factor for limiting the life of a component. No NDE method is capable of detecting all kinds of defects and in industry, a host of complementary NDE methods are adopted to ensure the quality and reliability of the component. While traditionally industries resort to the conventionally established four methods namely radiography, ultrasonics, liquid penetrant and magnetic particle testing, with increased stringency of specifications and also reduced margins of safety, a need arises for advanced defect selective methods capable of revealing the serious defects such as tight cracks which are difficult to detect by the above mentioned conventional methods. This is especially true in case of strategic industry like nuclear wherein, the material is not only going to be subjected to the harsh environment of high temperatures and pressures but also to the additional factor of X-, gamma and neutron radiation. In cases of components

which are within the core, an additional factor that is to be considered is that they would not be accessible during service and hence repair would be very difficult.

AISI type 316 and 316 L austenitic stainless steel are the most widely used structural material in the nuclear industry due to its excellent mechanical properties such as high corrosion and creep resistance and high temperature strength. Apart from the above its absorption cross section for fast neutrons is also relatively low. This material is also widely used in other industries such as chemical and petrochemical as a structural material. AISI type 316 is used for the fabrication of the hexcan which houses the fuel elements, it is also used as fuel clad [149-150]. These are very critical applications. One of the problems encountered during hexcan welding is the appearance of tight cracks which have been missed by UT. An international review of literature revealed that most of the works focused on application of IR imaging for defect detection and characterization in composites which are widely used in the aerospace industry. Very few works had been reported for AISI type 316 SS or 304 SS. In the field of crack and other defect detection, pulsed and lock in techniques hold promise as they are ideally suited for the detection surface defects.

However, successful exploitation of IR imaging for defect characterization requires detailed characterization studies in the laboratory to establish the basic correlations of IR images and thermal data with the dynamics of the events. Such studies are challenging, due to the multidisciplinary nature of the problems. It is the versatility of IR as an NDE imaging tool, the uniqueness of the problems and their relevance to research and industry, motivation to take on challenges that has triggered the enthusiasm of the author to undertake this work.

Aims and Objectives: PT and LT are widely used for ceramics and composites, but on SS limited works are reported. This thesis focuses on defect characterization in AISI type 316

L SS using PT and LT and defect detection and defect detectability limit in PT and LT are discussed. Thermal signals are greatly affected by the size and shape of the defect, which plays important role in depth quantification. In the real case the size and shape of the defect in structural material is unpredictable. Hence the objective of the present study is also to define depth quantification methods in PT and LT which are independent of defect size and shape. The defect sizing study using Full Width at Half Maximum (FWHM) method is also carried out.

1.7 Structure of Thesis

The thesis is organized in to 6 chapters. Chapter 1 gives brief introduction and overview of NDE. Different IRT techniques are discussed with detailed literature review. The gap areas are discussed and the motivation of the present work discussed. Chapter 2 discusses the theoretical aspects of IRT. Material and experimental approach and theoretical and numerical tools used in the study are discussed. In Chapter 3, defect characterization using PT is discussed. Four methods are used for depth quantification and effect of defect size and shape on them is studied. Analytical and numerical modeling is carried out for validating the experimental results. Chapter 4 focuses on defect characterization using LT. Blind frequency method for depth quantification was discussed and Bennett and Patty model is carried out. Phase contrast method is discussed for depth quantification. Effects of defect size and depth quantification on both the methods are studied. Defect sizing also carried out. In Chapter 5, a comparative study of PT and LT is carried out. Following two case studies are considered. The brazing quality inspection of Plasma Facing Component (PFC) which is used in fusion reactor and debond detection in coatings is carried out using PT and LT. In Chapter 6, the present work is summarized and the future direction is discussed.

CHAPTER 2

THERMAL IMAGING: THEORY AND EXPERIMENTAL APPROACH

A fundamental understanding of the physics of infrared science and technology is essential for the success of any IR based experimentation. This chapter after a brief overview of the fundamental aspects of infrared radiation focuses on the principles of pulsed and locks in thermography. The chapter also dwells on IR imaging systems, their essential performance parameters, numerical tools used in this study, the experimental arrangements and the challenges in experimentation.

2.1 Infrared Thermography: Theory and Instrument

All bodies above absolute zero emit electromagnetic radiations due to the vibration and oscillation of atoms and molecules. The intensity of radiation emitted depends on wavelength and temperature of the body. At ambient temperatures, the wavelength of radiation emitted by the body falls in the IR band of the electromagnetic spectrum. Infrared radiations are electromagnetic radiations with wavelengths ranging from visible (above 0.75 μm) and microwaves (below 1000 μm). They have properties similar to other electromagnetic radiations such as light. They travel in straight lines; propagate in vacuum as well as in liquids, solids and gases. They can be optically focused and directed by mirrors and lenses. The laws of geometrical optics are valid for these radiations also.

In the following sections, the basic laws of radiometry, detector system and system performance parameters are discussed [151-156, 6].

2.1.1 Basic Governing Laws

Planck's Law: This is the basic governing equation of radiometry. Planck's law gives the amount of radiation emitted by unit surface area into a fixed direction as a function of wavelength at a fixed temperature from a black body.

$$B_\lambda(T) = \frac{2hc^2}{\lambda^5} \frac{1}{\exp\left(\frac{hc}{\lambda kT} - 1\right)} \qquad (2.1)$$

where B is the spectral radiance emitted by the blackbody, h is Planck's constant (6.626×10^{-34} m^2kg/s), c is speed of light (3×10^8 m/s), k is Boltzmann constant (1.38×10^{-23} $m^2kgs^{-2}K^{-1}$), λ is wavelength and T is temperature. In fig. 2.1, the spectral response of blackbody at temperature 600 K, 500 K, 400 K and 300 K are shown. From the figure it is observed that maximum energy is emitted at a particular wavelength (peak of curve).

Wien's Displacement Law: Wien's displacement law states that the wavelength of the peak of the emission of the black body is inversely proportional to its temperature. It is expressed as

$$\lambda_{max} = \frac{B}{T} \qquad (2.2)$$

Where λ_{max} is the peak wavelength in meters, T is the absolute temperature of the black body in Kelvin and B is a constant of proportionality called the Wien's displacement constant and has a value of 2.898×10^{-3} mK. The relationship is obtained by differentiating Planck's law with respect to λ and setting the derivative equal to zero. Wein's law tells us that objects of different temperature emit spectra that peak at different wavelengths. Hotter objects emit most of their radiation at shorter wavelengths while cooler objects emit most of their radiation at longer wavelengths. This is depicted in fig. 2.1 which indicates that as the temperature of the black body decreases, the peak

wavelength shifts to longer wavelengths. Wien's law is of practical significance as it helps us to calculate the temperature of objects based on their peak intensity.

Stefan Boltzmann Law: Integrating Planck's law with respect to λ between the limits λ = 0-∞ for constant absolute temperature T, we get the total radiant power emitted into a hemisphere from a body. This is the Stephan-Boltzmann law and is mathematically represented as,

$$B = \sigma T^4 \qquad (2.3)$$

where σ = 5.67×10^{-8} $Wm^{-2}K^4$ is Stefan Boltzmann constant. The Stefan Boltzmann law gives the total energy being emitted by a blackbody at all wavelengths, which is the area under the curve. The above equation indicates that hotter an object more is the infrared radiation it emits.

Emissivity: The laws mentioned above are primarily valid for black bodies. A blackbody is a perfect emitter and a perfect absorber of radiation. That means it absorbs all radiation incident on it, regardless of wavelength. In real case, no objects emit or absorb radiation like a blackbody. Hence we define a parameter called emissivity. Emissivity is a measure of the ability or ease at which an object or surface emits radiation. Emissivity is the ratio of the radiant energy emitted by an object at a temperature T and the radiant energy emitted by a blackbody at the same temperature.

$$\varepsilon = \frac{B_o}{B_{bb}} \qquad (2.4)$$

where B_o is spectral radiance of real body and B_{bb} is spectral radiance of blackbody. The emissivity of a blackbody is 1 and is independent of temperature and wavelength. For real bodies, the emissivity depends on temperature, wavelength, surface finish and angle of emission. In some cases one can assume that there is constant emissivity value for all

wavelengths and such body is called as *gray body.* However the blackbody theory can be applied for real bodies, with introducing the emissivity factors in the above discussed laws. The emissivity of a perfect reflector is 0 and for real bodies, it varies from 0 to 1.

Kirchhoff's Law: Kirchhoff's law states that when an object is at thermal equilibrium, the amount of absorption will equal the amount of emission.

Lambert's Law: The amount of radiant energy from a given surface varies with cosine of the angle from which it leaves that surface.

$$B_\theta = B \cos\theta \qquad (2.5)$$

Where B_θ is the energy emitted at an angle θ and B is the energy emitted at the normal to the surface. The above equation shows that the maximum energy is emitted at a direction, normal to the surface (θ = 0). As the angle increases beyond the normal, the radiation emitted by the body decreases. This is important in IR thermography, since one has to ensure maximum IR radiation reaches the detector to obtain accurate measurements. Hence the detector and the testing surface should be normal to ensure maximum radiation reaches the detector.

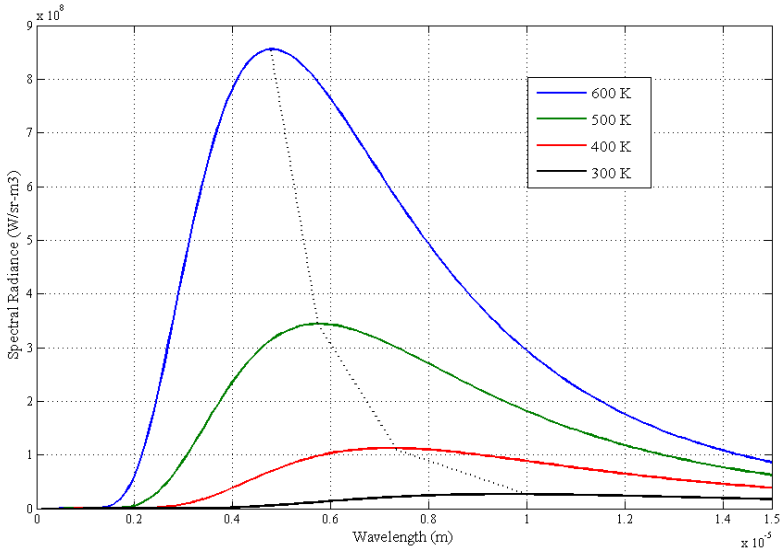

Figure 2.1: Spectral response of a blackbody at temperatures 600 K, 500 K, 400 K and 300 K

2.1.2 IR Imaging System The basic component of an infrared system is an infrared camera. An IR camera consists of lens, detector, cooling system, built in or external temperature reference and display. The IR radiation emitted by the body reaches the camera where a special lens focuses the radiation on to the detector which converts the radiation into electric signal, which is temperature calibrated using internal temperature references. Materials used for IR optics are different from the light optics due to difference in transmittivity of light and IR by the material. Hence IR transparent materials like Germanium, Silicon etc are used as lens material. Before detected by the camera, IR radiation has to pass through the atmosphere which contains water vapor, natural gases like oxygen, nitrogen and other molecules like carbon dioxide, carbon monoxide etc. These gases absorb IR radiations at wavelengths where the vibration frequency of molecules matches with the IR frequency. The atmospheric transmittance of IR is shown in fig. 2.2. It is observed that the IR transmittance through atmosphere is maximum in two windows 3-5 μm, which is called mid wave infrared (MWIR) and 8-14 μm, which is called long wave infrared (LWIR). Hence IR cameras are designed such that it detects either MWIR or LWIR.

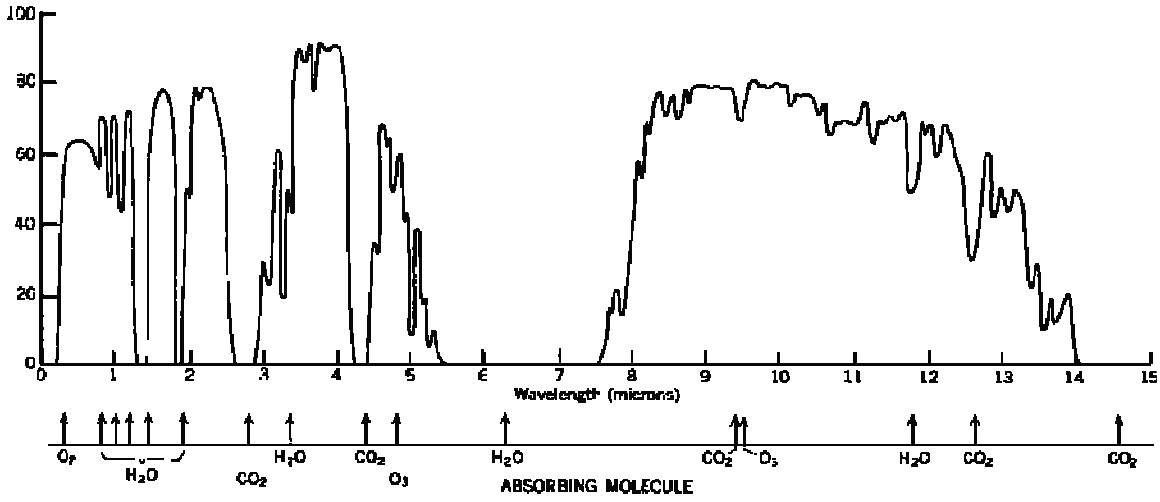

Figure 2.2: Transmission of IR radiation through atmosphere

2.1.2.1 Detector System: Detectors are the heart of IR imaging system. The quality of the detector system determines the performance of the imaging system to a great extent. Detectors generate electrical signals which are proportional to radiation power absorbed by them. There are two general classes of detectors: thermal detectors and photon detectors. The principle, advantage and limitations of these are discussed below briefly.

Thermal Detectors: In thermal detectors, the incident radiation is absorbed to change temperature of the material, and the resultant change in some physical properties such as resistance, thermo-electric voltage is measured.

The main advantage of thermal detector is that they operate at room temperature, are light, rugged and cost effective. But they have a modest thermal sensitivity and a large response time.

The different types of thermal detectors are listed below.

Bolometer: In bolometer, the incident IR radiation is absorbed by an absorptive element which heats the detector causing the change in resistance which is amplified and measured electrically. Different types of bolometer are metal bolometer where, resistance is a linear function of temperature, semiconductor bolometer where, resistance is exponential function of temperature.

Example: vanadium oxide, amorphous silicon etc.

Golay Cell: Golay cell contains a Xenon filled gas chamber and mirror which focuses light energy onto a photocell. Incoming IR radiation is absorbed by an absorptive layer, causing increase in temperature which intern expands the layer. The expansion of gas results in distorting the mirror causing change in light intensity falling on photocell. This change in intensity is related to the incoming IR radiation.

Pyroelectric Detectors: Crystals which do not exhibit center of symmetry, experience an electric field along the crystal axis due to polarization. These crystals are called

ferroelectric crystals and the voltage is a function of temperature. Hence when these detectors are exposed to IR radiation, the temperature change will cause in change in voltage, which is used to measure the temperature.

Example: Triglycine Sulphate (TGS), Lead lanthanum zirconate titanate (PLZT) etc.

Photon Detectors: In photon detector, the IR radiation is absorbed by the material converting the bound electrons to free charge carriers. The change in charge carrier concentration, changes the electrical properties like, voltage or electrical conductivity of the material which is measured to determine the incident power of radiation.

The photon detectors have the advantage of high thermal sensitivity and small response time but are costlier than thermal detectors.

Two types of photon detectors are widely used.

Photoconductive Detectors: In photoconductive detectors, the increase in free carriers, produced by incident radiation, causes increase in electrical conductivity. These detectors are composed of single uniform semiconductor materials.

Photovoltaic Detectors: Photovoltaic detectors consist of p-n junction in a semiconductor. In photovoltaic detectors, electron hole pairs are created due to the incident radiation. The hole and electron diffuses in opposite direction across the junction creating a photocurrent. This photocurrent is a function of temperature.

Example: Lead Sulfide, Indium Antimonide, Lead Selenide etc.

2.1.2.2 Performance Parameters for IR Detectors: Detector, which is heart of the system, has to be evaluated based on some of important performance parameters depending upon the applications for which it is used. Detector performance can be described in terms of various quantities of merit such as responsivity, noise equivalent power and detectivity.

Responsivity: The responsivity is a measure of the transfer function between the input signal photon power and the detector electrical signal output. Responsivity provides information on gain, linearity, dynamic range and saturation level and is given by the following equation,

$$R = \frac{V_s}{HA_d} \qquad (2.6)$$

where V_s is the rms value of the fundamental component of the signal voltage, H is the rms value of the fundamental component of the irradiance on the detector and A_d is the sensitivity area of the detector.

The response time of a detector is characterized by its response time constant, the time that it takes for the detector output to reach 63 % of its final value after a sudden change in the irradiance.

Noise Equivalent Power (NEP): Noise sets limit on the minimum input spectral flux that can be detected under given condition, since noise produces random fluctuation in the output of a detector which can mask the weak signals. Noise equivalent power is the radiant flux necessary to give an output signal equal to the detector noise. Mathematically, NEP is the ratio of root mean square noise and responsivity of the detector.

$$NEP = V_n/R \qquad (2.7)$$

where V_n is the rms value of the noise voltage at the output of the detector.

Specific Detectivity (D^*): To compare the sensitivity of different detectors a parameter called specific detectivity is defined. Specific detectivity normalizes the reciprocal of NEP to a 1 cm^2 detector area and 1 Hz noise bandwidth.

$$D^* = \frac{(A_d \Delta f)^{0.5}}{NEP} \qquad (2.8)$$

The specific detectivity for some of the thermal and photonic infrared detectors is shown in fig. 2.3.

From fig. 2.3, it can be observed that thermal detectors have a wide and flat response curve with low sensitivity where as photon detectors have limited spectral response and higher sensitivity. Thermal detectors usually operate at room temperature and photon detectors are to be cooled to optimize their performances.

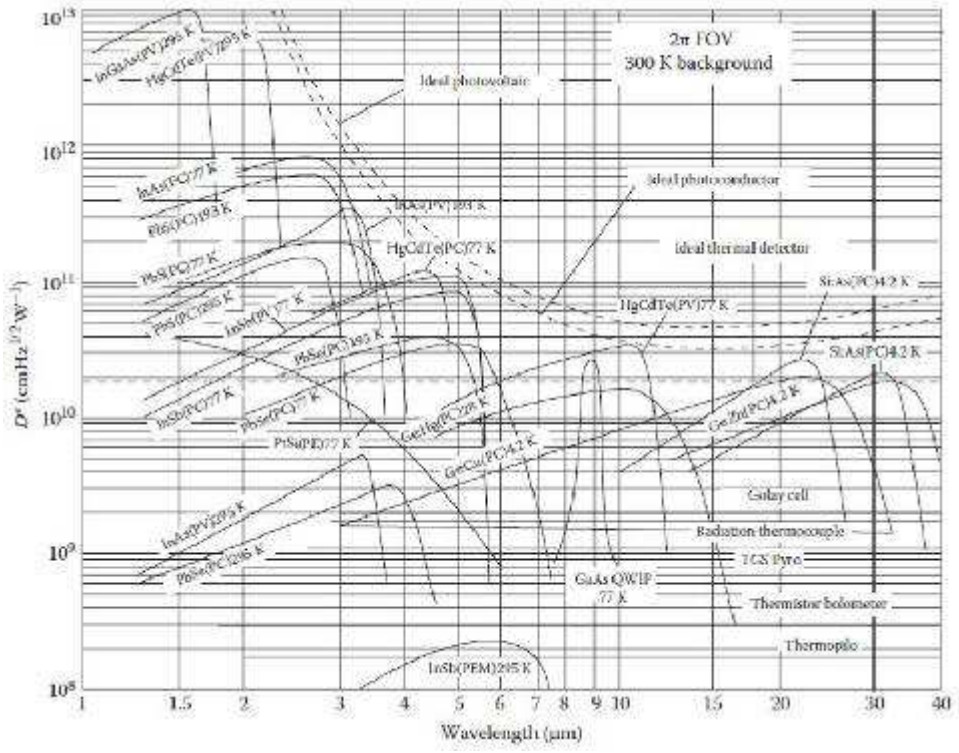

Figure 2.3: Specific detectivity curves for some IR detectors

2.1.3 System Performance Parameters: In thermal imaging, the system performance depends on both the spatial resolution and thermal sensitivity. In the following section, the different system parameters are discussed.

Spatial Resolution: Spatial resolution of an imaging system defines its ability to distinguish between two closely placed hot spots or objects within the field of view. Spatial resolution depends on the optics used by the IR system, mainly on detector array size and field of view.

If the detector array size is large, then more pixels will cover the scene in the field of view, hence increasing the spatial resolution. IR cameras with detector size 80x80, 16x120, 320x240, 640x512, 1024x1024 are available, higher the pixel numbers, better is the resolution. The other way to increase the spatial resolution is by decreasing the field of view (FOV). FOV is described in degrees of arc in the vertical and horizontal planes. In IR cameras normally 16-20 deg lens is used. For better spatial resolution, 7-10 deg lenses can be used. Total Field of View (TFOV) and Instantaneous Field of View (IFOV) are used to quantify the spatial resolution.

TFOV is the range of angles from which the incident radiations can be collected from the detector. Two components of TFOV are horizontal (H) and vertical (V) FOV. The TFOV is given by

$$TFOV = H \times V \qquad (2.9)$$

IFOV is the angular projection of the detector element at the target plane. IFOV defines the size of the area on the target from which the detector receives energy during any particular instance.

Modulation Transfer Function: The Modulation Transfer Function (MTF) describes both the spatial resolution and image quality of an imaging system in terms of spatial frequency response. The ability of an infrared system to transmit the spatial frequency of a scene is described in terms of the MTF. The MTF is shown in fig. 2.4.

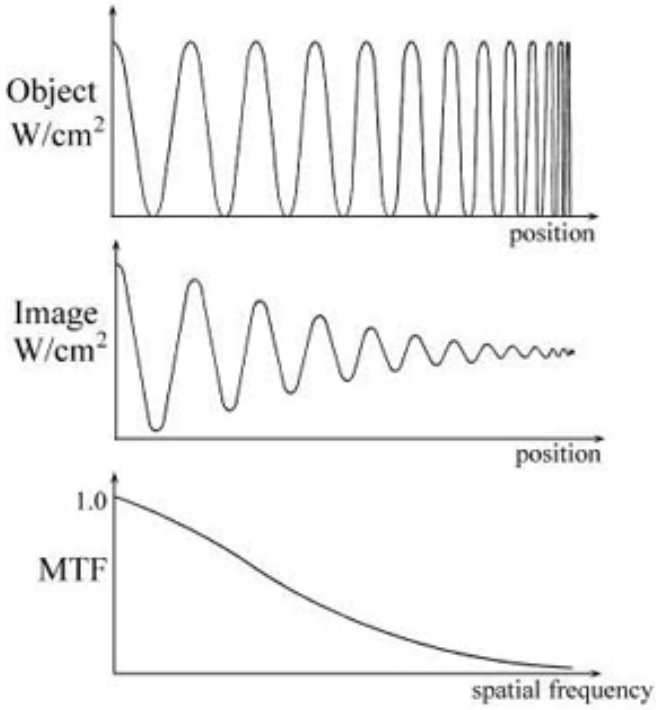

Figure 2.4: Modulation Transfer Function

Thermal Sensitivity: Thermal sensitivity is an important parameter in performance of an IR imaging system. Thermal sensitivity is the smallest difference in temperature that can be detected and displayed clearly by IR system above noise level. Commonly used terms to quantify the thermal sensitivity are Noise Equivalent Temperature Difference (NETD), Minimum Resolvable Temperature Difference (MRTD) and Minimum Detectable Temperature Difference (MDTD).

Noise Equivalent Temperature Difference*:* Noise Equivalent Temperature Difference (NETD) is the blackbody target to blackbody background temperature difference at which the signal to noise ratio of the scanner is equal to 1.

$$NETD = \frac{\Delta T}{SNR} \qquad (2.10)$$

Where ΔT is the temperature difference between the target and background and SNR is the signal to noise ratio. Signal and noise are obtained by capturing, averaging and taking the standard deviation of several thermal images.

NETD is a function of temperature and valid only at the temperature measured. NETD is a measure of noise in the IR image. It directly relates to the overall quality of the image. It is expressed in units of Kelvin (K). Cooled IR systems have lower noise levels compared to uncooled systems. NETD can be improved by increasing the size of detecting elements thus allowing elements to collect more flux. But this will reduce the spatial resolution by increasing IFOV.

Minimum Resolvable Temperature Difference: Minimum Resolvable Temperature Difference (MRTD) is a subjective parameter that describes the ability of the imager-human system for detection of low contrast details in the object under investigation. It is measured using a four bar target system and is a function of the minimum temperature difference between the bars of the standard 4-bar target and the background required to resolve the thermal image of the bars by an observer. MRTD combines both the thermal sensitivity and spatial resolution in a single measurement. At low spatial frequencies, thermal sensitivity is more important whereas at higher spatial frequencies the spatial resolution is dominating factor. MRTD is the temperature difference required between bars and spaces in standard test target, so that the bars are just discernable by an operator. While NETD is relevant to thermal sensitivity of a broad area target, MRTD refers to the thermal resolution of the imaging system as detected by the observer. The advantage of MRTD is that the results include a characterization of the thermal sensitivity of the sensor and the ability of a human observer to use the system to discriminate features within the thermal image.

Minimum Detectable Temperature Difference: Minimum Detectable Temperature Difference (MDTD) is a measure of the ability of an IR imaging system and an observer to detect a target of unknown location at one temperature against a large uniform background at another temperature for a limited time.

Noise: Any unwanted or spurious signal in a system is noise. It is not possible to get a system without noise but it can be reduced. In IRT, noise can be caused due to various reasons such as, noise from the detector, electronic noise (resulting from digitization), noise from external sources (background radiation, non uniform heating), noise due to materials lack of homogeneity, absorptivity and emissivity variation etc.

At the IR detector pixel level, noise can be classified into random and fixed pattern noise. Random noise can arise from variety of sources, but major contribution is from those that occur in the detector system. Three fundamental mechanism of noise production are, Johnson noise (occurs in conductors due to random motion of free electrons), generation recombination noise (occurs in semiconductors due to the fluctuation in the rate of generation of free charge carriers produced by the incident radiation and of the recombination of oppositely charged carriers) and 1/f noise (occurs in semiconductor where power spectral density varies inversely with frequency). Random noise is additive where magnitude of the random fluctuation is independent of signal intensity.

Fixed pattern noise refers to noise having a distinct pattern. Such kind of noise may appear from object distortion, intensity variation at pixel level, sensitivity variation between detectors at focal plane array.

To reduce the noise in thermal imaging system many preprocessing and post processing are done. The preprocessing involves Non Uniform Correction (NUC) and conversion of raw pixel value to temperature using proper calibration. Post processing involve mainly image and signal processing like, applying smoothing filters, polynomial fitting etc.

It is essential to know about the system performance of IR imaging system before it is used in the field. The knowledge of operating conditions (like temperature, humidity, atmosphere etc) is important since in IR imaging the IR radiation has to pass through the medium (atmosphere) before reaching the detector. High ambient temperature may cause malfunctioning of the electronics and rift in the calibration. Hence the operator must have knowledge of system parameters and the operating conditions.

2.2 Heat Transfer Mechanism for NDE

In the following section, theory and principle of PT and LT are discussed. Since active IRT involves propagation of thermal waves inside the material, thermo physical properties of the material and heat transfer mechanisms play important role. Different heat transfer mechanisms and few important thermo physical properties of material are discussed below [157].

2.2.1 Heat Transfer Mechanisms:

Conduction, convection and radiation are the three heat transfer mechanism between a body or two different bodies.

Conduction: Conduction is the propagation of heat energy, between two bodies or within a body, when a temperature gradient is present. One dimensional conductive heat transfer is given by Fourier law,

$$Q_{cd} = -K\frac{\partial T}{\partial x} \qquad (2.11)$$

where Q_{cd} is the conductive heat flux, ∂T is the temperature difference between two points separated by distance ∂x and k is material property called thermal conductivity.

Convection: Convection involves the transfer of thermal energy from one place to other by the movement of fluid. Two solids will exchange energy by convection if they are in contact with a fluid. Convection heat transfer is described with Newton's law of cooling.

$$Q_{cv} = h_{cv} (T_s - T_f) \qquad (2.12)$$

where h_{cv} is the convection heat transfer coefficient, T_s is the surface temperature and T_f is the fluid temperature.

Radiation: In radiation, the energy is transferred to or from a body by means of the emission or absorption of electromagnetic radiation. The maximum radiation flux emitted by a blackbody is given by Stefan-Boltzmann law (eqn. 2.3).

In active thermography techniques, the thermal waves generated at front surface, due to external stimulus, propagates to back surface by conduction, hence heat transfer by conduction is considered for analytical solutions.

The material properties which plays important role in active IRT are, density (ρ), specific heat (c_p) and thermal conductivity (K).

Thermal Diffusivity: Thermal diffusivity (α) is an important parameter in transient conduction problem. Thermal diffusivity is the measure of the materials ability to conduct heat in relative to store thermal energy (volumetric heat capacity)

$$\alpha = \frac{K}{\rho c_p} \qquad (2.13)$$

High diffusive materials respond faster to thermal changes and attain thermal equilibrium faster than the low diffusive material.

Thermal Effusivity: Effusivity (e) is the materials ability to exchange heat with the surrounding. It is given by the following equation,

$$e = \sqrt{K\rho c_p} \qquad (2.14)$$

Effusivity is a thermo physical property which is present in all the materials.

Reflection Coefficient: When thermal waves encounter interfaces, they are reflected. The extent of reflection depends on the thermal mismatch of two media. Reflection coefficient is given by following equation.

$$R = \frac{e_1 - e_2}{e_1 + e_2} \qquad (2.15)$$

Where e_1 and e_2 are the effusivity of two media (material and defect or coating and substrate).

2.2.2 Pulsed Thermography: Theory

Pulsed Thermography (PT) is one of the widely used active IRT techniques. It has become popular due to its fast inspection rate. In PT, the material is heated briefly and the resulting temperature variation is recorded using an IR camera. The pulse duration can vary from few milli seconds (for high conductivity materials) to few seconds (for low conducting materials). The short pulse is absorbed by the surface of the material which causes instantaneous increase in front surface temperature. The temperature of the object changes rapidly, because thermal front propagates under the surface, by diffusion. This diffusion causes decrease in front surface temperature while increase in rear surface temperature. Any discontinuity present inside the material alters the diffusion rate causing a temperature difference, above or below the discontinuity region when compared to surrounding area, which can be detected using IR camera. PT can be carried out either reflection or transmission mode. In reflection mode, the IR camera and lamps are positioned on the same side and decrease in front surface temperature is recorded. In

reflection mode, lamp and camera are positioned on opposite side and increase in back surface temperature is recorded. In the present study, reflection mode is used. The schematic diagram of the experimental set up and the temperature response of sound area and defective area are shown in fig. 2.4.

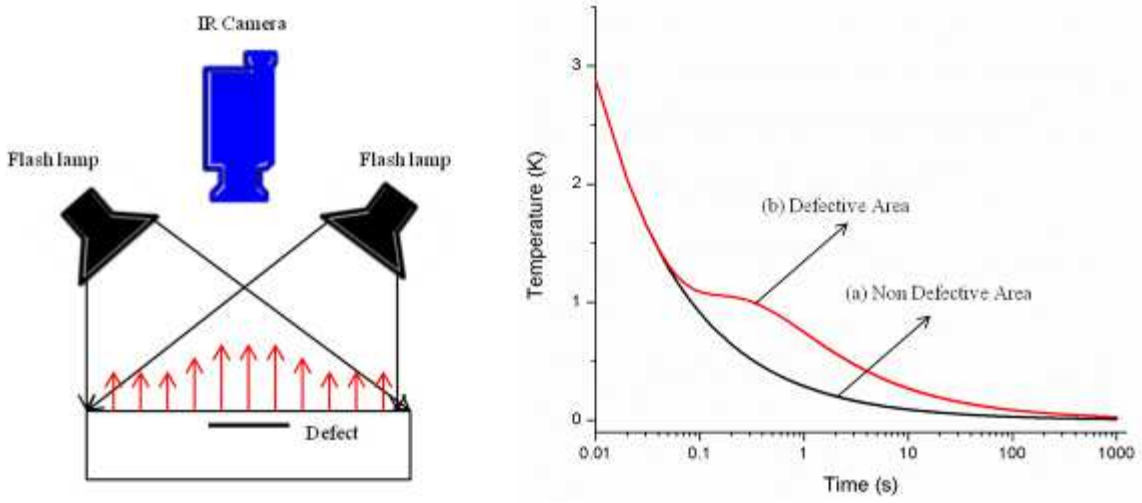

Figure 2.5: Schematic diagram of experimental set up and temperature decay curve

The transient (non steady) temperature distribution in solids is given by differential equation of heat conduction. Equation 2.16 is simple 1 Dimensional heat diffusion equation [158].

$$\frac{\partial^2 T}{\partial^2 x} = \frac{1}{\alpha}\frac{\partial T}{\partial t} \qquad (2.16)$$

The solution for surface temperature response, as a function of depth (x) and time (t), for instantaneous or Dirac pulse is given by following equation [46].

$$T(x,t) = \frac{Q}{e\sqrt{\pi t}} \exp\left(\frac{-x^2}{4\alpha t}\right) \qquad (2.17)$$

Q is the heat energy density, α is thermal diffusivity and e is thermal effusivity. In PT, we monitor only the surface temperature (x = 0), hence eqn. 2.17 reduces to,

$$T(0,t) = \frac{Q}{e\sqrt{\pi t}} \qquad (2.18)$$

The above equation shows that the transient temperature response of a material is inversely proportional to square root of time, for a given energy input. The above equation is valid for a semi infinite body. When a defect is present at finite depth L, the temperature response will deviate from sound area due to successful reverberation of thermal waves. Hence eqn. 2.18 has to modify to consider the effect of defect on temperature and it is as given below [61]

$$T(0,t) = \frac{Q}{e\sqrt{\pi t}}\left[1 + 2\sum_{n=1}^{\infty} R^n \exp\left(\frac{-n^2 L^2}{\alpha t}\right)\right] \qquad (2.19)$$

Where R is reflection coefficient, n is the reverberation that thermal waves make and L is defect depth.

The change in surface temperature, caused by the defect, depends on the type of discontinuity present inside the material. If an air gap or void containing air is present inside the material, then it will reflect the thermal waves back to front surface, since they have lower effusivity than the surrounding area (positive R). If an inclusion of higher effusivity is present, it allows thermal waves to propagate at higher rate than the surrounding, causing a decrease in surface temperature (negative R). This is illustrated in fig. 2.5, which is temperature response curve for a short pulse, with (a) R = 0.7, (b) R = 0 and (c) R = -0.7.

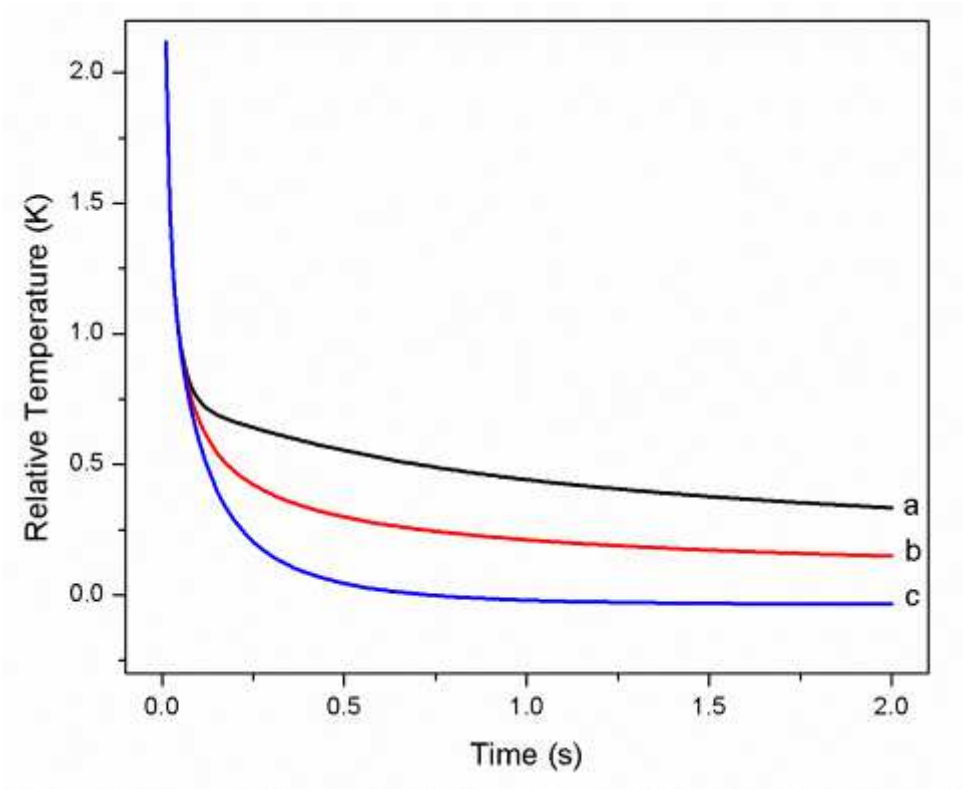

Figure 2.6: Temperature decay curve for (a) R = 0.7 (b) R = 0 (c) R = -0.7

The thermal wave from defect, which is near to surface, reaches the surface faster than the deeper defect. Hence deeper defect will be observed later than the near surface defect. Also, as thermal wave propagates inside the material, it attenuates which results in less contrast for deeper defect. The observation time is directly proportional to square of defect depth and contrast is inversely proportional to cube of defect depth [6]

$$T \approx x^2/\alpha;\ C \approx 1/x^3 \qquad (2.20)$$

where T is temperature, x is defect depth and C is temperature contrast.

2.2.3 Lock in Thermography: Theory

Lock in Thermography (LT) was first proposed by G. Busse et al [105]. In LT, the testing material is subjected to periodic heating using sinusoidally modulated heat source. The surface temperature of the object modulates periodically with frequency same as the

heating source. Thermal waves generated at front surface propagate inside the material and are reflected by the interfaces. The incoming and the reflected thermal waves interfere to cause change in phase and amplitude when compared to the input signal. This change in amplitude and phase is measured at each pixel to get amplitude and phase images. LT is carried out in steady state or stationary regime. LT gives more depth information and is invariant to surface emissivity variation.

The harmonic heating source has the form [157],

$$Q = \frac{Q_0}{2}\left[1 + \cos(\omega t)\right] \qquad (2.21)$$

where Q_0 is the intensity of heating source and ω is the angular frequency. The heating divides into two parts, $Q_0/2$ and $(Q_0/2)\cos(\omega t)$ which produces a dc temperature increase and an ac thermal modulation respectively. The dc part is neglected since LT is carried out in stationary regime. The heat conduction equation is solved for periodic heating component and the resulting temperature response is given by eqn. 2.22.

$$T(x,t) = T_0 \exp\left(\frac{-x}{\mu}\right)\cos\left(\omega t - \frac{x}{\mu}\right) \qquad (2.22)$$

where x is depth, t is time, $T_0 = \frac{Q_0}{2e\sqrt{\omega}}$ and $\mu = \sqrt{\frac{2\alpha}{\omega}}$ is the thermal diffusion length. Thermal waves are heavily damped while they travel in the medium and at a distance of thermal diffusion length thermal wave is attenuated by a factor of 63%. Thermal diffusion length is inversely proportional to square root of frequency and hence higher frequency is confined to the surface, while lower frequency penetrates deep inside the material. Figure 2.6 shows the comparison of input and output waves. The schematic diagram of the experimental setup is shown in fig. 2.7.

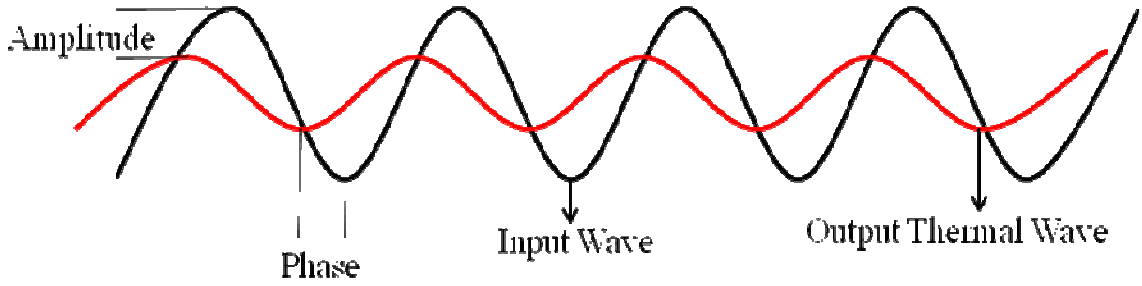

Figure 2.7: Comparison of input signal and output thermal wave

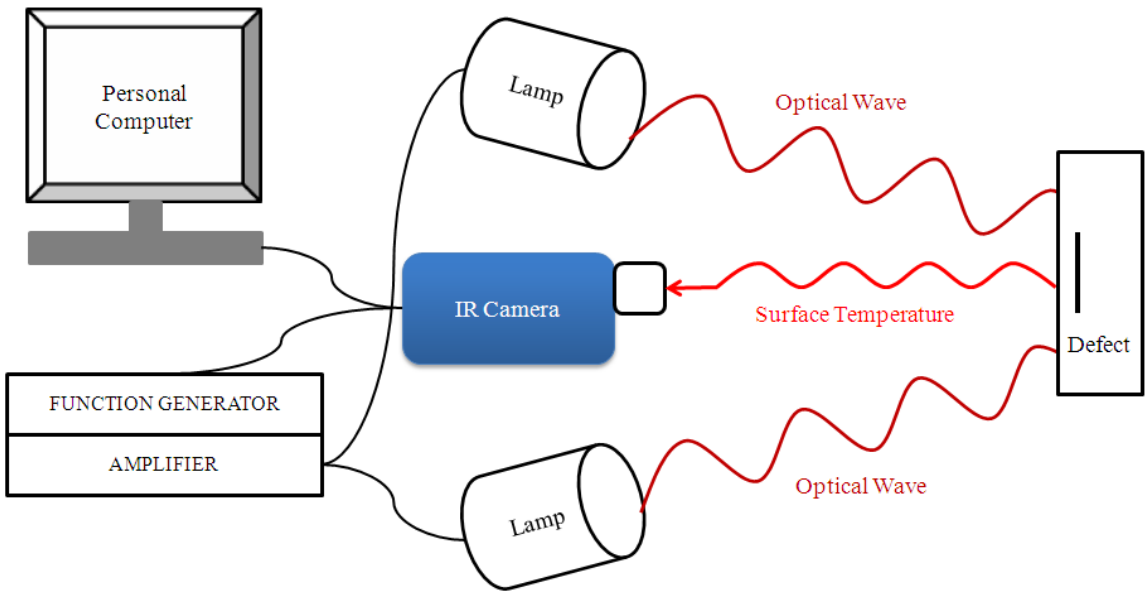

Figure 2.8: Schematic diagram of LT experimental setup

To get the amplitude and phase information from the temperature data, many algorithms have been developed, and most widely used algorithm is Four Point Correlation (FPC) method. In FPC method, four equidistant points (S_1, S_2, S_3 and S_4) are considered in one modulation cycle, then amplitude and phase information is obtained using following equations [105],

$$A = \sqrt{[S_1 - S_3]^2 + [S_2 - S_4]^2}\ ,\ \varphi = \tan^{-1}\frac{S_1 - S_3}{S_2 - S_4} \qquad (2.23)$$

Theoretically four images per one cycle will give phase and amplitude information, but if less number of image is acquired, then one will lose information. Hence numbers of images are acquired in one cycle and averaged it to obtain 4 images. From the above equation it observed that phase information is a ratio hence it is not affected by non uniform heating, optical absorption and emissivity variation [159].

2.3 Material and Qualification

India has embarked on an ambitious three stage nuclear program. The first stage of the program is based on pressurized heavy water reactors and is now a mature technology. The second stage of the program is based on fast reactors. The selection criteria for different components of second stage fast breeder reactors depends on the operating condition, ease of fabrication, cost and international experience. Clad and wrapper is the core components in a reactor. Compared to thermal power plants, components in a nuclear plant have to face not only the harsh operation environment of high pressures and temperatures but also the additional factors of irradiation by neutron and gamma radiations which can lead to deterioration of mechanical properties. In fast reactors, neutron flux is two orders higher than that of thermal reactors which leads to void swelling, irradiation creep etc. Sodium, used as coolant, poses high corrosion problem. Fast Breeder Reactors (FBR) operate at higher temperature ranging from 673 – 1273 K. The structural material should have high temperature mechanical properties for withstanding such high temperature operation conditions. Hence the structural material for FBR's should have good corrosion resistant properties, high temperature mechanical properties and good irradiation resistant properties. The international experience shows that stainless steel materials are suitable candidate for FBR structural materials. In FBTR AISI type 316 SS is used as structural materials. 316 SS has good corrosion resistant and creep resistant

property at high temperature. Further research has been carried out on 316 SS to improve its void swelling and sensitization problem. Alloy D9 is the structural material for PFBR, which is obtained by modifying the chemical composition of 316 SS. In alloy D9, titanium and silicon are added and nickel content is increased while chromium content is lowered.

Stainless steel is austenitic steel, which is obtained from quenching the austenitic phase in iron-carbon phase diagram and have Face Centered Cubic crystal structure (FCC). To get the 'stainless' property, sufficient amount of chromium (>13%) should be present. Chromium forms passive layer of chromium oxide which has the unique property of 'self healing'. Other alloying elements are Nickel (13-14 %), carbon (0.04-0.06 %) which gives the mechanical strength. Phosphorous and silicon are present in SS with minor concentrations as impurities.

Welding is a process of joining two dissimilar or similar metals and is widely used during the fabrication of different structural components. Welding of 316 SS causes problem of 'sensitization'. During welding, the operating temperature is 300 – 500 K and at this temperature chromium reacts with carbon forming stable chromium carbide precipitates at grain boundaries. In order for carbides to precipitate, it takes chromium from the surrounding making it chromium depleted region. If the chromium percent is less than 13 % in surrounding region, then it is no more corrosion resistant. This can cause localized intergranular corrosion. To avoid sensitization problem, the carbon content in 316 SS is reduced from 0.06 to 0.03 % and this type of SS is called AISI type 316 L SS. To improve the strength, sometimes nitrogen is added and this type is called AISI type 316 L (N). 316 L and 316 L (N) SS are used as structural components in PFBR.

For the present study, AISI type 316 L SS has been chosen. As indicated above, this steel is used for the fabrication of the reactor core and also structural components. Defects are likely during any fabrication process. While a variety of NDE methods are

used, surface defects like tight cracks formed during welding or service is still a matter of concern. Thermal imaging offers a potential method for surface defects especially cracks. No significant work has been carried out in this material especially with respect to the limits of detectability.

Parent materials was selected and machined to get smooth surface with thickness nearly 3.6 mm. This thickness has been chosen, since most of the rector components are of similar thicknesses. Materials qualification is an essential step in any experimental program. A systematic procedure was adopted for materials qualification. Optical emission spectrometry was carried to ensure its chemical composition. The parent material was then subjected to visual examination followed by ultrasonic inspection using conventional pulse echo technique. Both normal beam and angle beam techniques were adopted. The objective was to detect any defect such as laminations and stringers that can arise during plate manufacture. Radiography of the plates to be used for defect fabrication was also carried out to detect presence of any volumetric defects. The chemical composition is given in table 2.1. The thermo physical properties and thermal diffusivity are given in table 2.2.

Element	**C**	**Cr**	**Ni**	**Mo**	**Mn**	**P**	**S**	**Si**	**Fe**
Composition (%)	0.035	17.0	10.9	2.0	1.5	0.035	<0.003	0.6	Balance

Table 2.1: Chemical composition of the specimen

Parameters	**Stainless Steel**
K (W/m*K)	16.2
ρ (kg/m^3)	7990
c_p (J/(kg*K)	500
α (m^2/s)	4x10^{-6}

Table 2.2: Thermo physical properties of AISI type 316 L

The parent material was then machined into samples of size 150 mm (L) x 100 mm (B). Defects of various size and shape at different depth were then machined using Electro Discharge Machining (EDM). Defects were machined at depths 0.4 mm, 1.13 mm, 1.78 mm, 2.48 mm, 3.17 mm and 3.36 mm from front surface. Defects of shape square, rectangle and circle were drilled. The sizes of square defects are 10 x 10 mm, 8 x 8 mm, 6 x 6 mm, 4 x 4 mm, 2 x 2 mm. The diameters of circular defects are 10 mm, 8 mm, 6 mm, 4 mm and 2 mm. The size of rectangular defect is 10 x 5 mm, 8 x 4 mm, 6 x 3 mm, 4 x 2 mm and 2 x 1 mm. The size and depth of defect were measured accurately using non contact measuring machine (HAWK SYSTEM 7) with accuracy 2 µm and resolution 0.5 µm. The machined SS surface has shining appearance with typical emissivity value 0.5. A thin and uniform black paint is applied on the front surface of the sample to improve the emissivity of steel surface. The photograph of the sample with square defect with varying size and depth and black paint on the front surface is shown in fig. 2.9. Depth is from front surface and all units are in mm.

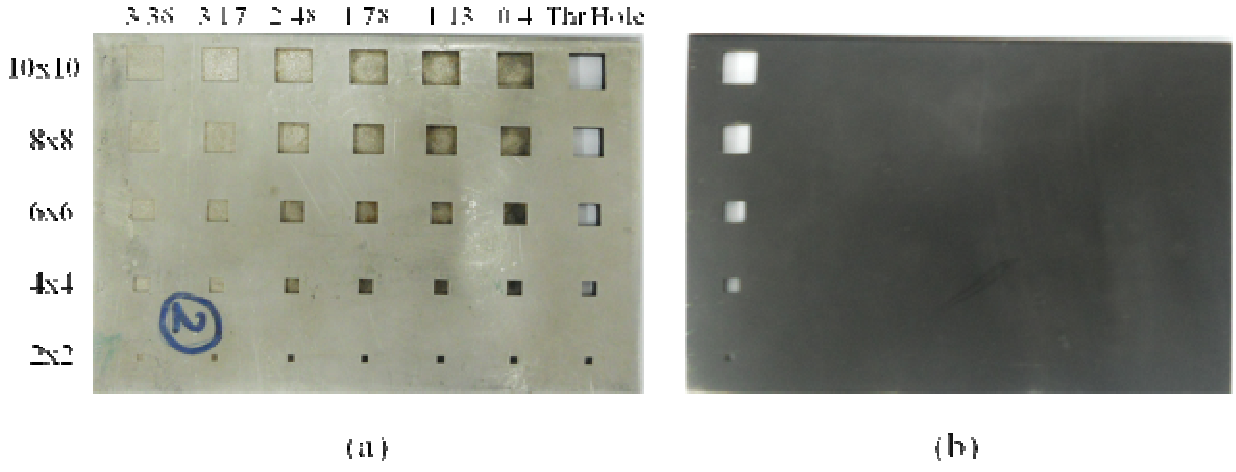

Figure 2.9: Photograph of the sample (a) Defects with varying size and depth (units are in mm, depth is from front surface) (b) Black paint on front surface

2.4 Thermal Imaging System and Experimental Set up

2.4.1 Thermal Imaging System

Thermal imaging camera used for the study is SILVER 420. The technical specifications are given below. The camera has Indium Antimonide (InAS) semiconductor detector (Type III-V) which works on the principle of photovoltaic effect. It detects IR radiation in the band 3.6 – 5.1 μm region. The detector array is focal plane based array with 320 x 256 detector elements. The pixel size is 25 μm x 25 μm and pixel pitch is 30 μm x 30 μm. Internal stirling cooling system is used to cool the detector which improves the thermal sensitivity to 25 mK. A germanium lens is used for focusing the incoming IR radiation. The maximum frame rate is 176 Hz at full window size and could be increased to 700 Hz with window size 64 x 8 pixels. The frame rate could be varied at step of 1 Hz. The integration time is 3 μs to 20 ms and could be varied at a step of 1 μs step. Temperature range is from 5 deg C to 1000 deg C. Accuracy is ± 2 deg C for less than 100 deg C and ± 2% of measurement above 100 deg C.

2.4.2 Experimental Set up

2.4.2.1Pulsed Thermography: PT was carried out in reflection mode, where lamps and camera were kept on the same side. Two Xenon flash lamps with maximum power 1600 W each were used as source. The pulse width at maximum power is 2 ms. Nexus 3600 series lamps were used provided by BALCAR company. The power level could be varied using a control knob. The energy delivered at the maximum power (1600 W) is around 4 KJ. The experimental set up is shown in fig. 2.9 (a). Image sequences were acquired using ALTAIR software which displays 16 bit pseudo color image on display.

Figure 2.10: Experimental Set up (a) Pulsed Thermography (b) Lock in Thermography

2.4.2.2Lock in Thermography: For LT, two halogen lamps were used as source of heat. The maximum power of lamps were 1000 W. The heat source was connected to amplifier and function generator. HAMEG 15 MHz programmable function generator and PULSAR amplifier with 6x10 A and 1-3 phase status dimming. The images were acquired with frame rate greater than 2f, where f is the modulation frequency to fulfill the Nyquist criteria. ALTAIR LI software was used for analyzing thermal image sequences and to get phase and amplitude images. The output of ALTAIR LI software is average image, phase image and amplitude image. The photograph of experimental set up is shown in fig. 2.9 (b). The entire set of experiments was performed under controlled conditions. The ambient temperature was ensured to be 298 K. It was ensured that no air drafts are likely in the vicinity and experimental setup was on a rigid base to avoid any vibrations and movements.

While generating optical stimulus, the halogen lamps get heated up, emitting IR radiations. These radiations will fall on sample and affect the lock in measurements. To avoid this unwanted signal, Perspex sheets with water bath was kept in front of the lamps which allows visible light but cut off IR radiation from lamp.

2.5 Numerical and Theoretical Tools Used

ThermoCalc 6L: Finite difference analysis was carried out to validate the experimental data. ThermoCalc 6L software was used for the finite difference analysis. It is a FDM based special software developed by Vavilov et al for solving active thermography problems. ThermoCalc 6L solve 3 D transient heat conduction problems and it takes care of heat loss due to convection[160]. The mathematical formula and the initial and boundary conditions are given below.

$$\frac{\partial T(x,y,z,t)}{\partial t} = \alpha\left[\frac{\partial^2 T(x,y,z,t)}{\partial x^2} + \frac{\partial^2 T(x,y,z,t)}{\partial y^2} + \frac{\partial^2 T(x,y,z,t)}{\partial z^2}\right] \tag{2.24}$$

$$T\ (t = 0) = T_{in} \tag{2.25}$$

$$-K\frac{\partial T(x,y,z=0,t)}{\partial z} = Q(x,y,t) - h_{cv}\left[T(x,y,z) - T_a\right] \tag{2.26}$$

where T is the temperature, α is the thermal diffusivity, T_{in} is the initial temperature, K is thermal conductivity, Q is the heat flux power density, h_{cv} is the heat exchange coefficient on front surface and T_a is the ambient temperature. Equation 2.24 is the 3 D parabolic equation of heat conduction, eqn. 2.25 is the initial condition and eqn. 2.26 is the boundary condition.

CHAPTER 3
DEFECT CHARACTERIZATION USING PULSED THERMOGRAPHY

3.1 Introduction

With the advent of fracture mechanics concepts, defect characterisation has become very important. Apart from defect size and shape, the determination of depth is very crucial to assess the defect severity and also predict remnant life. In PT, the thermal waves generated at front surface due to the flash, propagates to back surface by diffusion, causing continuous decrease in front surface temperature. When thermal waves encounter defects, they will reflect back on to the surface causing increase in surface temperature. If two defects are present inside the material at different depths, the thermal waves reflected by defect which is near to surface, reaches the surface earlier than the deeper defect. Hence in a thermogram, the defect closer to the front surface will appear first as shown in fig. 3.1. It can also be observed from the figure that the defects will appear diffused in the thermal image with increasing times. By plotting and comparing the temperature decay over sound area and defective area one can measure the time where decay curve for defective area deviates from non defective area and this time is a function of defect depth. By measuring the time of deviation, one can quantify the defect depth [5, 157].

To measure this time of deviation, many methods have been proposed in literature. The most commonly used ones are temperature contrast method [6, 61], contrast derivative method [64], log first derivative method [48] and log second derivative method [161]. Log first derivative method has been successfully used for coating thickness

characterization [48, 162]. In the present study, this method has been used for defect depth quantification.

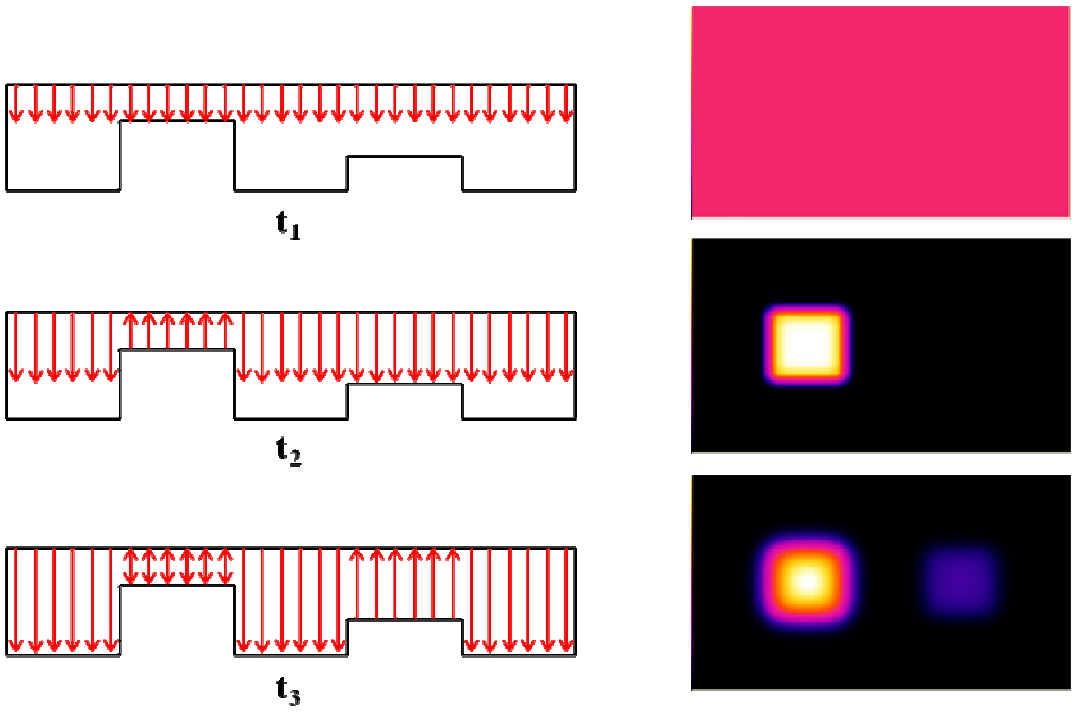

Figure 3.1: Schematic diagram of material with two defects at different depths and propagation of thermal waves at different time intervals ($t_1 > t_2 > t_3$)

In PT, many factors affect the depth prediction like defect size, input energy, defect thickness etc [62]. In general it has been observed that some of the methods used for defect depth quantification in PT have dependency on defect size. Studies have emphasized on importance of early time prediction of temperature contrast to overcome 3 D heat diffusion [163, 164] and limited work has been reported on the effect of defect size on depth estimation using PT [65, 165]. In practical applications, defect size and shape are unpredictable. Hence it is important to study the effect of defect size and shape on the above discussed peak time.

Another aspect of defect characterization is defect sizing. In PT, defect size decreases as the time elapses due to the diffusion of heat around the defect [68-71]. Hence this part has to be taken care while measuring the defect size.

This chapter focuses on the application of PT for depth quantification using above mentioned methods. In each method, calibration plots are generated using defects of known depth, which are later used to predict depth of unknown defect. The effect of defect size and shape on depth prediction is carried out. The defect sizing is also carried out by measuring the Full Width at Half Maximum (FWHM) at different time intervals.

3.2 Depth Quantification Methods

Temperature Contrast Method: Temperature contrast refers to the difference in temperature between the defective region and an adjacent good or non defective region. Mathematically, temperature contrast TC_{abs} is given by

$$TC_{abs} = T_{def} - T_{ND} \qquad (3.1)$$

where T_{def} is temperature over defective area and T_{ND} is temperature over non defective area. Higher the TC_{abs} better is the visibility of defect. TC_{abs} is directly related to the depth of a defect. Shallower a defect, more thermal waves reach the surface and thus better would be the contrast (high TC_{abs}). Deeper a defect, lower would be the value of TC_{abs}. Temperature contrast over a defective region is also not a constant with time. It varies, increasing first and then decreasing with time. The time at which it rises to its maximum value is referred to as peak contrast time (t_c) and this peak contrast time is a more precise measure of the depth of a defect. t_c can be determined from the temperature contrast vs. time plot. It increases with increasing defect depth. The above mentioned method of using

temperature contrast values for depth detections is referred to as temperature contrast method.

Contrast Derivative Method: One can also take the first derivative of the temperature contrast and then use the peak time determined from this plot for defect depth quantification. In this case the peak time is referred to as peak contrast derivative time and is given by

$$t_s = \frac{3.64L^2}{\pi^2 \alpha} \qquad (3.2)$$

where L is defect depth.

Log First Derivative Method: The surface temperature response for a short (Dirac) pulse is given by following equation [47],

$$T(0,t) = \frac{Q}{e\sqrt{\pi t}} \qquad (3.3)$$

The above equation shows that temperature and time are inversely related. Taking eqn. 3.3 in logarithmic domain one will get the following equation,

$$\ln(T(0,t)) = \ln\left(\frac{Q}{e\sqrt{\pi}}\right) - \frac{1}{2}\ln(t) \qquad (3.4)$$

When temperature history of sound area is plotted in logarithmic domain, one will get a straight line with slope -1/2. When a defect is present, the temperature decay curve will deviate from the straight line. By taking the first derivative, the plot will peak at a particular time. This time is referred to as the peak first derivative time (t_p) and is a function of defect depth. The theoretical relation between t_p and L is given below.

$$t_p = \frac{0.693L^2}{\alpha} \qquad (3.5)$$

Log Second Derivative Method: In this method, the second derivative of both log temperature and log time is taken and then the peak time is computed from this curve. This peak time is referred to as log second derivative peak time and is given by

$$t_2 = \frac{L^2}{\pi\alpha} \qquad (3.6)$$

It can be observed from eqn. 3.6 that thermal diffusivity and defect depth are the main parameters that influence the defect detectability. For a given material, the defect detectability is better if it is located closer to surface.

The temperature decay plot corresponding to fig. 3.1, in logarithmic domain is shown in fig. 3.2.

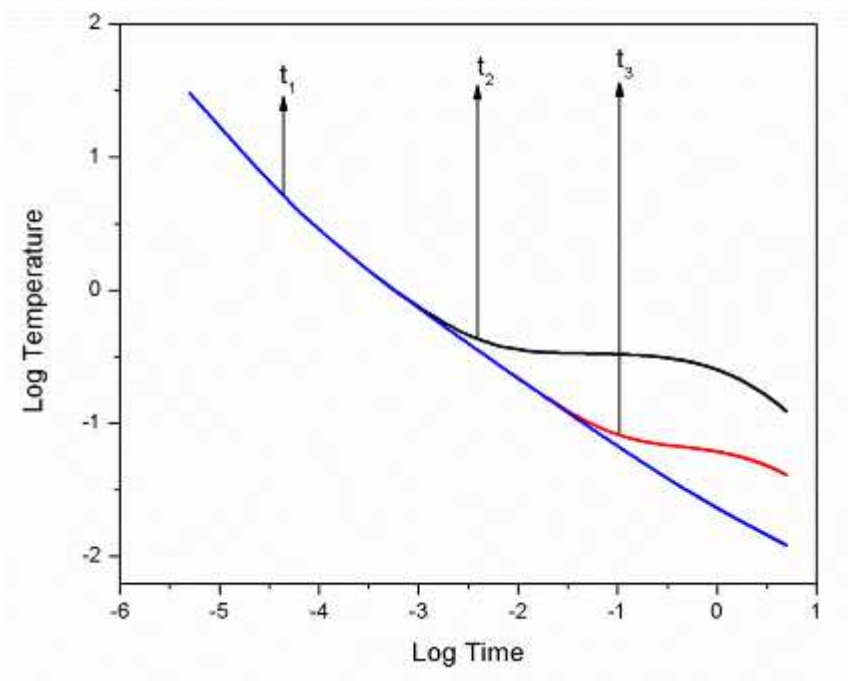

Figure 3.2: Temperature decay curve in logarithmic scale for sound area and two defects at different depths

3.3 Noise Reduction by Thermal Signal Reconstruction (TSR)

PT is associated with noise due to detector, non uniform heating etc. In the present work we apply Thermal Signal Reconstruction (TSR) proposed by Shepard [72, 73]. In TSR, the temperature response at each pixel is taken in log scale as per eqn. 3.4. A polynomial of higher order is fitted to the curve according to eqn. 3.7 which is the best fit for that curve, where N is order of polynomial and a_n is polynomial coefficient. The temperature data can be reconstructed using eqn. 3.8 which is noise free. This data is considered for analysis. Series of polynomial fit was carried out to determine the order of polynomial which gives best fit. It was observed that polynomial of order 6 gives the best fit.

$$\ln\left(T\left(0,t\right)\right) = \sum_{n=0}^{N} a_n \left(\ln\left(t\right)\right)^n \tag{3.7}$$

$$T\left(0,t\right) = \exp\left[\sum_{n=0}^{N} a_n \left(\ln\left(t\right)\right)^n\right] \tag{3.8}$$

Temperature decay curve in log scale and corresponding polynomial fit of order 6 is shown in fig. 3.3.

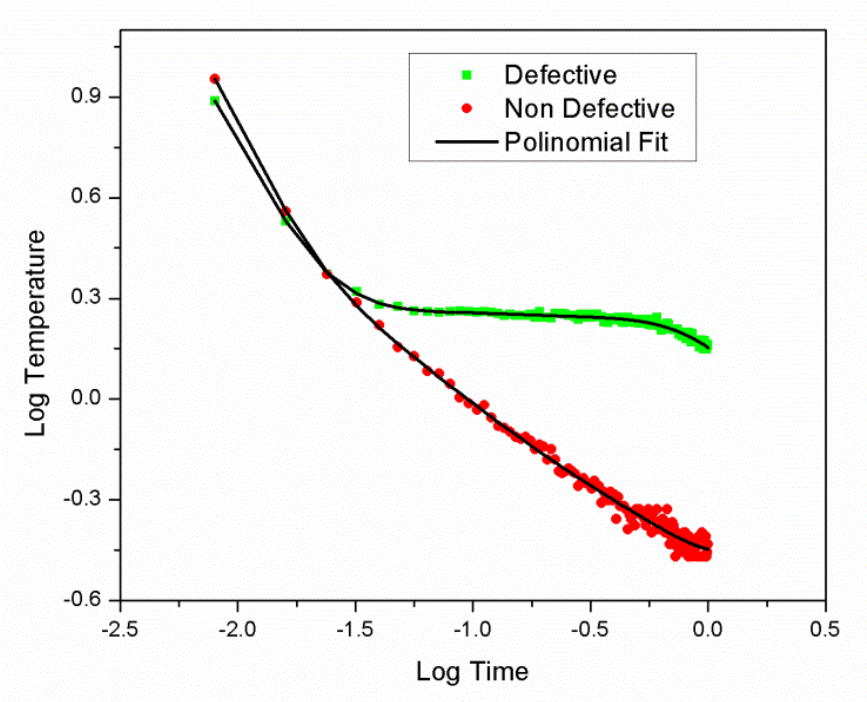

Figure 3.3: Experimental temperature decay curve in logarithmic domain for defective and non defective area and polynomial fitting of order 6

3.4 Experimental Parameter and Numerical Simulation

The experiment was conducted in reflection mode. The camera to object distance was kept at 35 cm so that the sample covers 80 % of FOV of camera. The lamps were kept at a distance of 30 cm from the sample to ensure that the flash covers the whole area of the sample. The frame rate used for acquisition was 125 Hz and the time of acquisition was 2 sec. Since Stainless Steel (SS) has relatively high thermal diffusivity ($4x10^{-6}$ m^2/s), high frame rate and less acquisition time was used.

The thermal conductivity, density and specific heat of AISI type 316 L SS, air and general parameters used for the ThermoCalc 6L analysis are given in Table 3.1. The analysis is carried out for time interval of 2 seconds with time step of 0.008 second. The initial and ambient temperatures were taken as 298 K. The sample length was taken as 150 x 100 x 3.5 mm. The sample was divided into 300 equal parts along x axis (length) and 200 equal parts along y axis (breadth) (mesh size of 0.5x0.5 mm). **:** The mesh size (0.5

mm) chosen such that it is nearly equal to the pixel size of the IR camera at a distance of 35 cm. Along z direction (thickness) it was divided into 350 parts (mesh length 0.01 mm).

Parameters	Stainless Steel	Defect
k (W/m*K)	16.2	0.0257
ρ (kg/m^3)	7990	1.125
c_p (J/(kg*K)	500	1005
General Parameters		
Q (W/m^2)	400000	
t (s)	2	
Time Step (s)	0.01	
H (W/m^2*K)	10	
T_{in} (K)	298	
T_a (K)	298	

Table 3.1: Thermal properties of stainless steel, air (defect) and other parameters used in ThermoCalc 6L simulation

Analytical calculations were done using MATLAB. Analytical modeling was carried out using eqns 2.18 for sound area and 2.19 for defective area with defect depth L.

3.5 Results and Discussion

3.5.1 Depth Quantification

Before the flash, few thermal images were acquired and averaged. This averaged thermal image is used for background subtraction and then TSR was carried out for reducing the noise. Images obtained after TSR were analyzed for further study. The near surface defects cause greater temperature difference than the deeper defects. This is because, as the heat wave propagates through the material, its strength decreases due to

attenuation. Hence, change in surface temperature caused by the deeper defect is small when compared to defects near surface. This can be clearly seen in fig. 3.4 which is thermal image sequences acquired at different time intervals. Image 3.4 (d) is a raw image at 1.2 sec which clearly shows the noise and non uniformity in temperature. The image also reveals that defect of size 10 mm which is buried at a depth of 2.54 mm could be detected using PT.

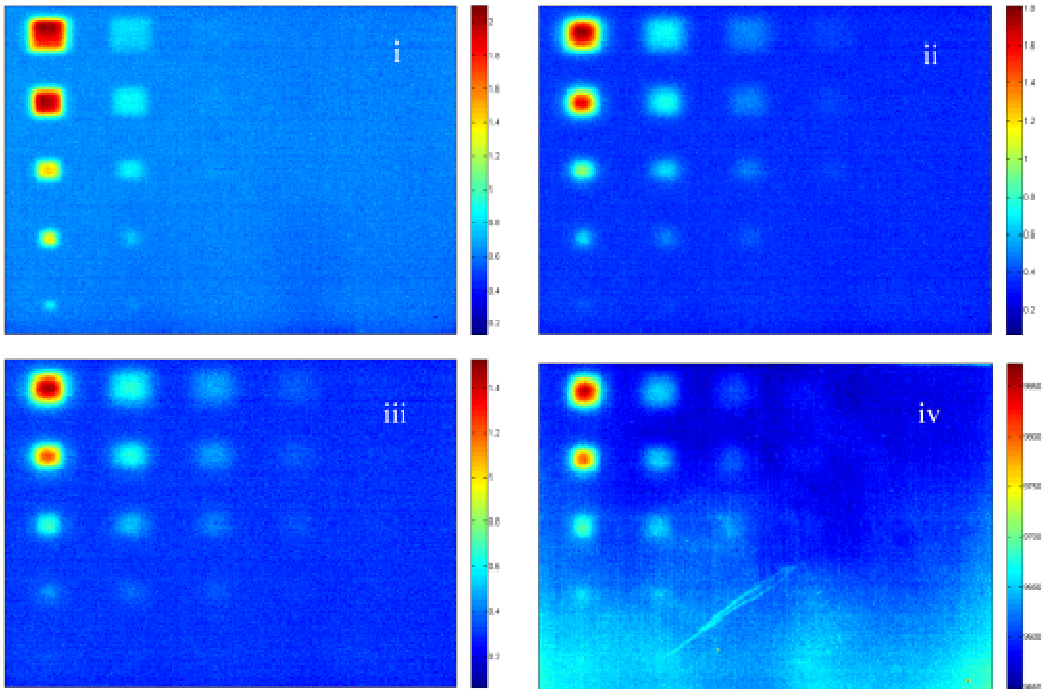

Figure 3.4: Thermal image sequences at time (a) 0.2 s (b) 0.75 s (c) 1.2 s (d) raw image at 1.2 s after flash

For defect depth quantification, defects of size 10x10 mm at various depths were considered. The experimental results were compared with numerical and analytical results.

Temperature Contrast Method: Temperature contrast was computed by taking the temperature difference between defective and non defective areas and plotted as a function of time (fig. 3.5 (a)). It can be observed from fig. 3.5 (a) that near surface defects peak at earlier stage and deeper defects at later stage. This is because, thermal waves reflecting

from the near surface defects reach the surface earlier than the thermal waves reflected from deeper defects. Hence peak contrast time can be used for defect quantification. A plot of peak contrast time as a function of defect depth indicates a linear relationship (fig. 3.5 (b)). A straight line is fitted to the plot by least square method with R^2 (coefficient of determination) = 0.8513.

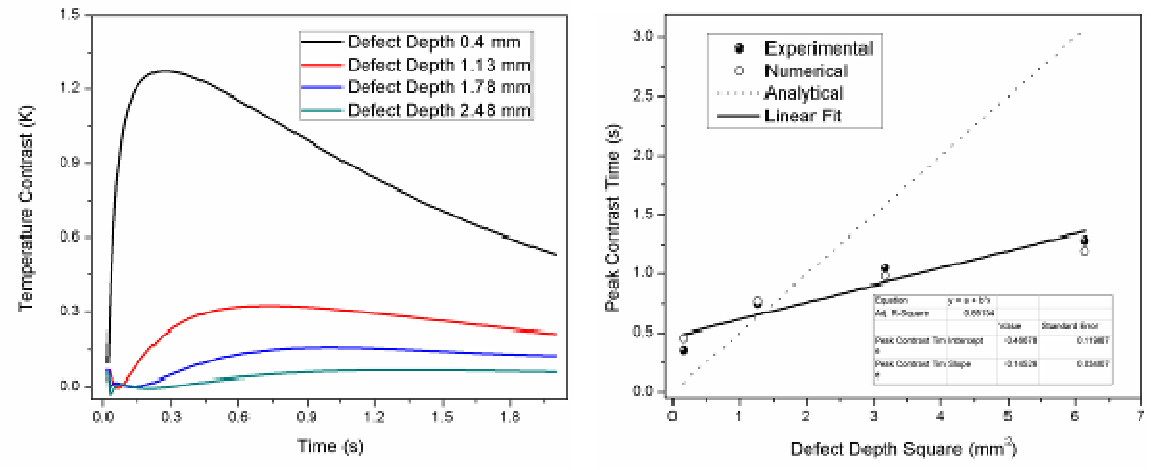

(a) (b)

Figure 3.5: (a) Temperature contrast variation as a function of time for defects of various depths (b) Peak contrast time variation as a function of square of defect depth

Temperature Contrast Derivative Method: In this method, the first derivative of the temperature contrast was computed and plotted as a function of time in fig. 3.6 (a). The curve peaks at a time t_s which is a function of defect depth. According to eqn. 3.2, t_s is a linear function of square of defect depth. Figure 3.6 (b) shows the variation of t_s with square of defect depth. The error bar in the plot shows the standard deviation of t_s from theoretical value. Least square fit was carried out with R^2 = 0.9733.

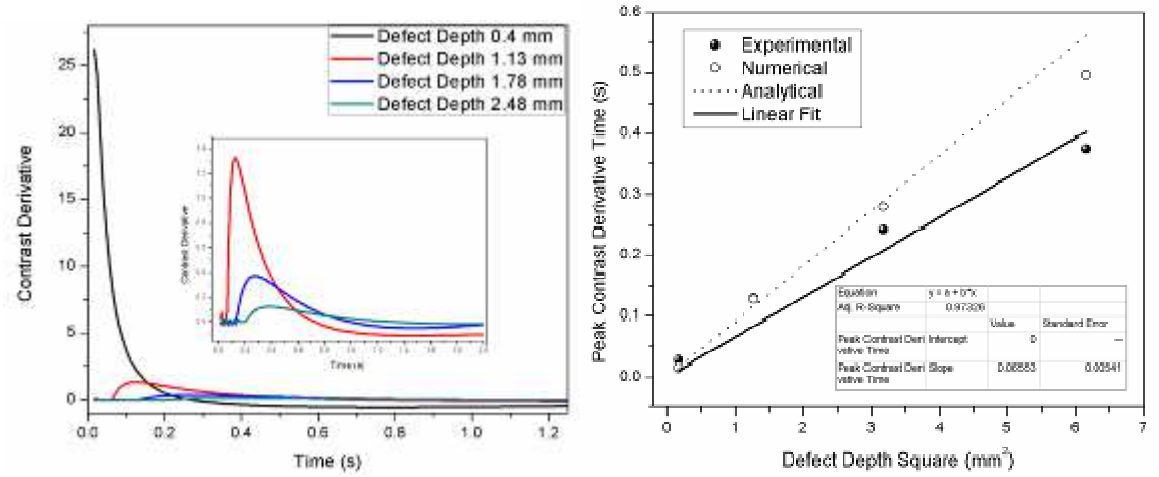

(a) (b)

Figure 3.6: (a) Contrast derivative variation as a function of time for defects of various depths (b) Peak contrast derivative time variation as a function of square of defect depth

Log First Derivative Method: Temperature decay curve has linear relation in logarithmic domain (eqn. 3.4). Temperature response of defected region is plotted in log scale and the first derivative was computed and plotted as a function log time as shown in fig. 3.7 (a). The peal derivative log first derivative time was measure and plotted as a function of square of defect depth which has a linear relation as shown in fig. 3.7 (b). Least square fit was carried out with $R^2 = 0.9764$.

Log Second Derivative Method: Second derivative of log temperature response is computed and variation with time is plotted in fig. 3.8 (a). The peak derivative time t_2 is obtained for experimental and simulated results and compared with theoretical value in fig.3.8 (b). The curve was fitted with straight line with $R^2 = 0.9975$.

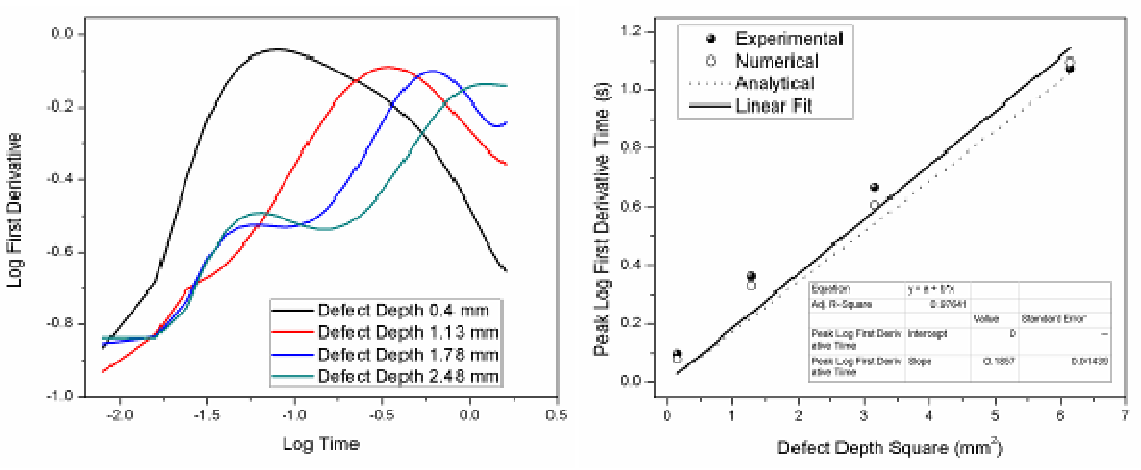

(a) (b)

Figure 3.7: (a) Log first derivative variation as a function of log time for defects of various depths (b) Peak log first derivative time variation as a function of square of defect depth

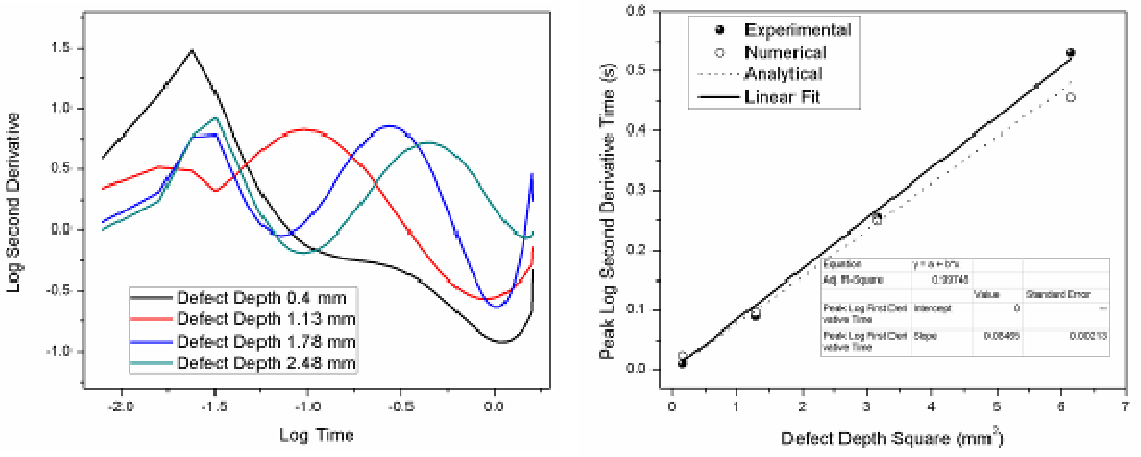

(a) (b)

Figure 3.8: (a) Log second derivative variation as a function of log time for defects of various depths (b) Peak log second derivative time variation as a function of square of defect depth

From above analysis it was observed that best fit is obtained for temperature contrast derivative and log second derivative methods when compared to temperature contrast method.

From the calibration plots it is observed that numerical simulations are in good agreement with experimental results. Theoretical analysis shows a large deviation in case of temperature contrast method and good agreement with other methods. The reason for this deviation is discussed in the later part of this chapter. Simulated values agree very well for shallower defects and minor deviations are observed for deeper defects. This is due to the uncertainty in measurement for deeper defects and the square of defect depth is considered.

Validation: To study the validation of the calibration plot obtained from the above discussed methods, PT was carried out on another sample with same experimental parameters used in the above experiment. Three defects with depth 0.5, 1.15 and 1.83 mm were considered for validation and peak contrast time, peak contrast derivative time, peak first derivative time and peak log second derivative times were computed. These peak times were used to predict the depth of defect using the above generated calibration plots. Table 3.2 shows the predicted depth and associated error in prediction using above mentioned methods. It was observed that error associated with temperature contrast method was large (20% maximum) when compared to other three methods (12% maximum). This is because, temperature contrast takes longer time for peaking when compared to contrast derivative and log second derivative. As time increases, lateral diffusion of heat becomes predominant, this could be the major contributing factor for the error in measurement. Another observation is that the error associated in case of near surface defect is more. This is because change in or missing of single frame causes this variation. Hence it is recommended to use a higher frame rate, to get good accuracy in case of near surface defects.

Actual Depth (mm)	Temperature Contrast Method		Contrast Derivative Method		Log First Derivative Method		Log Second Derivative Method	
	Predicted Depth (mm)	% Error	Predicted Depth (mm)	% Error	Predicted Depth (mm)	% Error	Predicted Depth (mm)	% Error
0.5	0.4	20	0.45	10	0.57	14	0.44	12
1.15	1.30	13	1.05	8.7	1.28	11.3	1.06	7.8
1.83	2.04	11.5	1.70	7.1	1.93	6.01	1.92	5

Table 3.2: Predicted and actual defect depths and associated error in prediction using four methods

3.5.2 Effect of Defect Size and Shape on Depth Quantification

In this section, we focus on the effect of defect size and defect shape on defect depth estimation.

Effect of Defect Size: The above study showed that PT is a promising NDE technique for inspection of the surface for defects. The above study is for fixed defect size.

For studying effect of defect size, square defects of size 10 mm x10 mm, 8 mm x 8 mm, 6 mm x 6 mm and 4 mm x 4 mm were considered at different depths. Defects of size 2 mm x 2 mm were not considered for analysis since they were barely visible as can be seen from fig. 3.4.

For computing temperature contrast, the area adjacent to defective area was chosen as non defective area. Temperature contrast was computed for defects of depth 0.4 mm, 1.13 mm and 1.78 mm and of size 10x10 mm, 8x8 mm, 6x6 mm and 4x4 mm and is shown in fig. 3.9 (a). The first derivative of contrast was also computed and plotted as a function of time and is shown in fig. 3.9 (b).

The temperature history was taken in logarithmic domain and the first and second derivatives were obtained and plotted as a function of log time and is shown in figs 3.9 (c) and (d) respectively.

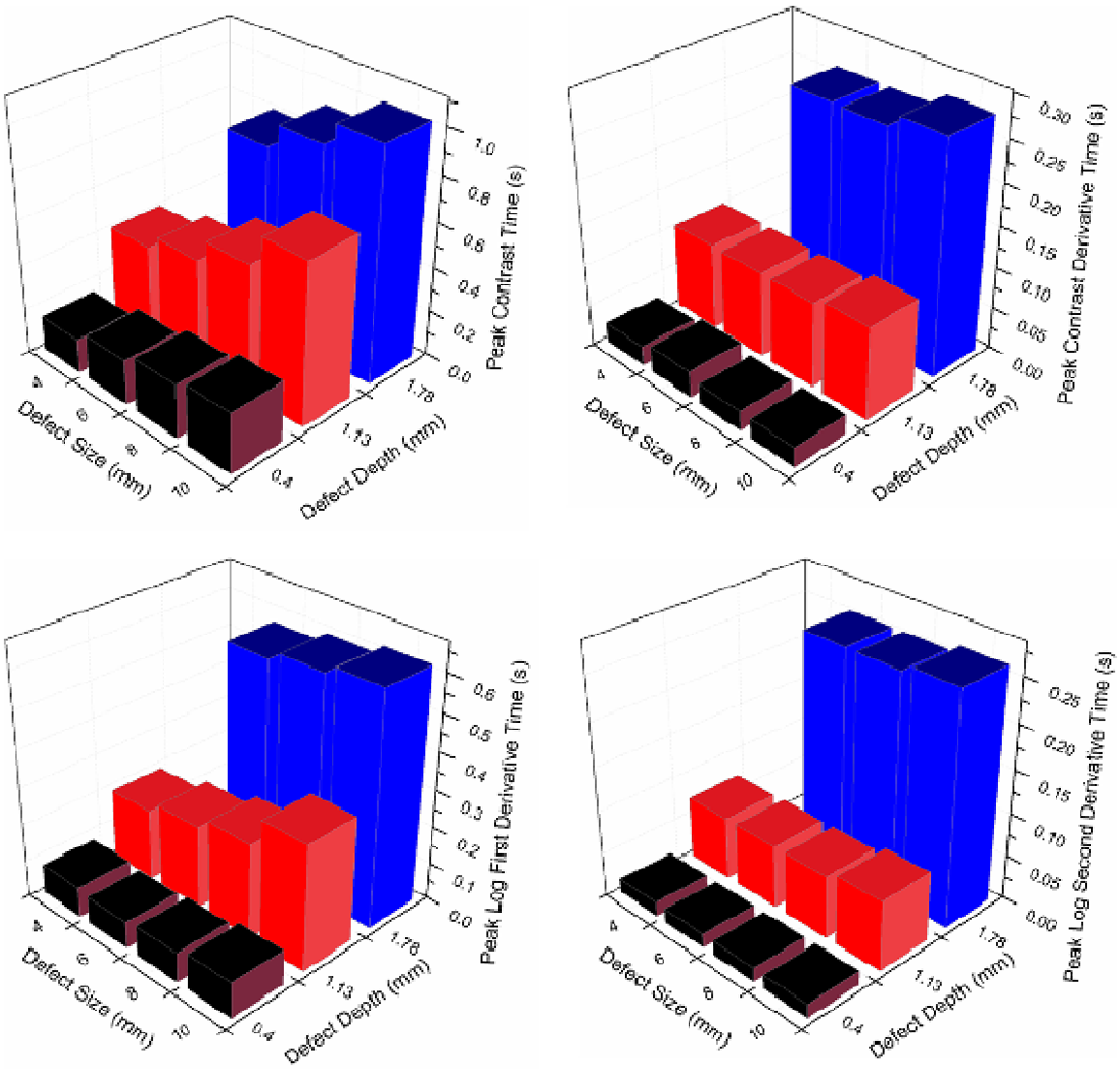

Figure 3.9: (a) & (b) Temperature contrast and contrast derivative variation as a function of time for defects of various sizes at a depth of 1.13 mm (c) & (d) Log first derivative and log second derivative variation as a function of log time for defects of various sizes at a depth of 1.13 mm

From fig. 3.9 it can be observed that the peak time in case of temperature contrast and log first derivative methods decrease as defect size decreases. But contrast derivative and log second derivative peak times are not affected by defect size.

Effect of Defect Shape: To study the effect of defect shape, three samples of same dimensions were chosen and defects of square, circular and rectangular shape were drilled at various depths and of varying size. The schematic diagram of the shape of the defects is shown in fig. 3.10. The area of square defect is slightly higher than the circular defect while area of rectangle defect is half of the square defect. Then experiment was conducted with same experimental parameters which are used for initial experiment. Then TSR is performed to reduce noise and this data is used for analysis. Defects of size 10 mm were considered for analysis. In case of square defect the area is 100 mm^2 (10x10), for defect of shape circle the area is 79 mm^2 (25π) and for rectangular defect, it is 50 mm^2 (10x5).

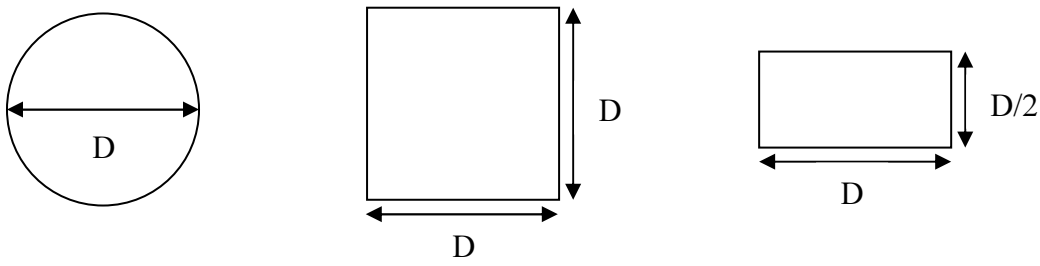

Figure 3.10: Schematic diagram of defects of various shapes with dimension

Temperature contrast, contrast derivative, log first derivative and log second derivative were computed for defects of various shapes with defect size 10 mm and depth 1.13 mm. These temperature responses were plotted as a function of time and are shown in fig. 3.11. From the plot it is observed that peak contrast time and log first derivative time are almost equal for square and circular defects where as for rectangular defect it is low. In case of contrast derivative and log second derivative methods, the peak times for all the three cases are almost same.

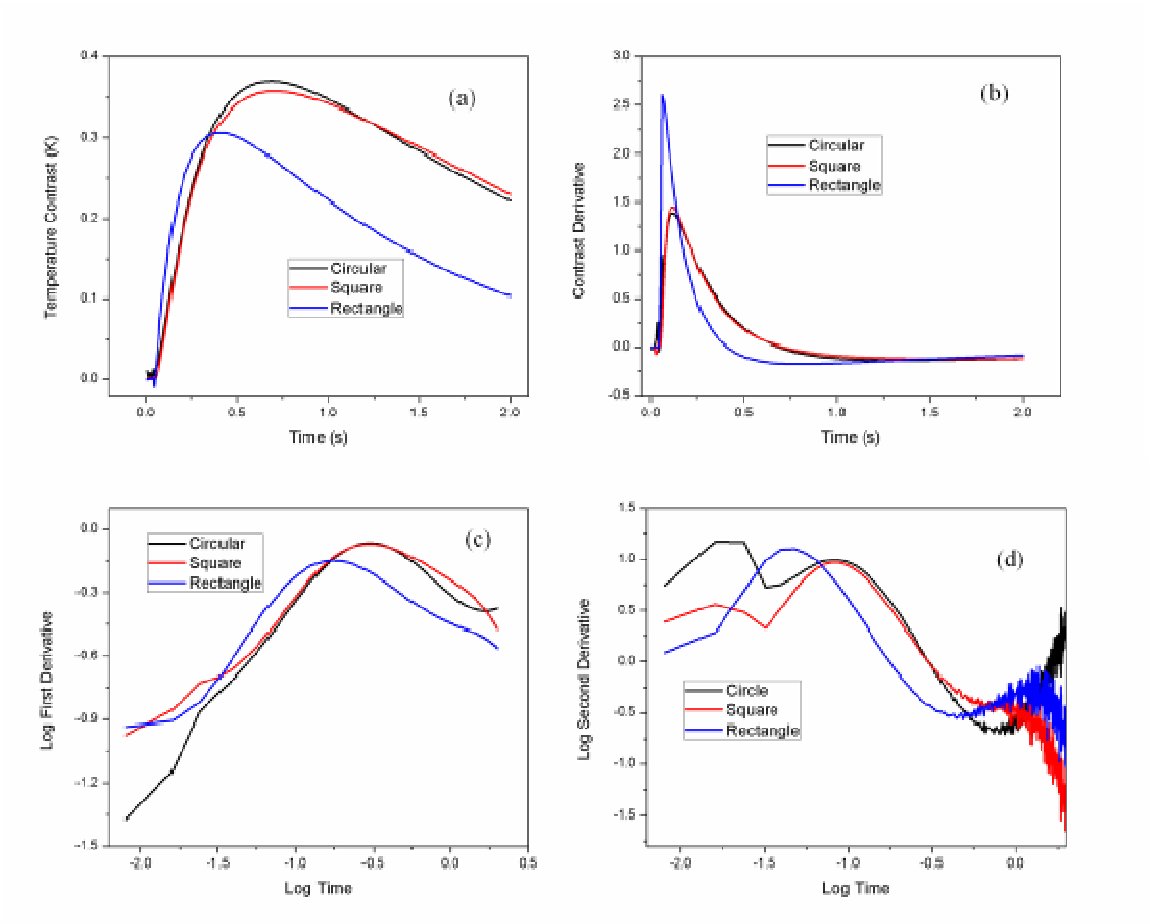

Figure 3.11: (a) & (b) Temperature contrast and contrast derivative variation as a function of time for defects of various shapes at a depth of 1.13 mm (c) & (d) Log first derivative and log second derivative variation as a function of log time for defects of various shapes at a depth of 1.13 mm

The above study showed that peak contrast and peak log first derivative times were affected by defect size and shape where as peak contrast derivative and peak log second derivative times were invariant of defect size and shape. This could be explained by understanding the heat diffusion mechanism. For this purpose, 1 D analytical modelling was carried out for a semi infinite 316 L SS plate and a defect of depth of 1.13 mm. The temperature response was computed using eqns 2.16 and 2.17 respectively. From the temperature data obtained from modelling, temperature contrast, contrast derivative, log first derivative and log second derivative were computed and respective peak times were

obtained. Figure 3.12 shows the theoretical and experimental temperature contrast variation with time and comparison between the theoretical peak times for defect of depth 1.13 mm.

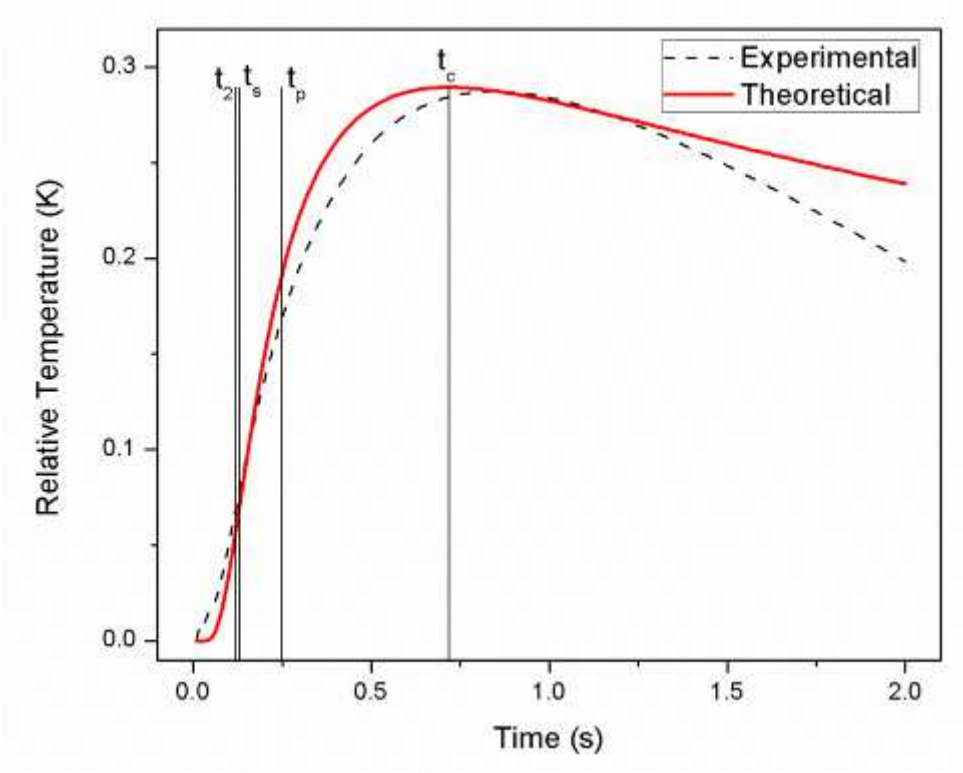

Figure 3.12: Experimental and theoretical temperature contrast plot and comparison of peak times

The comparison between theoretical and experimental temperature contrast curves clearly shows a good agreement between them at the initial stage. With the passage of time, the rate of decay is faster for the experimental curve compared to the theoretical curve. This is because at the initial stage thermal waves reflecting from defect interface follow the 1 D heat flow [63]. With the passage of time, lateral diffusion of thermal waves become predominant since the surrounding area is at a lower temperature. Hence as time increases, the 3 D heat diffusion (lateral diffusion) becomes more predominant causing temperature contrast curve to decreases rapidly (fig. 3.12) which is not observed in theoretical curve since it is based on 1 D approach and does not take into account the lateral diffusion. From

fig. 3.12 it is also observed that t_s and t_2 occur at an early stage where 1 D heat diffusion is predominant while t_p occurs at an intermediate stage where lateral diffusion has just begun and t_c occurs at later stage where 3 D heat diffusion is predominant.

An important factor to be considered in PT is the size of the region surrounding the defect. The non defective region surrounding the defect increases when defect size decreases. Increased non defective surrounding region aids the lateral diffusion of heat. Hence thermal waves over smaller defect area diffuse very quickly. It can be observed that peak temperature contrast time occurs at time where lateral heat diffusion is predominant. Hence temperature contrast curve peaks at early stage for smaller size defects (fig. 3.9 (a)). From fig. 3.9 (a) it is also observed that as defect size decreases the peak amplitude of contrast curve also decreases. This is because as the defect size decreases, the amount of thermal waves reflected by it also decreases, thus causing a lower temperature rise for smaller defects when compared to larger defects. The same behavior is observed in case of log first derivative method as seen in fig. 3.9 (c). But much variation in peak time is not observed as in case of temperature contrast, since the peak log first derivative time occurs at intermediated stage, where lateral diffusion has begun. Peak contrast derivative time and peak log second derivative times are not affected by defect size as seen in fig. 3.9 (b) and (d). This is because t_s and t_2 occurs at early stage where 1 D heat diffusion is predominant. The amplitude of response curves in both the cases is not affected by defect size, since in this case the plot is not affected by lateral diffusion of heat. The same explanation holds good for the effect of defect shape.

The peak time in different methods were computed for defects of different depths and size and are compared in fig. 3.13. Figure 3.13 (a) – (c) shows the variation of peak times with defect size for defects of depth 0.4 mm, 1.13 mm and 1.78 mm respectively. From the figure it is clear that defect size has greater effect on peak temperature contrast

time, moderate effect on peak log first derivative time and least effect on peak contrast derivative and peak log second derivative time. This is again confirmed in fig. 3.13 (d) which is the plot of average peak time for defects of depth 1.13 mm and different size calculated from above discussed methods. The error bar represents the standard deviation in the measurement of peak time for defects of different size. The standard deviation is large for temperature contrast method, while it is intermediate for log first derivative method and least for contrast derivative and log second derivative methods.

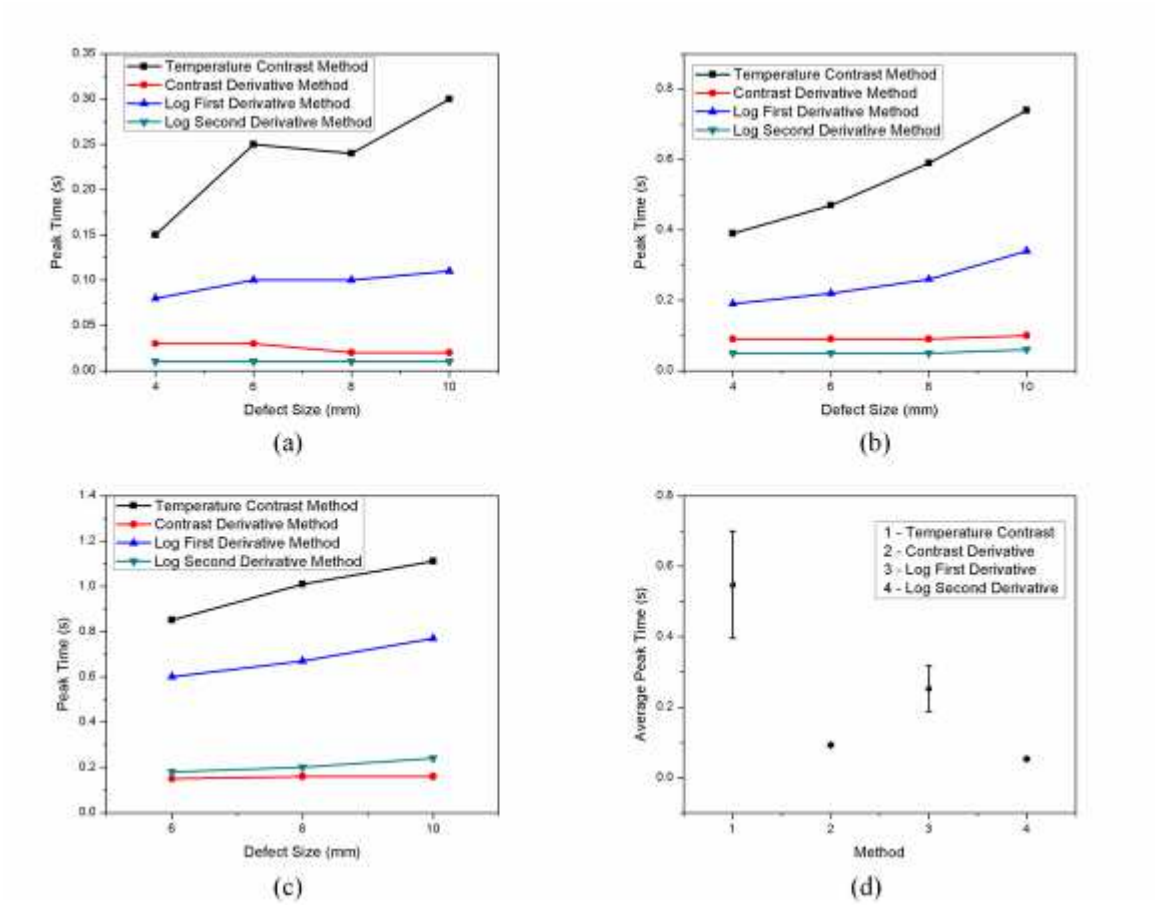

Figure 3.13: Plot showing the variation of peak times as a function of defect size in different methods for defects of depth (a) 0.4 mm (b) 1.13 mm (c) 1.78 mm (d) Plot of average peak time obtained from different methods and the corresponding standard deviation

Figure 3.14 is the plot of variation of peak time in case of defects of shape square, circle and rectangle for depth 1.13 mm. The fig. 3.14 shows that the peak contrast time is largely affected by defect shape while log first derivative is moderately affected by defect shape. Whereas peak contrast derivative and peak log second derivative times were least affected by defect shape. Same explanation of heat diffusion around defects holds good here too.

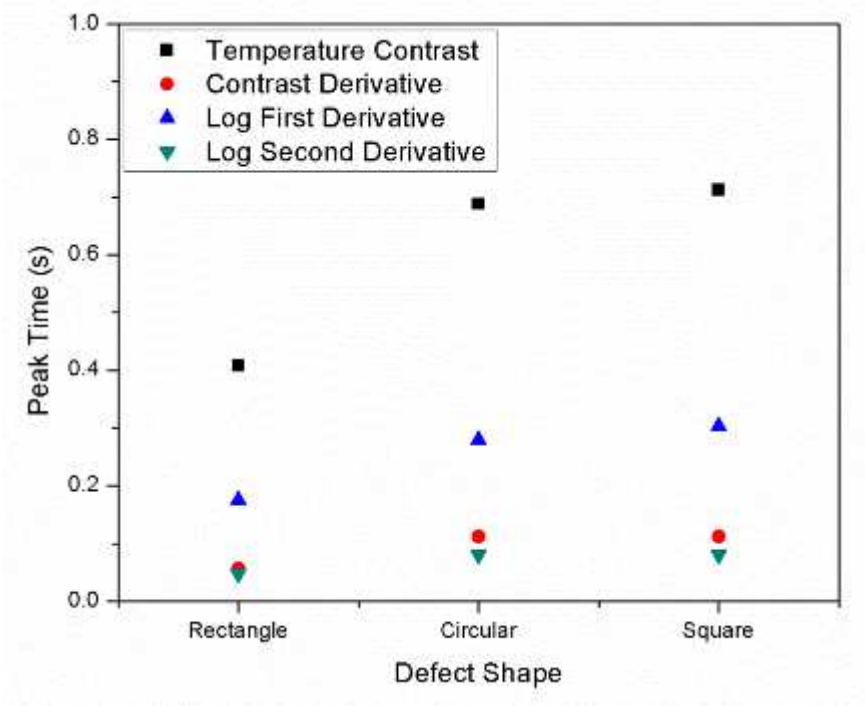

Figure 3.14: Effect of defect shape on peak time in case of all the methods

3.5.3 Defect Sizing

In PT, the size of the defects can be measured by drawing a line profile over the defective area, which is a Gaussian distribution of temperature and measuring the Full Width at Half Maximum (FWHM). Figure 3.15 shows the line profile of defects of size 10 mm x 10 mm at different time intervals. The figure clearly shows that the FWHM as well as the amplitude decreases as the time passes. This is due to the diffusion of thermal waves around the defect causing the defect to disappear as time passes. Hence FWHM will not give the actual size of defect. Hence decrease in FWHM has to be taken care while

measuring the defect size. An empirical relation has been proposed by Almond et al [68] to overcome this effect and is given in the following equation.

$$FWHM = D - 1.08(\alpha t)^{1/2}\, mm \qquad (3.9)$$

where D is actual defect size, α is thermal diffusivity of the material. Hence D at t = 0 should give the actual size of the defect. The FWHM at different time intervals are measured, straight line is fitted to the data and the intercept gives the actual defect size.

The sample was kept at a distance where it covers the maximum area in the FOV to get the good spatial resolution. For a distance of 35 cm, the spatial resolution obtained was 0.45 mm. Defects with depth 0.4, 1.13 and 1.78 mm with 10 mm size were chosen for size measurement. The FWHM for each defect was computed and plotted as a function of time as shown in fig. 3.16. In Table 3.3, comparisons between actual and measured sizes were done and the errors associated with the measurement are also given. It can be observed that the maximum error in size measurement is 4.8%.

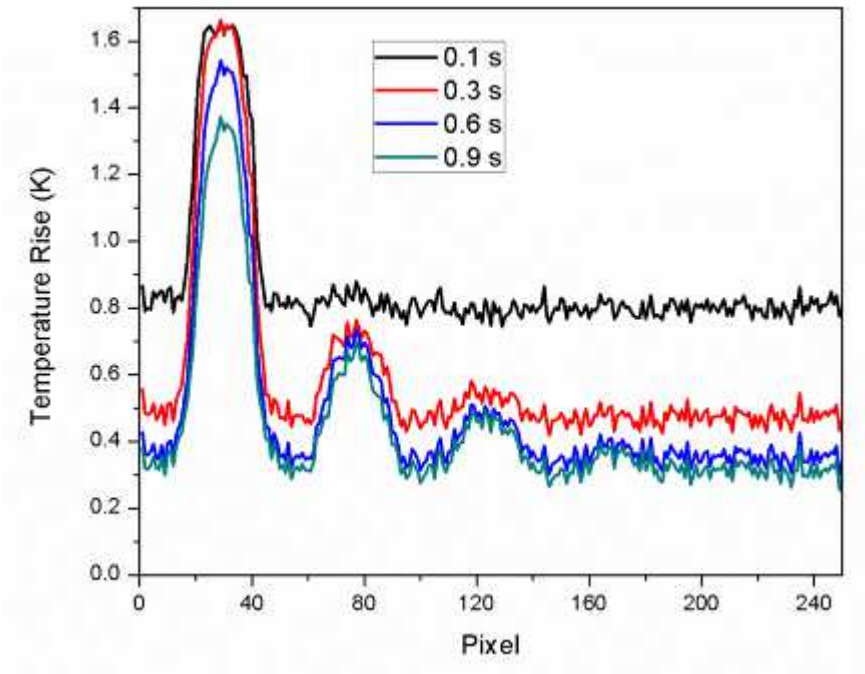

Figure 3.15: Line profile over defective area at different time intervals

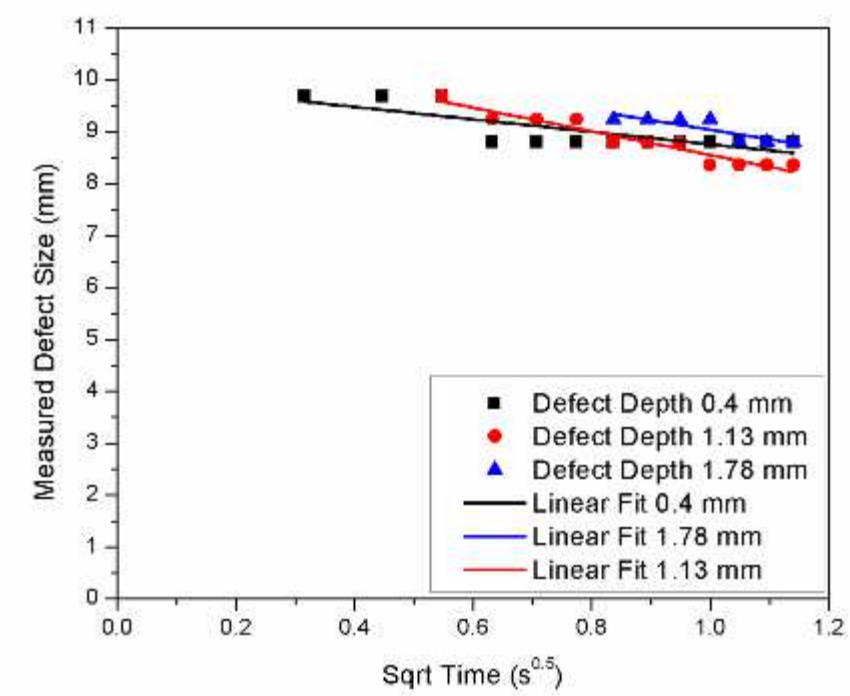

Figure 3.16: Defect size variation as a function of square root of time

Defect Depth (mm)	**Defect Size (mm)**		
	Actual	Measured	% Error
0.4	9.99	9.96	0.3
1.13	9.94	10.83	8.9
1.86	9.9	10.89	10

Table 3.3: Defect size measurement

3.5.4 Repeatability

In any experiment repeatability is an important parameter which has to be checked. In the present study, to check the repeatability, the experiment was conducted on the same sample for 6 times with same experimental parameters. The peak time in each case was computed and the average peak time plotted (fig. 3.17). The error bar represents the standard deviation in the measurement. The maximum deviation associated in peak time

measurement in case of contrast derivative, log first derivative and log second derivative methods is 0.03 sec where as for temperature contrast method it is 0.06 second. From fig. 3.17 it can also be observed that as the defect depth increases, the error in peak time measurement also increases. This is because, as the defect depth increases thermal signal strength decreases which introduces the uncertainty in measurement. The deviation in the measurement is within acceptable limit.

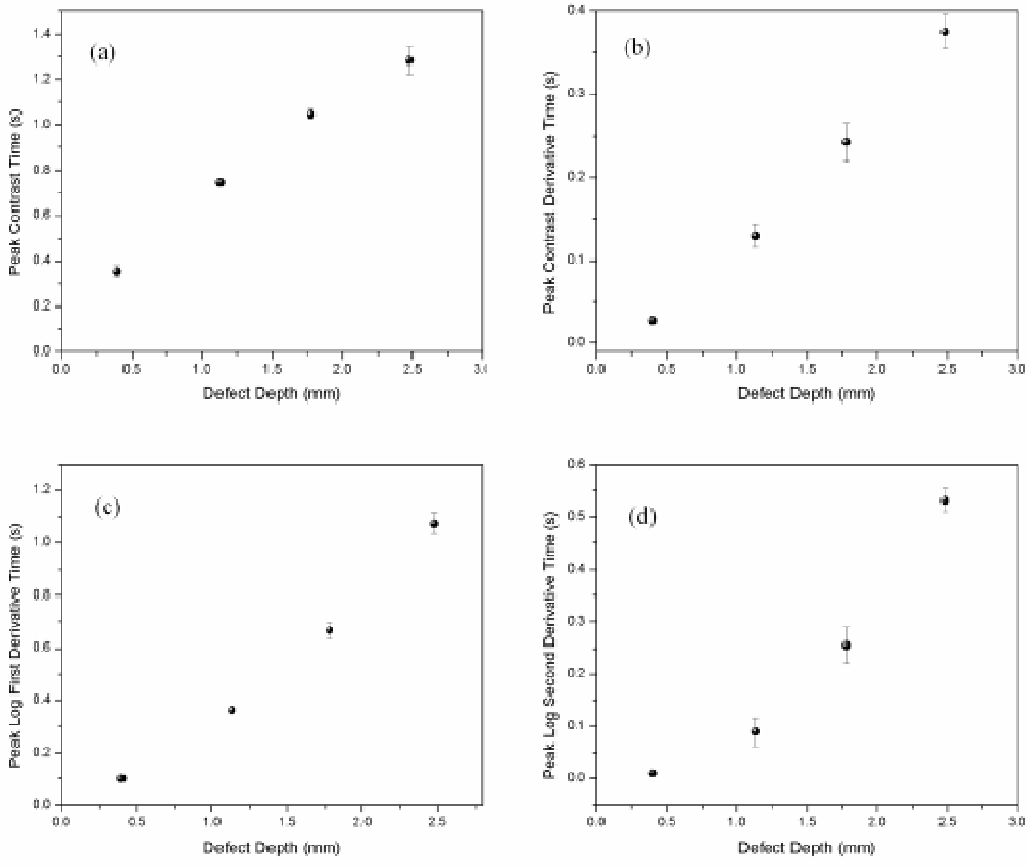

Figure 3.17: Average peak time variation as a function of defect depth for (a) temperature contrast (b) contrast derivative (c) log first derivative (d) log second derivative methods

The above experiments and the analysis clearly reveal that contrast derivative and logarithmic second derivative method are more accurate in defect depth quantification. The effect of defect size and shape on depth quantification was also studied. This study revealed that contrast derivative and logarithmic second derivative method are least

affected by defect size and shape, since they occur at early stage. The study also revealed that heat diffusion around the defect plays an important role in defect depth quantification. The error in depth quantification and dependence of peak time on defect size and shape mainly depends on the lateral heat diffusion. In PT, any method which predicts the time of deviation at early stage is more suitable for depth prediction since as they occur at 1 D heat transition regime, they are independent of defect size and shape. The defect sizing study revealed that defect size could be measured with good accuracy using PT. The study shows that contrast derivative and log second derivative methods are best for depth quantification. But contrast derivative method has the inherent disadvantage of need of reference region for contrast computation. Hence log second derivative method is best for depth quantification in PT.

CHAPTER 4
DEFECT CHARACTERIZATION USING LOCK IN THERMOGRAPHY

4.1 Introduction

The basic idea of Lock in Thermography (LT) is that the temperature modulation induced externally through a modulated light source excites the object surface. This results in a thermal wave which propagates inside the material and undergoes reflections at interfaces / boundaries of defects like all other waves. The temperature modulation at the surface is modified by the interference of the thermal waves reflected from within the component with the incoming waves. By monitoring the temperature field during the modulated illumination with an IR camera and performing a Four Point Correlation (FPC) analysis each pixel one can extract the amplitude and phase which can be represented as images. The amplitude image is affected by inhomogenities of optical surface absorption, infrared emission and distribution of optical illumination. The phase value is computed by taking the ratio of temperature information (Eqn. 2.23). Since the ratio nullifies the emissivity variation in the signal, the phase image is invariant to emissivity variations. Phase images also provide more information as the penetration of the thermal wave in phase image is 1.6 times the thermal diffusion length compared to amplitude image [92]. Due to this reason it is preferred to work with phase image for defect depth evaluation. In LT, the important factors that affect defect detection are phase contrast and blind frequency which is discussed in detail in this chapter. Defect detection in composites and polymers, coating thickness evaluation using LT is well studied [116, 124, 130, 111, 112]. On Stainless Steel (SS), this study is sparse [115, 122]. Depth prediction in LT has not been studied in a systematic and detailed manner. Two methods are proposed in literature

namely blind frequency method [117] and phase contrast method [166] for depth prediction. The strength of thermal waves reflected from near surface defect is stronger than the deeper defects which causes higher phase shift for near surface defect. Thus, the phase contrast for near surface defect is higher than the deeper defect. The blind frequency for near surface defect is also higher than for the deeper defect. This allows the quantification of depth by measuring either phase contrast or blind frequency as a function of defect depth. However, a detailed study of depth prediction has not been done. In the present chapter, the aspects of defect detection using LT in AISI type 316 L SS and depth prediction methods are discussed. Effect of defect size and shape on depth prediction is studied and sizing of defect using LT has also been successfully attempted.

In the present experimental work, two halogen lamps (1000 W each) kept at a distance of 40 cm from the camera were used for illumination. The IR camera was placed at a distance of 35 cm and a frame rate of 25 Hz was used. This frame rate ensures that the Niquist criterion is satisfied. The experiment was conducted over the frequency range 0.01 Hz to 0.9 Hz so that it covers the depth range.

4.2 Defect Detection Using LT

In this section, the aspects of defect detection using LT are discussed. The important parameters are thermal diffusion length, blind frequency and phase inversion, which are discussed below.

Thermal Diffusion Length (μ): Thermal diffusion length is one of the important parameter in LT. Thermal waves attenuate as they travel through material. μ is the distance at which the thermal wave attenuates to 37 % of its original strength. Thermal diffusion length is given by following equation [131],

$$\mu = \sqrt{\frac{\alpha}{\pi f}} \qquad (4.1)$$

where α is the thermal diffusivity and f is the excitation frequency. From eqn 4.1, one can observe that μ and f are inversely related. Lower frequencies probe deeper in a material while higher frequencies are confined to near surface. Hence frequency of excitation has to be appropriately selected for the experiment depending on the defect depth.

Phase Contrast: The experiment was carried out over the frequency range of 0.01 Hz to 0.9 Hz. Phase contrast was computed by taking the phase angle difference between the defective area and sound area. The plot of phase contrast as a function of frequency and amplitude as a function of frequency is shown in fig. 4.1. It can be observed from the fig.4.1 that, the phase contrast is negative at lower frequencies. That means the phase angle of defective region lags from that of sound area. The phase contrast increases, in negative scale, as frequency increases. It peaks at a particular frequency and then starts decreasing (in negative scale). This frequency is called optimum frequency. As frequency is further increased, the phase contrast becomes zero and starts increasing in positive scale. The amplitude decreases exponentially with frequency. For two different depths (0.4 mm and 1.13 mm) the optimum frequency is 0.07 Hz (fig 4.1). The optimum frequency mainly depends upon the thickness of the object under inspection and its thermal diffusivity. Figure 4.2 is the phase image and amplitude image of the sample with square defects at optimum frequency. From the figure, it is observed that, phase image gives better defect visualization than the amplitude image. Phase image clearly detects defects of size 10 and 8 mm which are at depth 2.48 mm and defects of smaller size (4 mm x 4mm) at depth 1.78 mm were also clearly seen. But in amplitude image, deeper defects were not observed also smaller defects at depth 1.78 mm were not seen. This is due to the depth, in case of amplitude, is of the order of thermal diffusion length ($L \approx \mu$) where in phase image depth

is 1.6 times the thermal diffusion length (L ≈ 1.6μ) [92]. Hence phase image is considered for analysis.

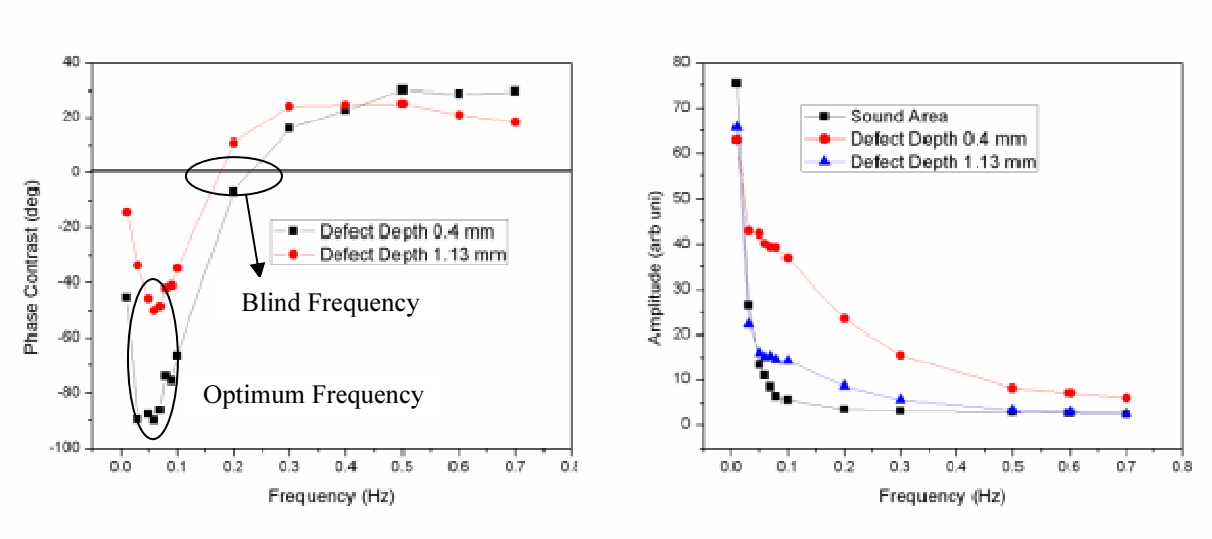

Figure 4.1: Phase contrast and amplitude variation as a function of frequency for defects of size 10 mm x 10 mm

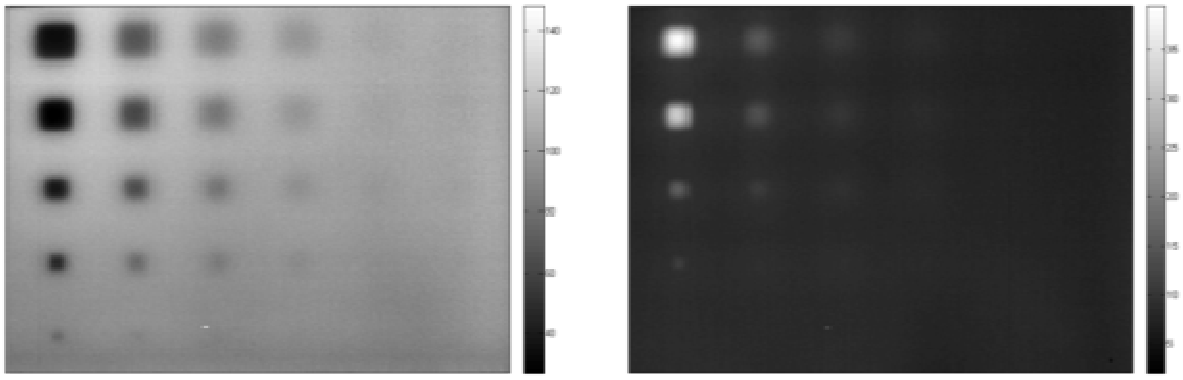

Figure 4.2: Phase and amplitude images of sample with square defects at optimum frequency (0.07 Hz)

Phase Inversion: Another important issue in LT is phase inversion and blind frequency. As seen in fig. 4.1, at lower frequency, the phase angle of defective area lags that of non defective area hence we get negative phase contrast. As frequency increases, this difference decreases and at a particular frequency, the phase angle of defective area

becomes equal to the non defective area leading to zero phase contrast. This frequency at which the phase contrast is zero is referred to as 'blind frequency'. At the blind frequency, the defect "appears to disappear". With further increase in the frequency, the phase angle of defective area leads the phase angle of non defective area causing a positive phase contrast. The phase contrast which is initially negative at lower frequencies becomes positive for higher frequencies and this change in phase contrast is referred to as 'phase inversion'. Phase inversion is clearly seen in fig. 4.3 which is the phase images at frequencies 0.07 Hz and 0.5 Hz. The defective area was dark at frequency 0.07 Hz whereas at 0.5 Hz, it appears bright when compared to sound area. Figure 4.4 is the phase images of defect of size 10 mm x 10 mm at frequencies 0.1 Hz, 0.15 Hz and 0.2 Hz. The image clearly shows the effect of blind frequency. At frequency 0.1 Hz the deeper defect (4^{th} from left, in square box) was observed with negative phase contrast, at 0.15 Hz the defect disappears and at 0.2 Hz it appears with inverted contrast (Phase inversion).

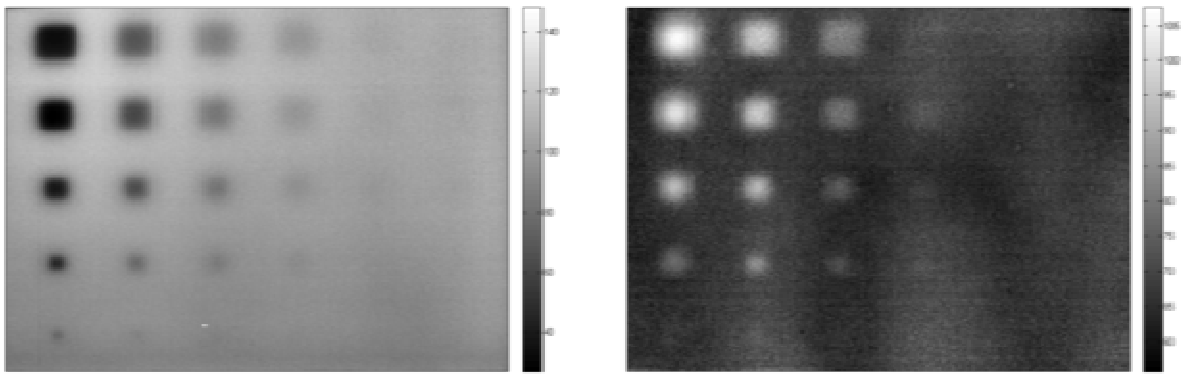

Figure 4.3: Phase images of sample with square defects at frequencies 0.07 Hz and 0.5 Hz

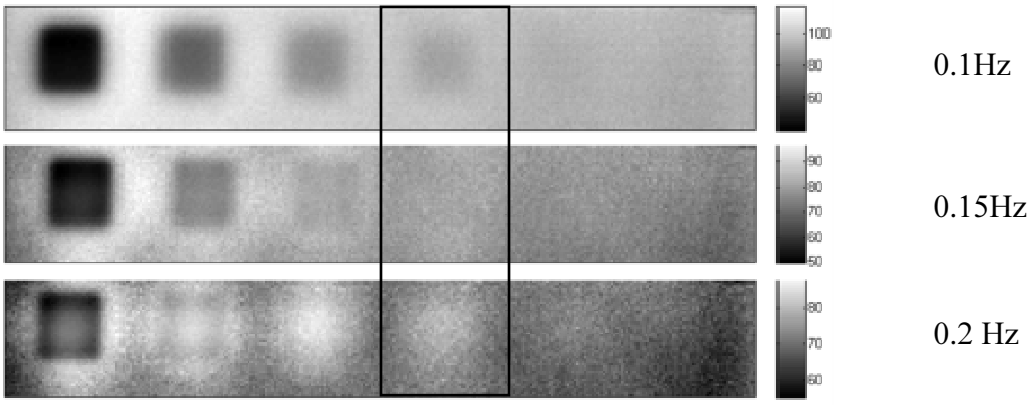

Figure 4.4: Phase images at 0.1 Hz, 0.15 Hz and 0.2 Hz of defects of size 10 mm x 10 mm

While conducting LT, one should take care of blind frequency, since there is a chance of missing the defect if the experiment is carried out at single frequency. If the defect depth is unknown, one has to perform experiment in a certain frequency range. The choice of frequency depends on the sample thickness and thermal diffusivity of the material (eqn. 4.1)

4.3 Depth Quantification

Depth quantification study is carried out by two methods reported in literature namely blind frequency method and phase contrast method.

4.3.1 Blind Frequency Method

In Pulsed Phase Thermography (PPT), blind frequency is widely used for depth quantification [97, 134, 136]. Blind frequency is a function of defect depth. The interference effect of shallower defect is strong, since thermal waves have good strength when compared to deeper defects. This result in greater phase angle difference when compared to sound area and deeper defects will have lower phase contrast. Thus deeper defects will have lower blind frequency than the shallower defects.

The thermal diffusion length measured at the blind frequency is the function of defect depth [117]. The relationship between defect depth and blind frequency is given by the following equation,

$$L = C\sqrt{\frac{\alpha}{\pi f_b}} \qquad (4.2)$$

where C is constant, f_b is the blind frequency for defect of depth L.

The reported value of C in literature for composite materials is 1.8-1.88, using PPT [134]. This value has not been reported using LT. For AISI type 316 L SS, value of C has not been reported. To calculate C, theoretical analysis was carried out using Bennett and Patty (BP) model [93].

BP model was originally proposed for the photoacoustic methods. LT and photoacoustic method works on the same principle, the way the output is detected is different. In LT, the modulated light source causes periodic variation in surface temperature which is measured using IR camera and FPC is performed to get the amplitude and phase information. In photoacoustic method, the photoacoustic cell is attached to the surface of the sample which is exposed to modulated light source that causes periodic variation in surface temperature. The temperature changes pressure in the photoacoustic cell which results in generation of acoustic signals which are detected and used for analysis. If the sample is thermally thin, then thermal waves will undergo interference causing change in amplitude and phase angle measurement. The change in phase angle of thermally thin sample and reference sample, which is assumed to be thermally thick, is given by the following equation,

$$\Delta\varphi = \tan^{-1}\left\{\frac{-R_b\left(1+R_g\right)\exp\left(-2a_sL\right)\sin\left(2a_sL\right)}{1-R_g\left[R_b\exp\left(-2a_sL\right)\right]^2+R_b\left(1-R_g\right)\cos 2a_sL}\right\} \qquad (4.3)$$

where R_b and R_g are the reflection coefficients of sample-backing material interface and sample-gas interface respectively. a_sL is the thermal thickness of the material where a_s is the inverse of thermal diffusion length ($a_s = 1/\mu$). Equation 4.3 could be used for theoretical analysis of LT, since the equation deals with the thermal wave propagation inside the material, which is same in case of LT and photoacoustic method. In LT, there is no backing material, hence the sample-air interface can be considered as the sample-backing material interface, which is also true for gas-sample interface (front side).

The theoretical analysis is carried out using MATLAB software and the parameters used for analysis is given in table 4.1. The analysis was done for defects at depths 0.4 mm, 1.13 mm, 1.78 mm and 2.48 mm. The variation of phase angle difference as a function of square root of frequency is shown in fig. 4.5 (a). The plot shows that the near surface defects have higher blind frequency when compared to deeper defects. The blind frequency was measured for each defect and thermal diffusion length at blind frequency was calculated. According eqn. 4.2, the plot of defect depth and corresponding diffusion length at blind frequency should be a straight line, passing through the origin with slope C. To obtain the constant C, defect depth is plotted as a function of thermal diffusion length at blind frequency. Then a linear fit is carried out on the data as shown in fig. 4.5 (b). The analysis showed that the linear fit matches the analytical result with $R^2 = 1$ and slope = C = 1.57.

Parameters	**Stainless Steel**	**Defect**
K (W/m*K)	16.2	0.0257
ρ (kg/m^3)	7990	1.125
c_p (J/(kg*K)	500	1005
μ (m^2/s)	4x10^{-6}	22.7x10^{-6}
e (J/m^2*K*s$^{0.5}$)	8045	5.39

Table 4.1: Thermal properties of AISI 316 L SS and air (defect) used for BP model

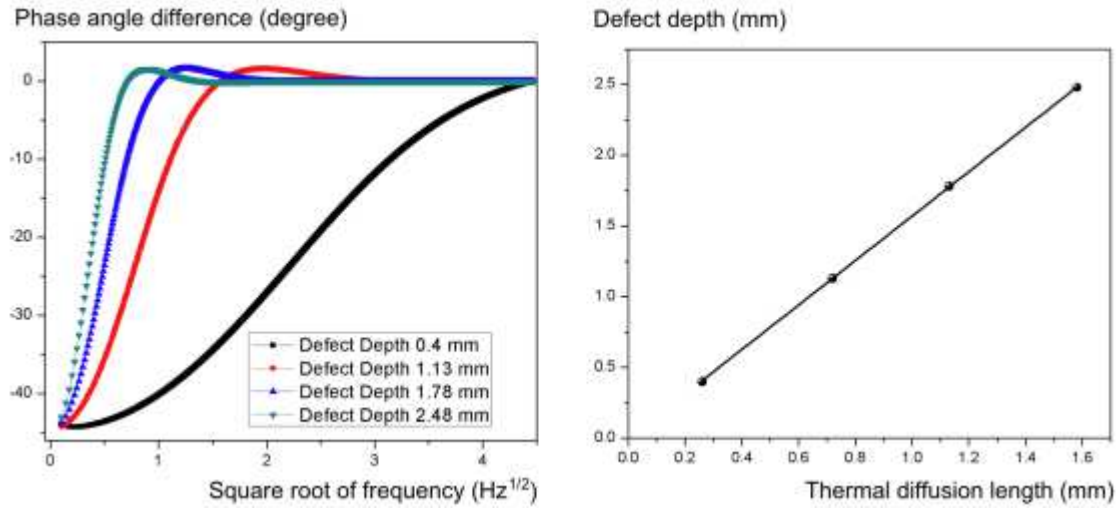

Figure 4.5: (a) Plot of phase angle difference variation as a function of square root of frequency obtained from Benett and Patty model for defects of various depths (b) Defect depth variation as a function of thermal diffusion length at blind frequency

Since LT experiment consumes time, the experiment was initially carried out over a frequency range 0.01 to 0.7 Hz with a frequency step of 0.1 Hz. Then the phase contrast value was computed for defects of size 10 mm x 10 mm at various depths and plotted as a function of frequency (fig. 4.1). Now where the phase inversion occurs, the experiment was conducted at that frequency range with frequency step 0.02 Hz for defects of various depths. Then the phase contrast value was computed and plotted as a function square root of frequency. It was observed that polynomial of order 3 gives better fit to the curve as shown in fig. 4.6. The blind frequencies were then measured for defects of various depths and thermal diffusion length at blind frequency was computed. Then the defect depth is plotted as a function of diffusion length as shown in fig. 4.7 (a). From figure we can observe that though it follows the straight line trend, but does not pass through origin, as expected from theoretical analysis. The value of C is computed for each defect depth and a plot of C as a function of defect depth is shown in fig. 4.7 (b). From fig. 4.7 (b), it is observed that C is not a constant as concluded from theoretical analysis, but it is a function of defect depth also. The value of C is lower than the expected value 1.57. The comparison

between theoretical blind frequency and experimental blind frequency shows that theoretical value is higher than the experimental value.

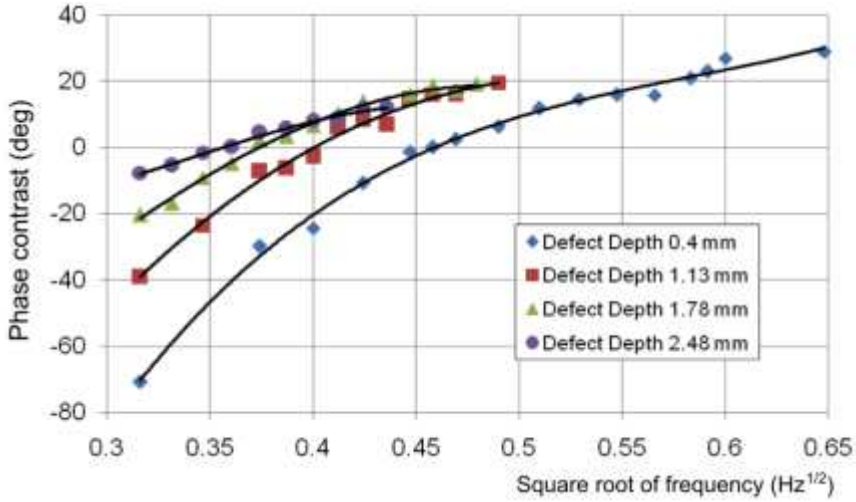

Figure 4.6: Phase contrast variation as a function of square root of frequency (Experimental)

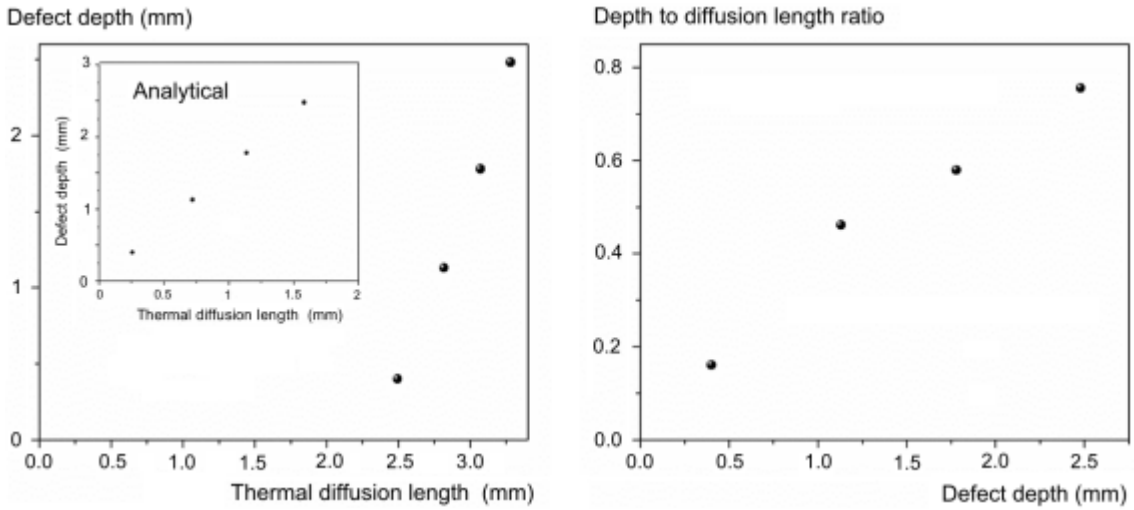

Figure 4.7: (a) Defect depth vs thermal diffusion length at blind frequency (b) Depth to diffusion length ratio (C) as function of defect depth for square defects of size 10 mm x 10 mm.

To explain the deviation from theoretical prediction, we have considered effect of defect size and shape on blind frequency. The phase contrast was computed for defects of

size 10 mm x 10 mm, 8 mm x 8 mm, 6 mm x 6 mm and 4 mm x 4 mm located at a depth of 0.4 mm and plotted as a function of square root of frequency as shown in fig. 4.8 (a). From fig. 4.8 (a), it can be observed that blind frequency increases as defect size decreases and smaller defect has more effect on blind frequency than the larger defect. This is clearly seen in fig. 4.8 (b), which is the plot of variation of blind frequency as a function of defect size. The experiment was repeated with the same parameters as used in the earlier experiment for defects of different shape (circular, square and rectangular). Then the blind frequency was computed for defects of different shape at depth 0.4 mm and is shown in fig. 4.9. From the figure, it can be observed that rectangular shaped defect has greater influence on blind frequency while circular and square shaped defects have comparable blind frequencies. Hence the blind frequency is not only a function of defect depth but also a function of defect size and shape.

The theoretical analysis is a one dimensional approach, where as in the actual case thermal waves follow three dimensional heat flows. This causes the low value of experimental blind frequency when compared to theoretical value. Another source of error is the choice of reference material. In theoretical analysis, the reference is thermally thick (semi infinite material) but it is not true in case of experiment, the reference area chosen in experiment has finite thickness. This also contributes to the deviation in the blind frequency measurement. The theoretical analysis does not account for the effect of defect size and shape which influences the blind frequency to a greater extent. Hence blind frequency cannot be considered as an accurate method for depth quantification.

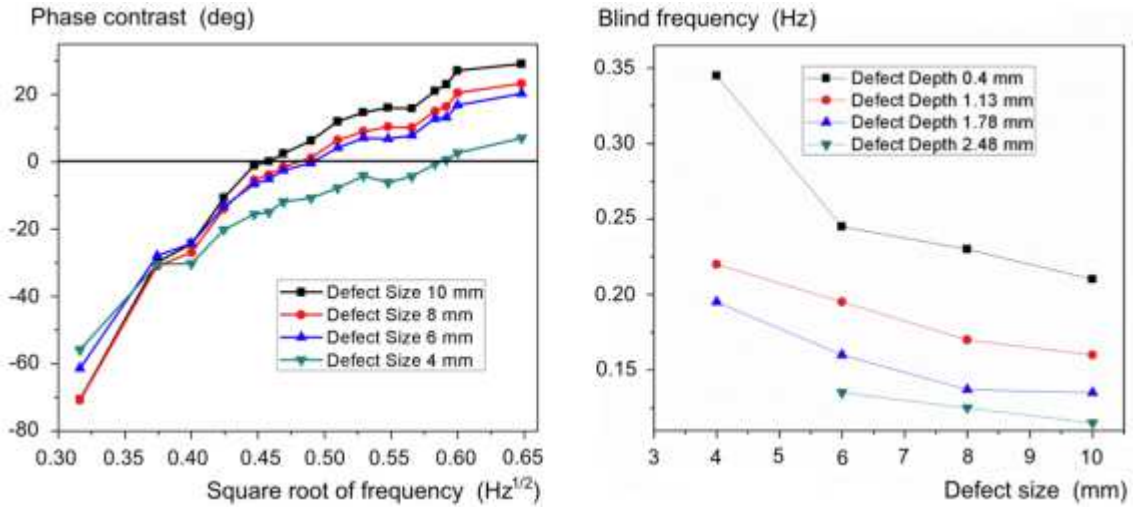

Figure 4.8: (a) Variation of phase contrast as a function of frequency for defects of various sizes (b) Variation of blind frequency as a function of defect size

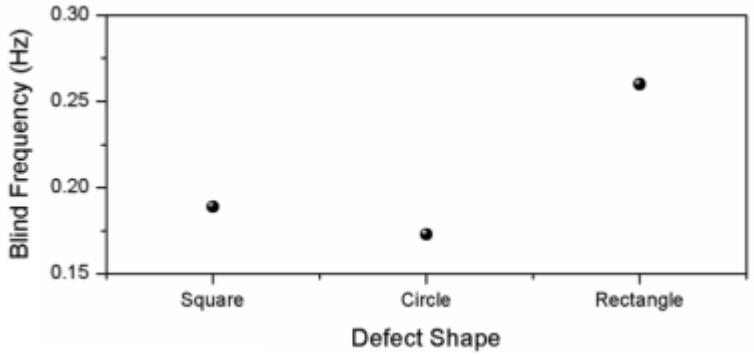

Figure 4.9: Variation of blind frequency for defects of shape square, circular and rectangle at depth of 0.4 mm

4.3.2 Phase Contrast Method

An alternate approach proposed for depth quantification is the phase contrast method [166]. Phase contrast decreases as defect depth increases. This is because, as thermal waves from deeper defect reaches the surface, they are highly damped resulting in a weak signal. Hence phase contrast could be used as a measure of defect depth. Phase image at optimum frequency was considered for analysis (0.07 Hz), since at optimum frequency maximum number of defects is detected.

The phase contrast was computed by taking the average phase angle over a defective area and an adjacent non defective area. A rectangle area was selected and the pixel values were averaged over the area to reduce the fluctuation. Since we are working on single frequency, absolute phase contrast was considered. Figure 4.10 is a plot of defect depth vs phase contrast. It can be observed that the curve is non linear. A polynomial of order 3 (eqn. 4.4) was observed to gives best fit with $R^2 = 0.998$

$$L = -8x10^{-6}(\Delta\varphi)^3 + 0.0014(\Delta\varphi)^2 - 0.0974\,\varphi + 3.51 \qquad (4.4)$$

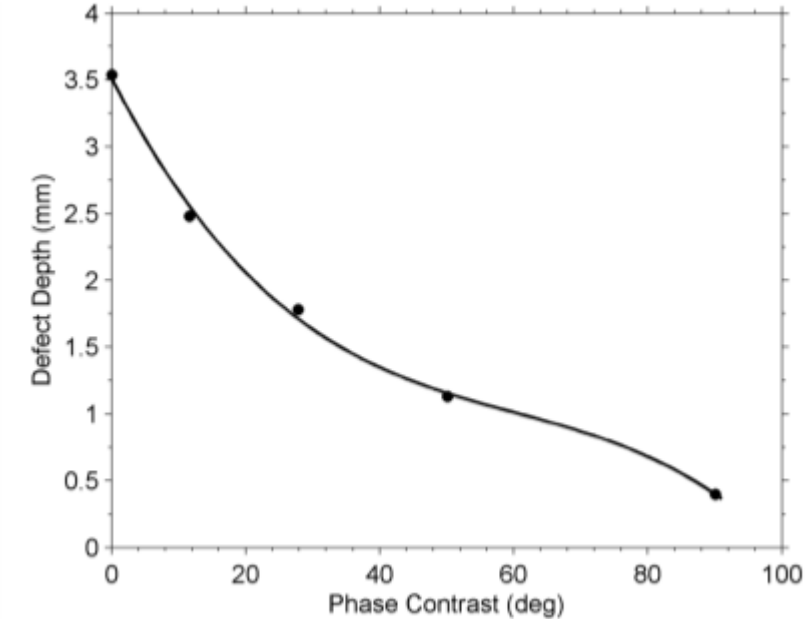

Figure 4.10: Plot of defect depth vs phase contrast with polynomial fit of order 3 for defects of size 10 mm x 10 mm.

This is used as calibration plot. The intercept of the fit gives the phase angle value of sound area. To evaluate the efficiency of the above generated calibration plot, the experiment was conducted on another square defect sample under identical experimental conditions. Phase contrast was measured for defects of size 10 mm at various depths (unknown) and the depth was estimated using eqn. 4.4. The actual depth, predicted depth

and the error is given in table 4.2. From the table we can observe that the error percentage involved in measurement is minimum (less than 10 %).

Actual Depth (mm)	Predicted Depth (mm)	% Error
0.5	0.47	6.0
1.15	1.22	6.1
1.83	1.91	4.4

Table 4.2: Depth prediction using phase contrast method and error associated with it

To study the effect of defect size on phase contrast, defects of size 10 mm x 10 mm, 8 mm x 8 mm, 6 mm x 6 mm and 4 mm x 4 mm were considered. The phase contrast was computed for each defect and is plotted in fig. 4.11. From the figure it can be observed that phase contrast decreases with decreasing defect size for a fixed defect depth. Hence the phase contrast of larger defect located at deeper depth may be same as phase contrast of smaller defect located at near surface. This will lead to error in measurement. Hence the calibration plot generated should be independent of defect size. Hence a dimensionless parameter, defect size to depth ratio, is defined and a plot of defect size to depth ratio and phase contrast is plotted in fig. 4.12. The curve follows a non linear trend and polynomial of order 4 is fitted which gives better fit.

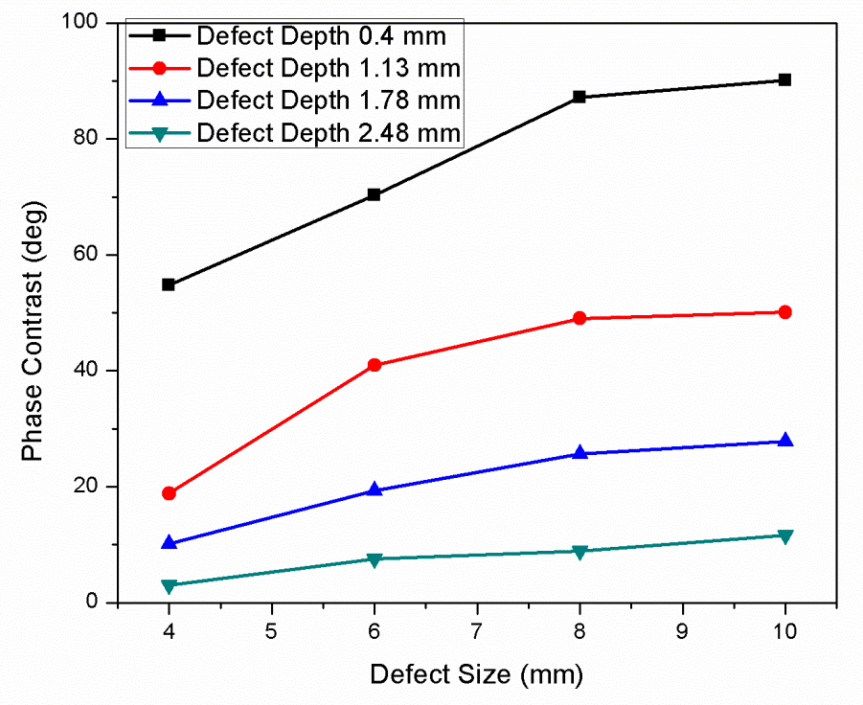

Figure 4.11: Variation of phase contrast as a function defect size located at various depths for square defects

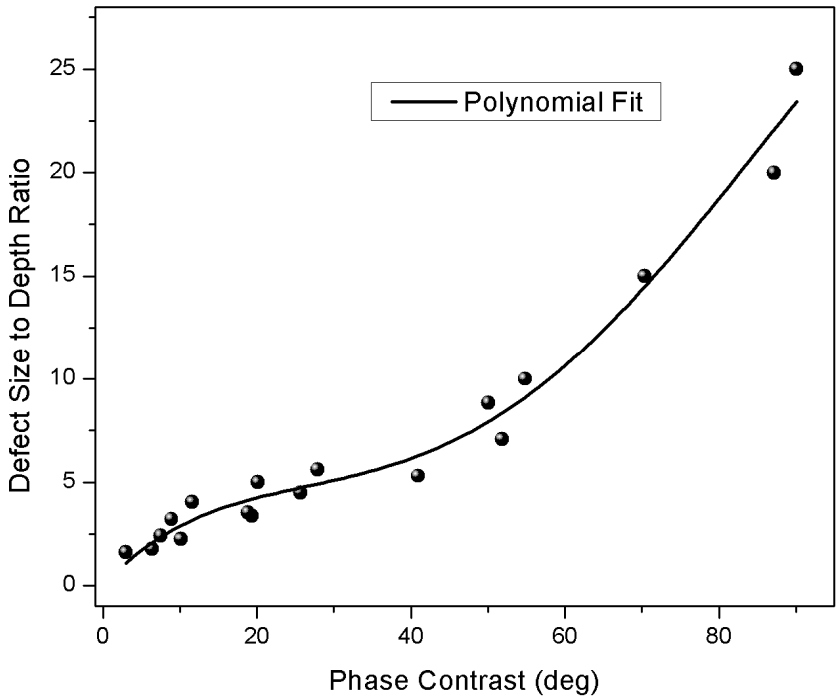

Figure 4.12: Plot of dimensionless parameter defect size to depth ratio vs phase contrast and polynomial fit of order 4

This dimensionless parameter holds well if defect is square in shape. If defect has a rectangular shape, then the validation of this method has to be evaluated. To study this, the experiment with same parameters as above, was conducted with another sample with defects rectangular in shape and with an area that was half of that of square defect and the defect length is double of defect breadth. Phase contrast was computed for each defect. While conventionally, defect size refers to the defect length, in the present case, we have investigated the effect of phase contrast with length to depth ratio and also breadth to depth ratio. This is graphically represented in figs. 4.13 (a) and 4.13 (b) respectively. The solid line in the figure is the fitted line for square defects. From fig. 4.13 (a) it can be observed that the defect length to depth ratio underestimates the phase contrast where as defect breadth to depth ratio overestimates the phase contrast (fig. 4.13 (b)). This is because the phase contrast value for square defect (size 10 mm x10 mm) and rectangular defect (size 10 mm x 5 mm) is different. This is illustrated in fig. 4.14 which is phase contrast variation as function of defect size. The square and rectangle defects have same length but the area is different. Square defect has an area of 100 mm^2 while for rectangular defect it is 50 mm^2. The larger area in the case of square defects will result in more thermal waves getting reflected in case of square defects compared to rectangular defects leading to higher contrasts for square defects compared to rectangular defects. This also explains the reasons for over and under estimation. This also indicates that defect size to depth ratio cannot be relied upon for accurate depth predictions. Hence a new dimensionless parameter, square root of defect area to defect depth (S) is proposed. Figure 4.15 is the plot of S vs phase contrast in case of rectangular defects fitted using polynomial of order 3.

The experiment was repeated for square, circular and rectangular defects and the phase contrasts computed in each case. Then a plot of S vs phase contrast was plotted as

shown in fig. 4.16. The plot follows a non linear trend as expected and fitted with polynomial of order 3.

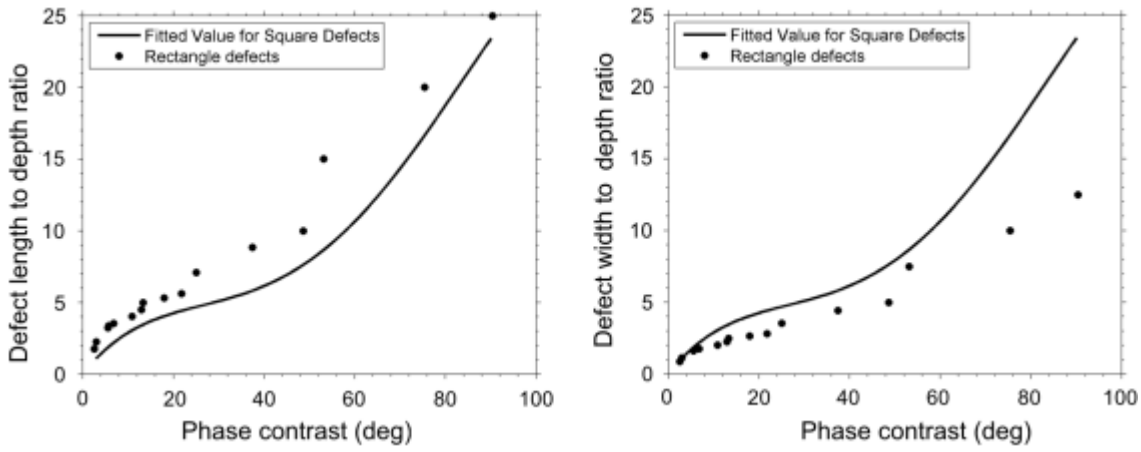

Figure 4.13: (a) Defect length to depth ratio vs phase contrast (b) Defect breadth to depth ratio vs phase contrast for defects of shape rectangle

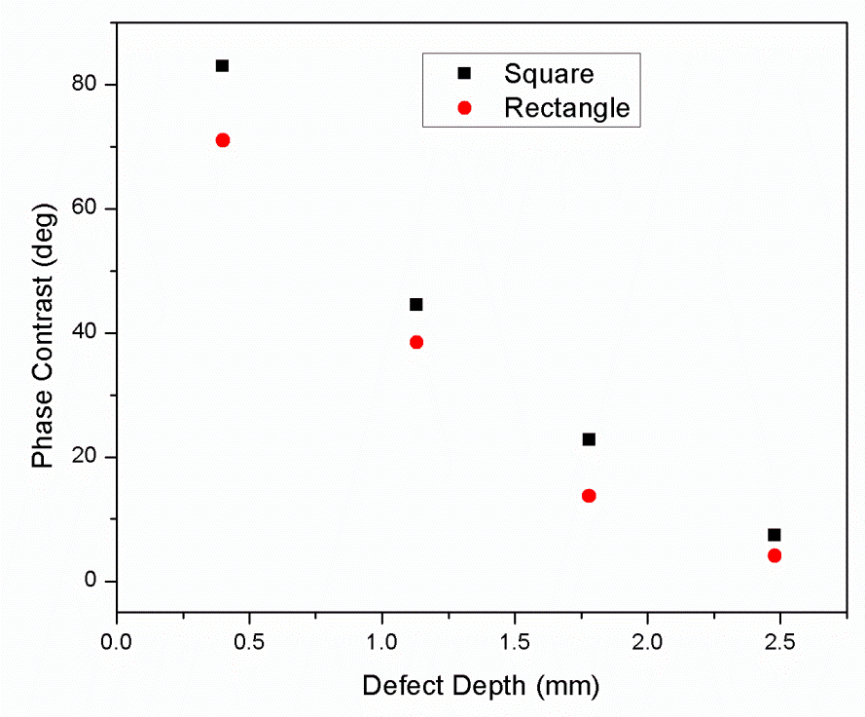

Figure 4.14: Variation of phase contrast as a function of defect depth for defects of shape square and rectangle

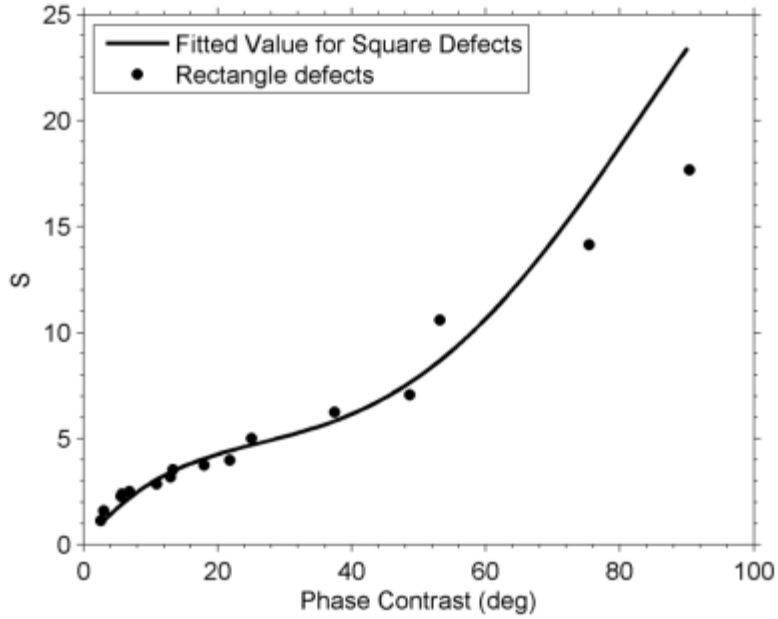

Figure 4.15: Square root of defect area to depth ratio, S, vs phase contrast plot for rectangular defects and comparison with fitted value of square defect

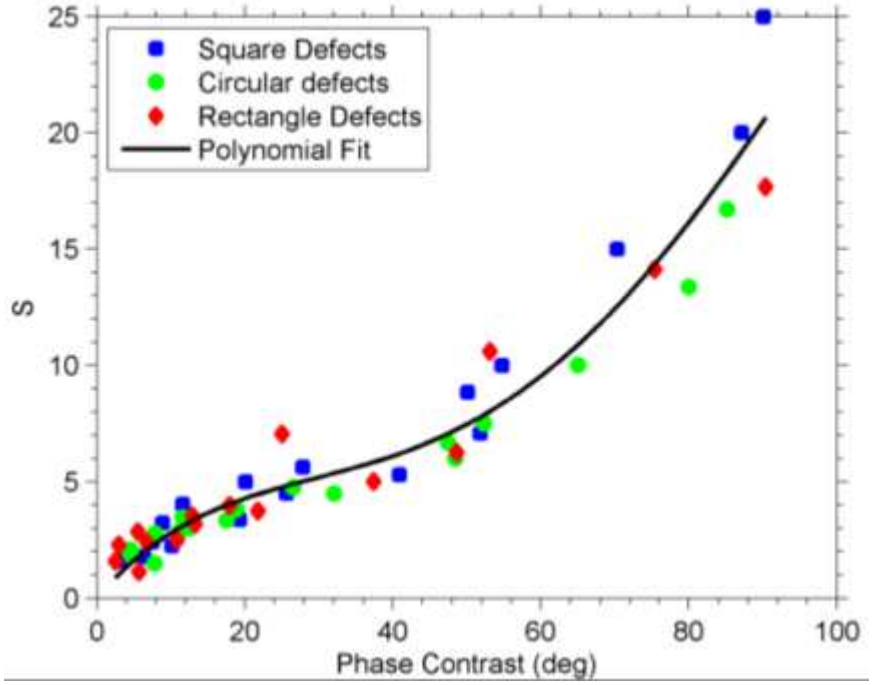

Figure 4.16: Plot of S vs phase contrast for defects of various shape, size and depths

4.4 Defect Sizing

Literature review clearly reveals that defect sizing in LT has not been reported. A shearing phase technique was employed for measuring the defect size and location of defect accurately [120, 121]. In this section FWHM method is considered for defect sizing and the effect of frequency on defect sizing is studied. To measure the defect size, a line profile is drawn over the defective area. The resulting phase distribution is a Gaussian as shown in fig. 4.17 (f = 0.05 Hz) and the FWHM is considered as a measure of defect size. Defects of size 10 mm x10 mm at various depths were considered for analysis. From fig. 4.17 it is observed that the trend in magnitude phase angle (line profile) is observed. It increases from left to right. To normalize, line profile was drawn over adjacent non defective region (fig. 4.18 (a)) and it was subtracted from line profile obtained on defective region as shown in fig. 4.18 (b). This phase contrast line profile is considered for analysis. At different frequencies the above procedure was carried out and the FWHM of phase contrast profile was computed. The variation of defect size as a function of frequency is shown in fig. 4.19 (a) and the associated error (% error) is shown in fig. 4.19 (b). From the fig. 4.19 (a) it can be observed that the measured defect size increases as frequency increases. At intermediate frequencies the measured defect size is comparable with the actual defect size and at frequency f = 0.05 Hz, the error associated with the defect size measurement is minimum (fig. 4.19 (b)). The minimum error at this frequency could be explained using thermal diffusion length. At frequency f = 0.07 Hz the thermal diffusion length is 4.2 mm which is comparable to sample thickness 3.6 mm. Another observation from fig. 4.19 (a) is that for near surface defects, the error in the sizing measurement is large when compared to deeper defects. This is because the reflection of thermal waves from the near surface defect is stronger causing more diffusion of thermal

waves around the defect. Hence near surface defects appear more diffused than the deeper defects causing broadened FWHM.

Table 4.3 gives the measured values of defect size at frequency 0.07 Hz and the errors associated with it. From the table one can observe that the maximum error associated is 2.5 % which is within acceptable limit.

Defect Depth (mm)	Actual Defect Size (mm)	Measured Defect Size (mm)	% Error
0.4	10	10.25	2.5
1.13	10	9.84	1.6
1.78	10	9.84	1.6

Table 4.3: Defect sizing using LT

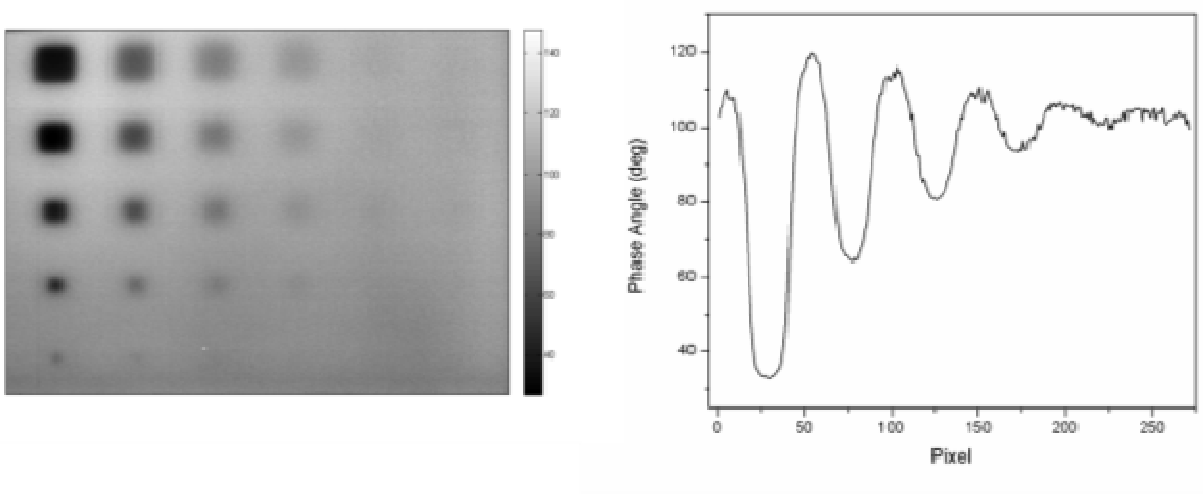

Figure 4.17: Phase image at 0.07 Hz and line profile over defects of size 10 mm

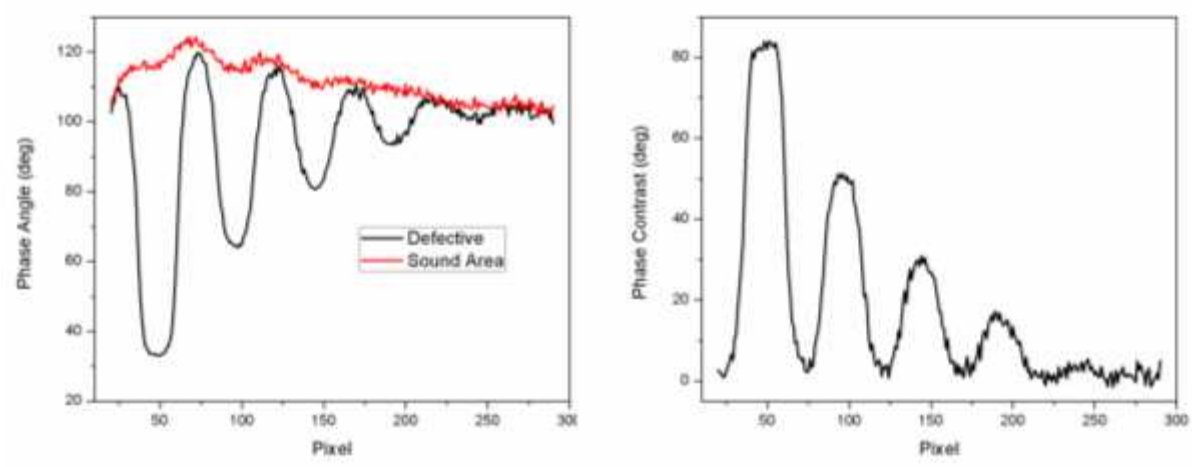

(a) (b)

Figure 4.18: (a) Line profiles over defective and sound area (b) Phase contrast profile

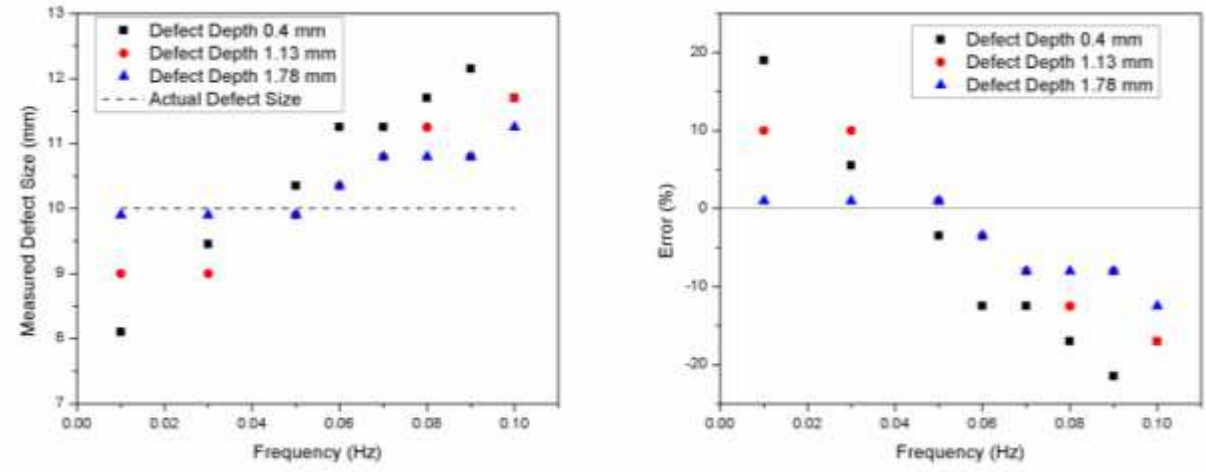

(a) (b)

Figure 4.19: (a) Defect size variation as a function of frequency for defects of various sizes (b) Percentage error associated with measurement

The present study showed the ability of LT for defect depth quantification and sizing. Two methods were discussed for depth quantification using LT, namely blind frequency method and phase contrast method. The experiments showed that blind frequency strongly depends on defect size and shape. Hence blind frequency cannot be considered as an accurate method for depth quantification unless a normalization parameter is used. In phase contrast method, the calibration plot was generated by plotting

phase contrast as a function of defect depth and the depth prediction was accurate. The study of effect of defect size and shape on phase contrast showed that the phase contrast is also a function of defect size and shape. A normalized parameter was defined called square root of defect area to defect depth ratio (S) which is independent of defect size and shape. The experiment was conducted for defects of different shape and size and calibration plot was generated. Defect sizing using LT was carried out. It was observed that defect size varies as function of frequency. At frequency 0.05 Hz, the error associated was minimum. Using LT, both defect depth and size could be measured with good accuracy.

CHAPTER 5

DEFECT CHARACTERIZATION USING PT AND LT – A COMPARATIVE STUDY AND CASE STUDIES

5.1 Introduction

The first part of this chapter deals with comparative study of defect detection, depth quantification and sizing using Lock in Thermography (LT) and Pulsed Thermography (PT). Visualization of defects of various size and depth in each technique is evaluated and for determination of the image obtained in each technique Signal to Noise Ratio (SNR) is calculated. In the second part, two important case studies are discussed. First case study discussed is on inspection of the brazing quality of Plasma Facing Components (PFC) which are used in fusion reactors and second study reported is on debond assessment in Nickel Boron (Ni-B) – SS coating system which are widely used due to their excellent wear and corrosion resistance and hardness. Both pulsed and lock in thermography techniques are used for the study and the results are compared. Validation of the brazing quality study is done with hot and cold simulation testing. For the validation of results in coating system, immersion ultrasonic testing is carried out.

5.2 Comparative Study

For comparative study between RT and LT, defect detectability, defect depth prediction and defect sizing aspects and the errors associated with them were considered.

5.2.1 Defect Detectability

Detection of smallest defect with adequate contrast by an observer is given as defect detectability. For defect detectability, thermal images at different time intervals

acquired during PT and phase image at 0.07 Hz (optimum frequency) in LT were compared as shown in fig. 5.1.

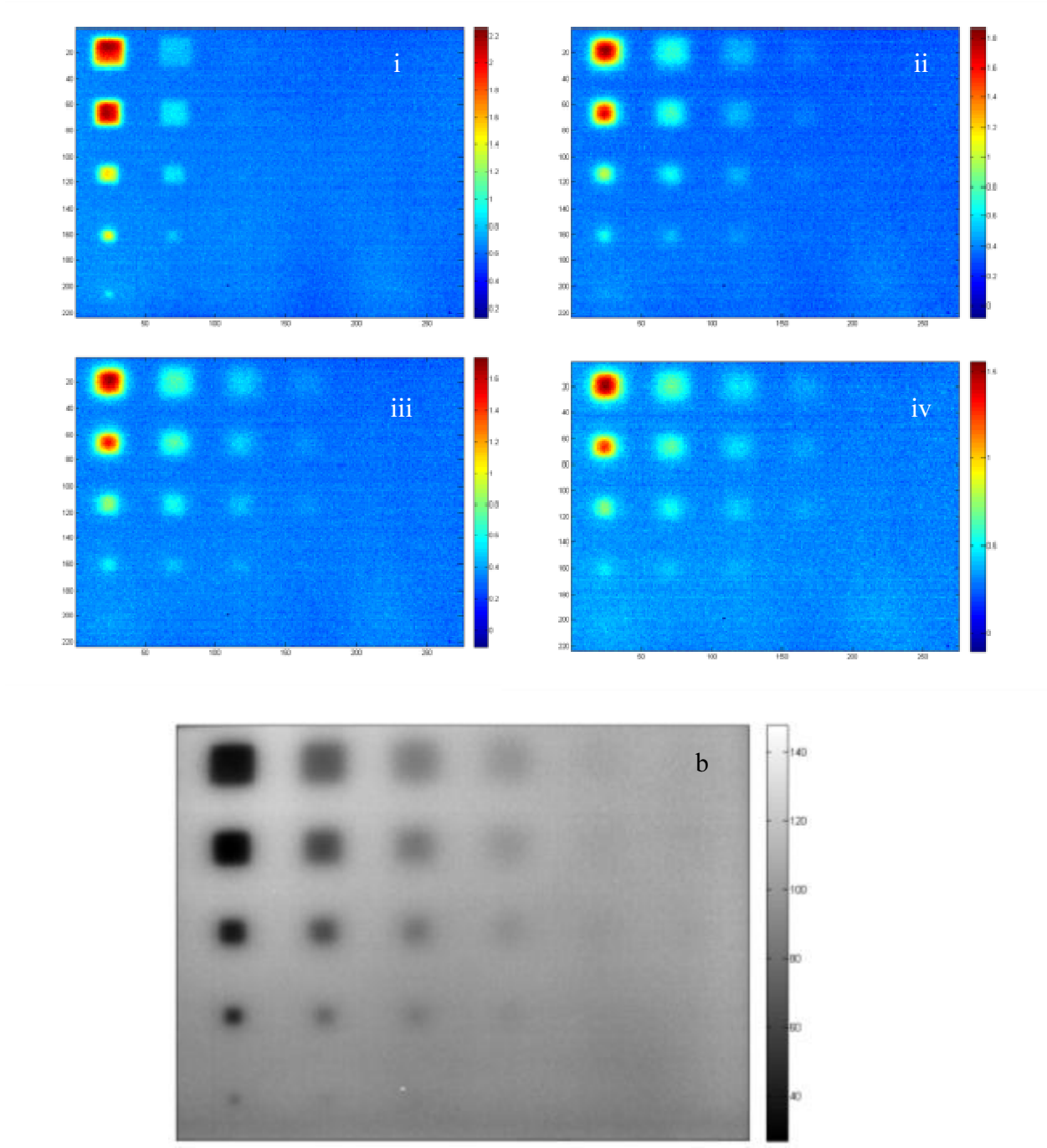

Figure 5.1: (a) Thermal images at time intervals (i) 0.2 s (ii) 0.75 s (iii) 0.95 s and (iv) 1.18 s in PT (b) Phase image at f = 0.07 Hz

Figure 5.1 (a) reveals that smaller defects appeared in the image for short time period and as time increased, they disappeared quickly due to diffusion of thermal waves around defect, when compared to defects of bigger size. The smallest defect observed is of size 2 mm x 2 mm at a depth of 0.4 mm and at depth 1.13 mm the defect is barely visible and deeper defects of size 2 mm x 2 mm were not detected. The defect of size 10 mm x 10 mm, 8 mm x 8 mm and 6 mm x 6 mm was clearly detected up to depth 2.48 mm. From the phase image (fig. 5.2 (b)) we can observe that defect of size 2 mm x 2 mm is barely visible at a depth of 1.13 mm. Defect of size 10 mm x10 mm at depth 2.48 mm is clearly visible whereas at depth 3.17 mm it is barely visible. The schematic diagram of the defect detectability using PT and LT is shown in fig. 5.2. From the figure it is clearly observed that LT gives more depth information than PT.

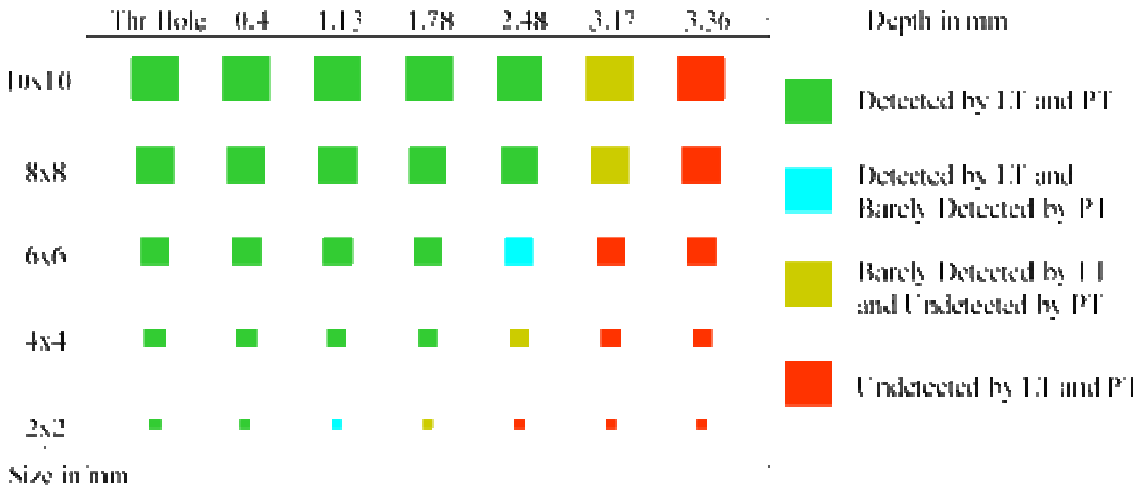

Figure 5.2: Comparison of defect detectability in PT and LT (schematic)

5.2.2 SNR Analysis: SNR is a measure of signal strength relative to background noise. It is expressed as the ratio of the mean of signal to standard deviation of the signal.

$$SNR = Avg / SD \qquad (5.1)$$

For an image, to compute the SNR, one requires signal and background. The mean of difference of signal (defective area) and background (sound area) gives the Avg while the standard deviation in the background (sound area) area gives the SD, which is nothing but the noise. Hence for an image SNR is given by [78, 167],

$$SNR = \frac{\bar{S}_D - \bar{S}_{SA}}{SD_{ND}} \qquad (5.2)$$

In case of PT, S stands for temperature value and in case of LT, S stands for phase value. Defects of size 10 mm x 10 mm at various depths were considered for analysis.

In PT, the SNR was computed over a period of time as shown in fig. 5.3 (a). From the figure, it can be observed that the SNR increases at the initial time where thermal waves start reaching the surface and then decreases due to the lateral diffusion of thermal waves. In LT, the SNR was computed as a function of frequency for defects of various depths and is shown in fig. 5.3 (b). From the figure, it can be observed that the SNR is maximum near the frequency 0.05 Hz which is near to the optimum frequency (0.07 Hz). Figure 5.3 clearly shows that near surface defect has higher SNR when compared to deeper defects because of higher strength of thermal waves for near surface defect. It is also observed that LT has superior SNR than PT. To study the variation of SNR as a function of defect size, defects of size 10 mm x 10 mm and 6 mm x 6 mm at depth 0.4 mm. The SNR as a function of time in PT and as a function of frequency in LT are computed and shown in fig. 5.4. From fig. 5.4 it is observed that SNR decreases with defect size due to the lateral diffusion of thermal waves around the defect in case of PT. In LT, the SNR is comparable in both the cases. The comparison of SNR in case of PT and LT are given in table 5.1, for defects of size 10 mm x 10 mm and 6 mm x 6 mm at various depths. In PT, peak SNR is considered for analysis. From the table it can be observed that the SNR is superior for LT

than PT. It is well established that in LT particularly Phase angle has an advantage of being less sensitive to local variations of illumination and surface emissivity compared to PT. Hence LT shows higher SNR compared to the PT.

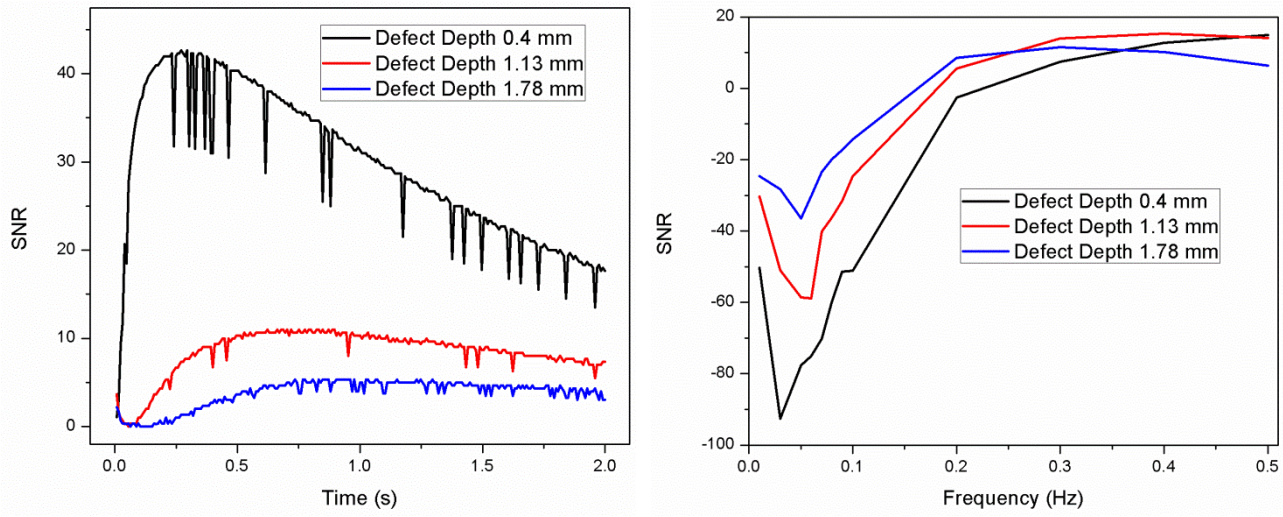

(a) (b)

Figure 5.3: (a) SNR variation as a function of time in PT (b) SNR variation as a function of frequency in LT

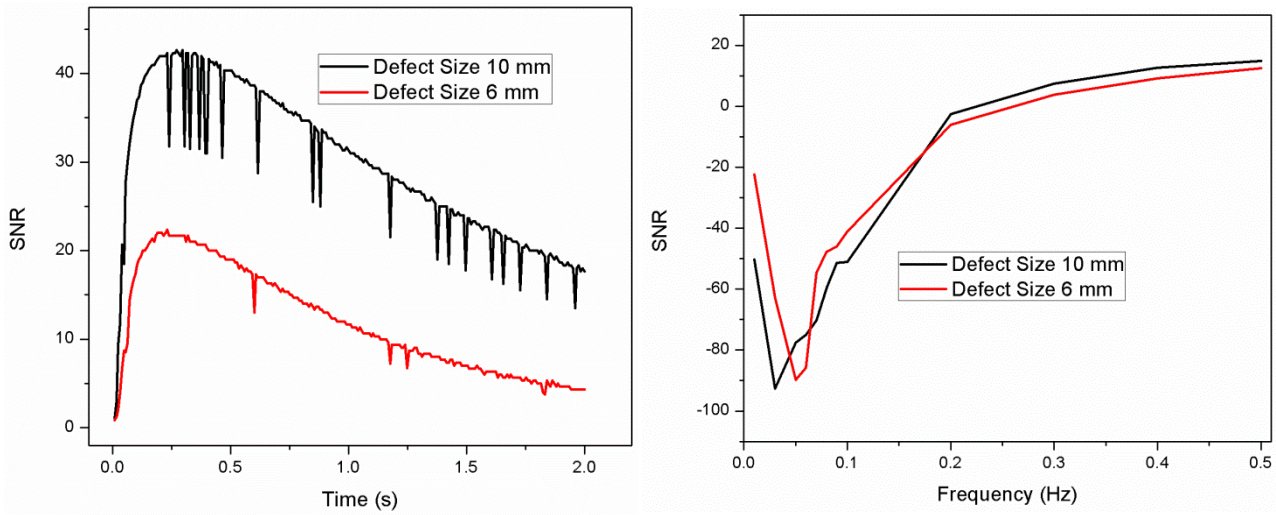

(a) (b)

Figure 5.4: SNR variation for defects of size 10 mm and 6 mm in case of (a) PT (b) LT

Defect Size (mm)	Defect Depth (mm)	SNR PT	SNR LT
10	0.4	42.67	92.55
	1.13	11	58.91
	1.78	5.33	36.39
6	0.4	22.33	89.76
	1.13	8.67	49.10
	1.78	3.67	22.45

Table 5.1: SNR comparison between PT and LT for defects of different size and depth

Effect of Smoothing in PT: In PT, smoothing is carried out in two steps. First, the raw thermal images are background subtracted, second, thermal signal reconstruction (TSR) was carried out on background subtracted images to further reduce noise. It is well known that during smoothing process we lose some data from original signal. This two stage smoothing will affect the SNR in PT. This is illustrated in fig. 5.5, which is SNR plot for defect of size 10 mm x 10 mm and depth 1.13 mm calculated with raw signal, background subtracted signal and TSR signal. From the plot it is observed that SNR is higher for raw data while it decreases for background subtracted data and less for TSR data.

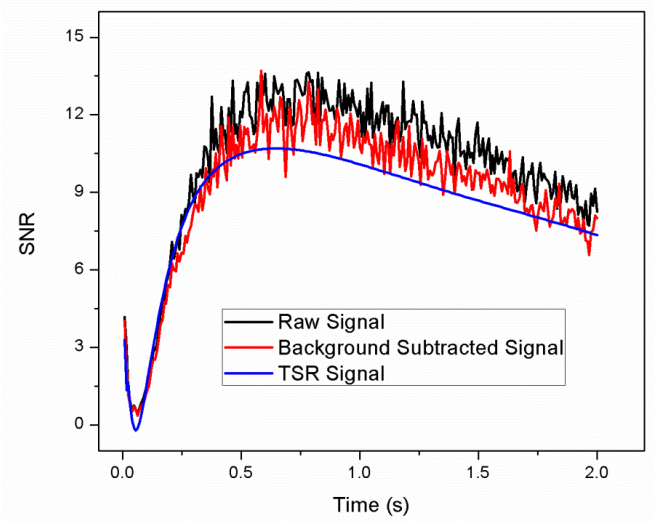

Figure 5.5: Comparison of SNR in PT computed using raw, background subtracted and TSR signals

Enhancement of defect visualization in PT using second derivative image: It was observed that in PT, the defects detected is less when compared to LT. To improve defect detectability in PT, the second derivative image is considered [73]. In thermal images the later diffusion of heat is predominant. The defect is better visualized when the temperature contrast of defect is maximum. But, at his stage lateral diffusion of thermal waves becomes predominant which results in masking of deeper defects and shallower defects of smaller size. Using TSR, one can obtain the derivative of temperature history in logarithmic domain. The second derivative image gives the indication of presence of defect much earlier than the contrast image (refer fig. 3.12). Thus it reduces blurring of the defects caused by diffusion of thermal waves and allows the visualization of deeper and smaller defects. This is illustrated in fig. 5.6, which is second derivative image sequences at different time intervals. From the figure, it can be observed that the defect of size 6 mm x 6 mm at depth 2.48 mm and 2 mm x 2 mm size defect at depth 1.13 mm can be clearly seen which were barely visible in temperature image (refer fig. 5.1 (a)). The deeper defect of size 10 mm x 10 mm at depth 3.17 mm is barely visible in second derivative image which was missing in temperature image. The schematic diagram comparing the defect detectability of thermal image and second derivative image is shown in fig. 5.7. From the figure we can observe that the second derivative image gives more depth information than the thermal image.

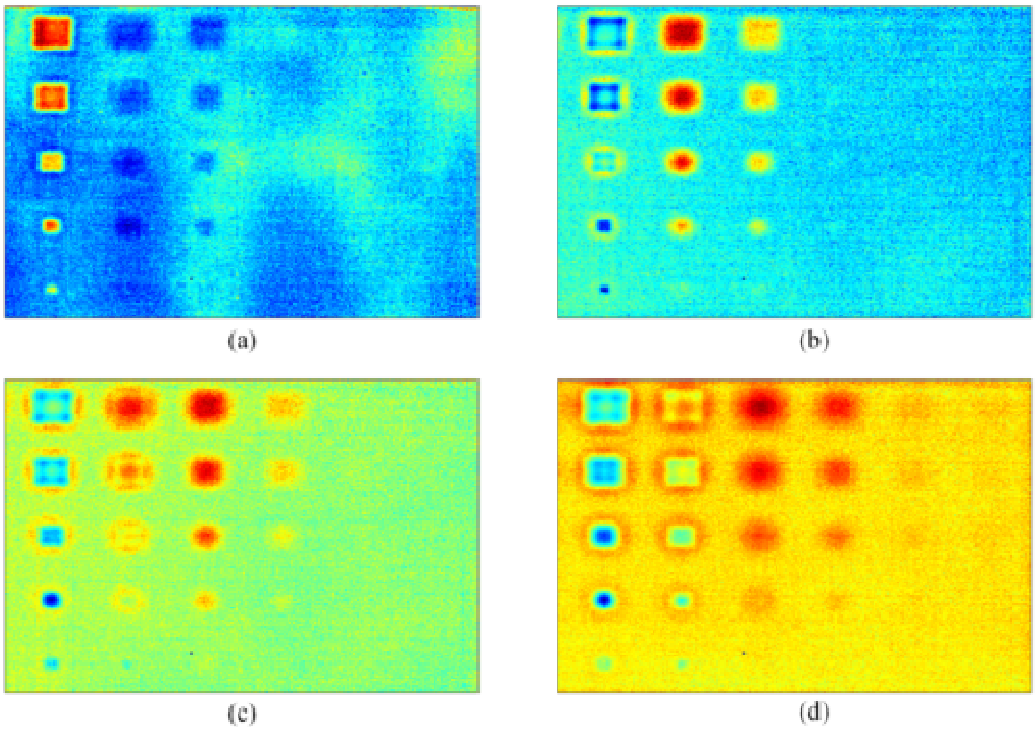

Figure 5.6: Second derivative images at time intervals (a) 0.02 s (b) 0.1 s (c) 0.2 s (d) 0.3s

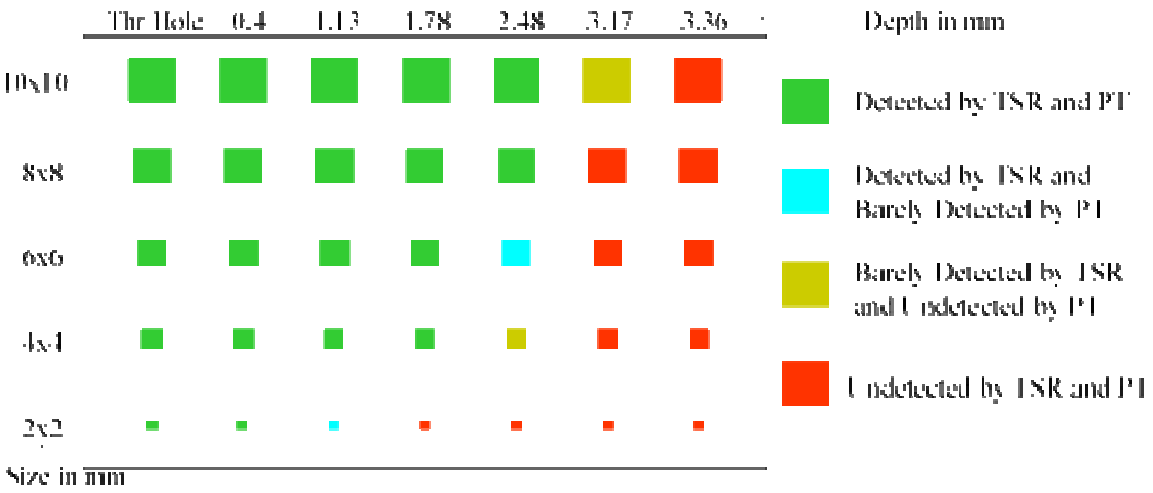

Figure 5.7: Comparison of defect detectability in PT and TSR (schematic)

5.2.3 Depth Prediction and Sizing Comparison: In chapter 3, various depth quantification methods in PT were discussed and it was observed that log second derivative method gives good accuracy and is independent of defect size and shape. In LT, phase contrast method was observed to be better method for depth quantification. Hence

these two methods were considered for depth prediction comparison. Defects of size 10 mm x 10 mm at various depths were considered for analysis. Table 5.2 gives comparison of defect depth prediction and error associated with it in both the techniques. From the table it can be observed that in case of LT the error associated with depth prediction is less when compared to PT. Similarly the sizing measurement comparison is done. Defect of size 10 mm x 10 mm at various depths were considered for analysis. The comparison is given in table 5.3. From the table, it is observed that both PT and LT give accurate size measurement.

Actual Depth (mm)	**Measured Depth (mm)**			
	PT	% Error	LT	% Error
0.5	0.44	12	0.45	10
1.15	1.06	7.8	1.23	6.9
1.83	1.92	5	1.99	8.7

Table 5.2: Defect depth prediction comparison in PT and LT

Actual Size (mm)	**Measured Size (mm)**			
	PT	% Error	LT	% Error
9.99	9.51	4.8	10.35	3.6
9.94	10.02	0.8	9.9	0.4
9.9	9.99	1	9.9	0

Table 5.3: Defect size measurement comparison in PT and LT

5.3 Case Studies

In this section two case studies are discussed. First, brazing quality inspection of Plasma Facing Components (PFC) which are used in fusion reactors, second, debond inspection of Ni-B coating on AISI 316 L SS. Both PT and LT techniques were used and results were compared. The results were also validated with other NDT techniques.

5.3.1 Brazing Quality Inspection of Plasma Facing Components

Nuclear fusion reaction produces enormous amount of energy (Example: Fusion of tritium and deuterium gives helium with neutron of energy 14.1 MeV). By harvesting the fusion energy in controlled manner, one can use it for power production. Research and development projects have been carried out worldwide to develop the international thermonuclear experimental reactor to maintain continuity with Tokamak type reactors and to develop fusion plasma technology [168, 169]. Tokamak is a facility used to confine plasma in the shape of tours using magnetic field. The temperature of the plasma in the fusion reactor is very high of the order of few million Kelvin. Hence the first wall, the limiters and the diverters used in the magnetic confinements are made of high temperature materials. The role of the diverter is to reduce the amount of plasma flowing directly into the first wall as a result of plasma disruption. Fusion reaction is maintained by controlling magnetic fields around the diverter in such a way that the impurities in the plasma and those generated during the control procedure are removed through the diverter [170, 171]. To protect diverter, first wall of the reactor, lining materials are used which are called PFC. The PFC consists of plasma facing material (PFM) and heat sink. The PFM and the heat sink are joined together by brazing or welding [172]. Brazing is the most commonly used technique. The most commonly used PFM are carbon (graphite), tungsten, molybdenum [172 – 174] and the heat sinks are copper and CuCrZr alloy while the brazing material are CuCrZr and CuCr alloys [175]. The performance of the fusion reactor

greatly depends on the heat removal capability of the PFC. If the connection of PFM to heat sink is not satisfactory then their service life is shortened significantly. Hence the brazing quality in PFC has to be checked before using in the reactor and during their service. In the present study thermal imaging techniques are used for the study. This work was in collaboration with Institute of Plasma Research, Gandhinagar, India.

Sample Details: Sample was received from IPR with graphite as PFM and copper as heat sink. CuCrZr was used as brazing material. The sample was a matrix of 3 x 5 tiles. The schematic diagram of the sample is shown in fig. 5.8 (a) and fig. 5.8 (b) is the photograph of the sample. Graphite tiles of dimension 10mm (L) x 10mm (W) brazed to copper block of dimension 31 mm x 31mm x 52mm with longitudinal cylindrical hole (inner diameter = 10 mm) through the copper block. The height of the Graphite tiles is 10 mm. The thermo physical properties of PFMs, heat sink and the brazing materials are given in table 5.4. Tiles were numbered from 1 – 15 from left to right as shown in fig. 5.8 (a).

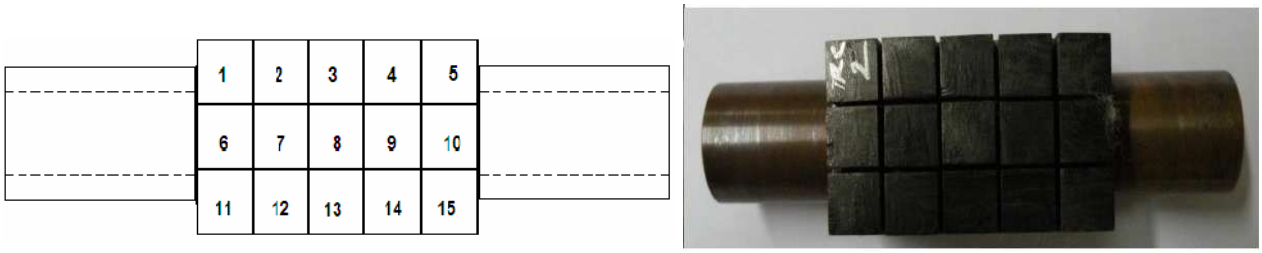

(a) (b)

Figure 5.8: (a) Schematic diagram of the sample with 15 numbers of tiles (b) Photograph of the sample

	Graphite	CuCrZr	Copper
Density (kg/m^3)	1820	8800	8950
Thermal Conductivity (W/m-K)	95	320	400
Specific Heat (J/kg-K)	650	350	386
Thermal Diffusivity (m^2/s)	80.3x10^{-6}	103.9x10^{-6}	115.8x10^{-6}
Thermal Effusivity (J/m^{2}Ks$^{0.5}$)	10601.2	31394.3	37173.6
R (Graphite – CuCrZr)	-0.49		
R (CuCRZr – Copper)		-0.08	
R (Graphite – Copper)		-0.56	

Table 5.4: Thermo physical properties of graphite, brazing material and copper and the reflection coefficient

Pulsed Thermography: PT was carried out in reflection mode using 2 Xe flash lamps of power 1600 W each. Thermal image sequences were recorded using frame rate of 138 Hz for time interval of 3 seconds (Refer Chapter 2.4.2.1 for experimental set up). Then TSR was carried out with polynomial of order 6. Reconstructed images were considered for analysis. From table 5.4 it is observed that graphite has negative reflection coefficient (R) with both copper and brazing material. Thermal image sequences at time 0.1 s, 1 s and 2 s are shown in fig. 5.9.

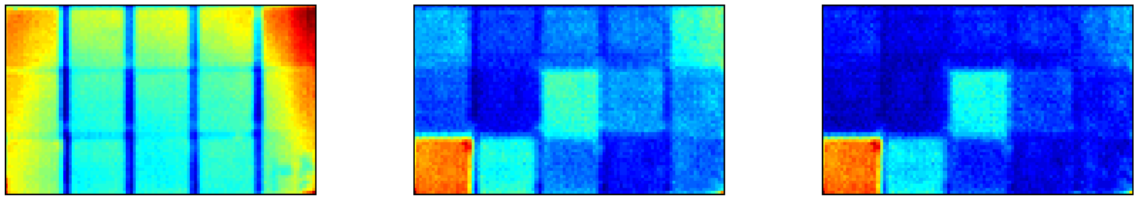

(a) (b) (c)

Figure 5.9: PT image sequences at time intervals (a) 0.1 s (b) 1 s (c) 2 s

From the figure it is observed that three tiles, tile no. 8, 11 and 12, showed higher temperature while tile no. 5 showed initial rise in temperature and attained equilibrium as time increased. This gives the indication that tile no. 5 has not been brazed well. Then temperature history was plotted in logarithmic domain to see the deviation in temperature history of defected tiles. Figure 5.10 shows the temperature history of all the tiles in logarithmic domain. From the figure we can observe that tile no. 8, 11 and 12 deviates from the normal temperature decay plot indicating the poor quality of brazing. The temperature decay of tile no. 5 follows that of well brazed tiles and no deviation is observed. The amplitude of temperature is slightly high when compared to other tiles. This might be due to reasons like non uniform heating, surface irregularities or lower thickness of tile or brazing material. Figure 5.11 (a) shows the temperature decay of well brazed tile (tile no. 7) and defective tile (tile no. 11) in logarithmic domain. From the figure we can observe that the tiles no. 7 follows a linear trend at initial stage and then it starts to decrease when thermal waves reach the brazing material due to negative R. In case of tile no. 11, the temperature history follows a linear trend at initial stage, similar to tile no. 7. Then the temperature increases due to the air gap present between the tile and the brazing material (+R). To see the change in slope of decay curve, first derivative of temperature decay in logarithmic domain and plotted as a function of log time and is shown in fig. 5.11 (b). The figure shows that the tile no. 7 has the negative peak and tile no. 11 has the positive peak and both starts to deviate at the same time, since the thickness of tile is same. Hence log first derivative plot can be used for differentiating the defective tiles from well brazed tiles.

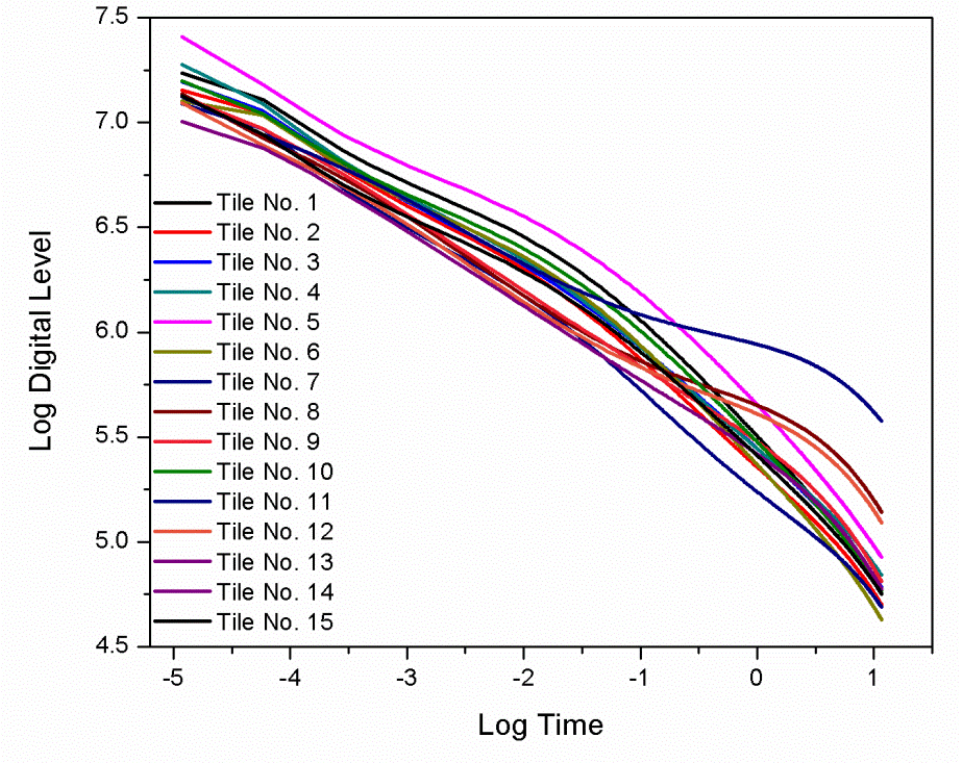

Figure 5.10: Temperature decay of all the tiles in logarithmic domain

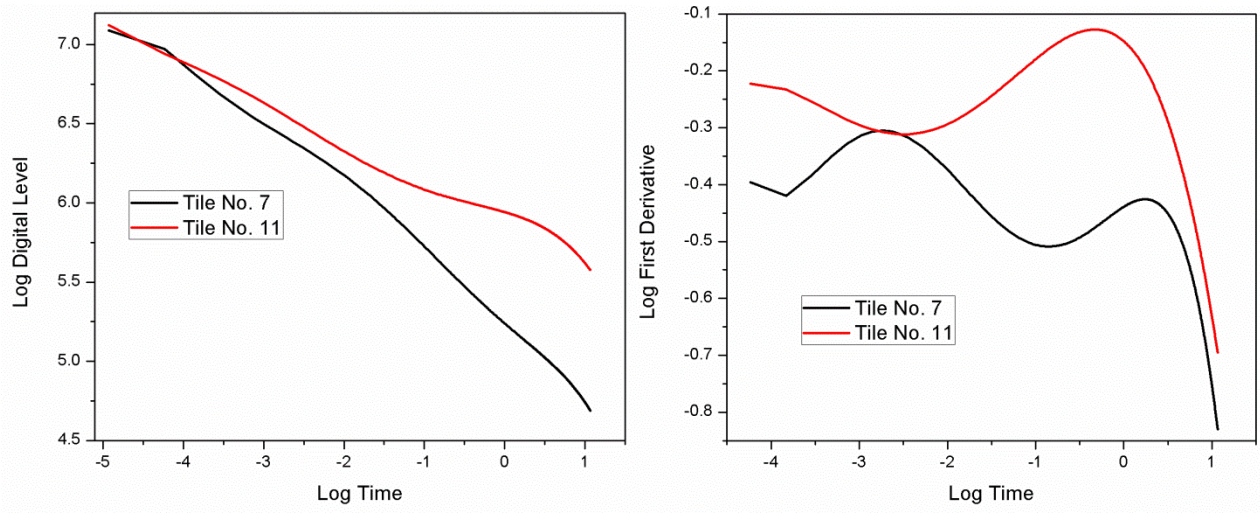

(a) (b)

Figure 5.11: (a) Comparison of temperature decay in logarithmic domain of tiles no. 7 and 11 (b) Corresponding first derivative plot

The earlier study showed that second derivative image gives better defect visualization. Hence second derivative images were computed at time intervals 0.1 s, 1 s and 2 s and are shown in fig. 5.12. The figure clearly shows 5 tiles are defective. Tile no. 5 is shown as

non defective tile in second derivative image. Hence PT can be used for brazing quality inspection with the aid of signal processing techniques.

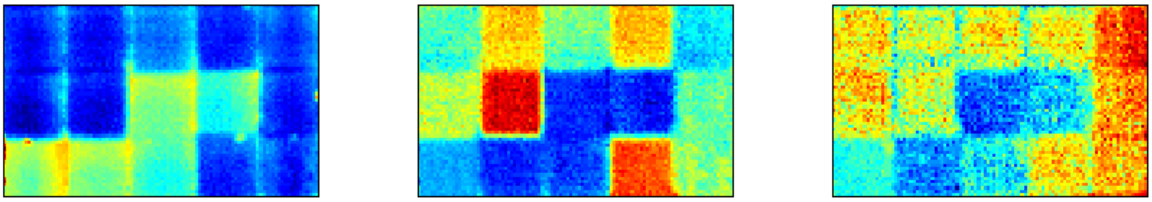

(a) (b) (c)

Figure 5.12: (a) Second derivative images at time intervals (a) 0.1 s (b) 1 s (c) 2 s

Lock in Thermography: LT was carried out at frequency range 0.005 Hz to 0.2 Hz with two halogen lamps of power 1000 W. The choice of lower frequency is due to the higher thickness of tiles (10 mm). Frame rate used was 50 Hz. (Refer Chapter 2.4.2.2 for experimental set up)

Phase and amplitude images at frequencies 0.01 Hz, 0.07 Hz and 0.1 Hz are shown in fig. 5.13. from the figure it is observed that tile no. 8, 11 and 12 are clearly seen in phase and amplitude images at all frequencies indicating they are defective tiles.

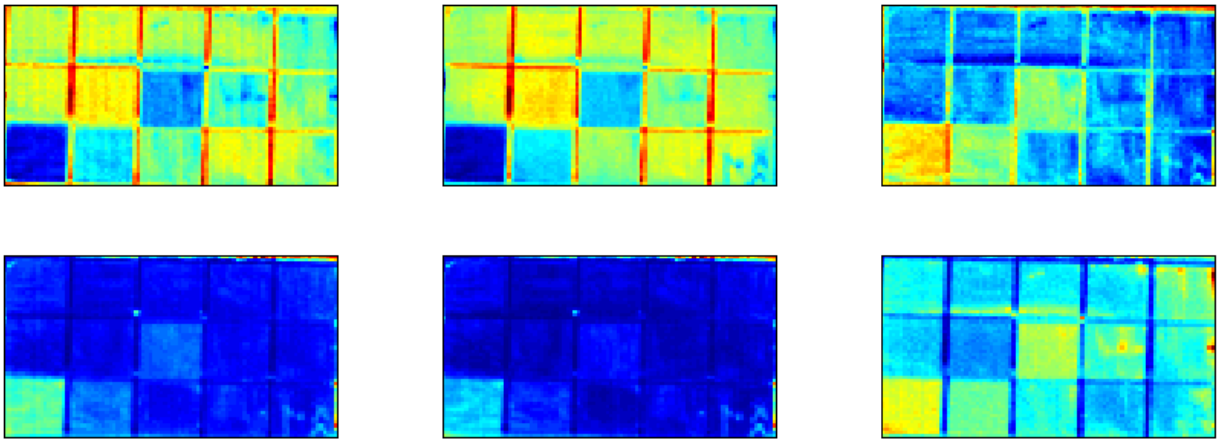

Figure 5.13: Phase images at frequencies (a) 0.01 Hz (b) 0.07 Hz (c) 0.1 Hz Amplitude images at frequencies (d) 0.01 Hz (e) 0.07 Hz (f) 0.1 Hz

Tile no. 7 was considered as reference tile and the phase angle was subtracted from other tiles to get the phase contrast values as shown in fig. 5.14. The figure shows that the fluctuation in phase angle measurement even for non defective tiles, though the tile no. 8, 11 and 12 have higher phase contrast indicating clearly as defective tiles. To differentiate between defective and well brazed tiles, one has to define threshold value of phase contrast. To define this threshold value, the phase contrast values of all the tiles were averaged and this was set as threshold. In the present study the threshold value is -5 degree (fig. 5.14). From the fig. 5.14 it can be observed that tile no. 8, 9, 11 and 12 are defective due to the poor brazing quality.

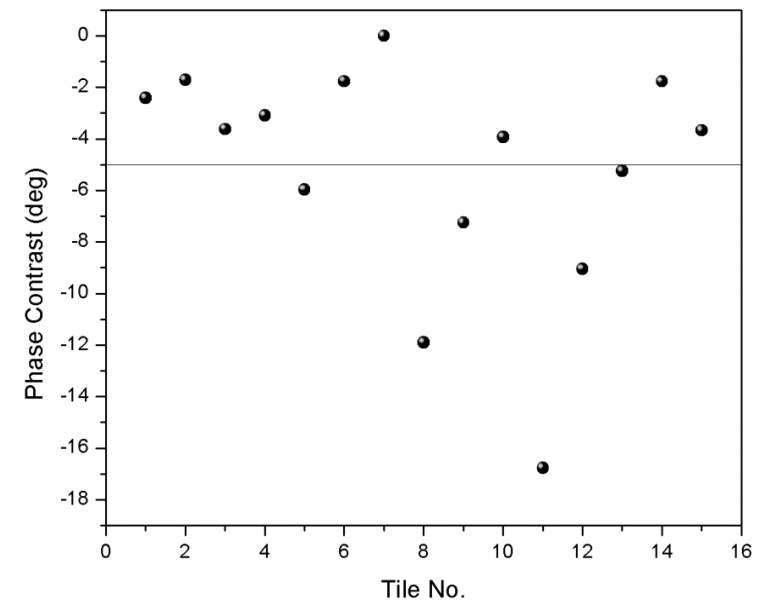

Figure 5.14: Phase contrast computed for different tiles with tile no. 7 as reference. The horizontal line at -5 deg is the threshold line

Validation: For validating the above results, Hot and Cold simulation was carried out, which is a standard method used for brazing quality inspection in PFC. It is done in transmission mode. Hot water was passed through the copper sink and the temperature rise was recorded using an IR camera. Five tiles (tile no. 8, 9, 11, 12 and 13) recorded lower

rise in temperature indicating poor brazing of tiles to heat sink. Tile no. 8 and 11 had lower temperature indicating poor brazing where as tile no. 9, 12 and 13 recorded intermediate temperature rise indicating moderate brazing of tiles. The results are in correlation with PT and LT results. The thermal image is shown in fig. 5.15.

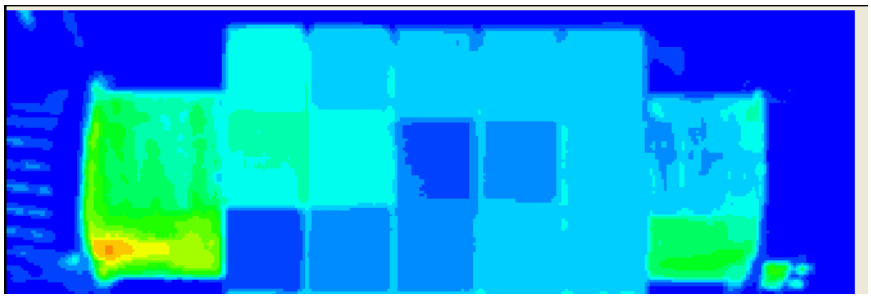

Figure 5.15: Thermal image of hot and cold simulation carried out at IPR, Gandhinagar

5.3.2 Debond detection using PT and LT

In industries coatings have become important part of system. Coatings protect the structural materials from hazardous and corrosive environment by improving its surface properties. The coating thickness varies from few microns to few millimeters depending on the application. Electroless deposition is an emerging coating technique where single electrode is used, no electrical energy is supplied and the electrolyte consists of reducing agent [176, 177] and they are widely used for developing Nickel Phosphorus and Nickel Boron (Ni-B) coatings. Ni-B coatings are one of the most widely used coatings in aerospace, nuclear, chemical industries due its good corrosion, wear resistance and excellent hardness [178 - 182]. The inspection of coatings for coating thickness evaluation, thickness variation and debond detection is important before using them in field since if the coating thickness is not up to the desired level or if the coating to substrate adhesion is not good, it will lead to the failure of the system. Debond is the most common type of defect in coatings. Debond is the lack of chemical bonding between

coating and substrate leading to separation of coating from substrate. For the present study, the coatings were developed by CECRI, Karaikudi in collaboration with QAD and CSTG, IGCAR. The case study focuses on the inspection of Ni-B coatings on AISI grade 316 L stainless steel substrate. As coated samples with coating thickness of 75 μm were inspected for debond detection using PT, LT. Then ultrasonic immersion test was carried out to confirm the debond in coating.

Electroless Ni-B Coating: Ni-B coating was deposited on AISI grade 316 L SS using electroless nickel deposition technique. The stainless steel substrates of dimension 100 mm x 150 mm x 3 mm were selected for deposition process. Initially the samples were cleaned by sandblasting, then by dipping in acid solution (HCl) for 2 minutes, then washed with tap water and then with DI water for 2 minutes. Water soluble nickel chloride salt was taken and sodium borohydrate was used as reducing agent. EDTA was used as stabilizing agent and the pH was maintained at 10-11. The temperature of the bath was kept at 80±2^{o}C. The deposition time was varied depending upon the thickness of the coating required. The photograph of the sample is shown in fig. 5.16.

Figure 5.16: Photograph of the sample

In Pulsed Thermography, 2 Xenon flash lamps of power 1600 W with pulse width around 2 ms were used. The experiment was conducted in reflection mode. The distance between object and lamp was 30 cm and the distance between object and camera was 35 cm. The temperature decay was recorded using thermal camera with frame rate of 125 Hz for 1 sec. High frame rate and less acquisition time was chosen due to high thermal diffusivity of the coating.

In lock in thermography, 2 halogen lamps with power 1000 W were used as exciting sources. A function generator with amplifier was used to control the frequency and the power of incident waves. ALTAIR LI software was used for lock in analysis. Object to lamp and object to camera distance was 40 and 35 cm respectively. The experiment was carried out for the frequency range of 0.01 to 1 Hz with frame rate 25 Hz. (Refer Chapter 2.4.2 for experimental set up)

Results and Discussion

Pulsed Thermography: Thermal images at different time intervals are shown in fig. 5.17. Figure 5.17 clearly shows that there are debond areas in the sample, which are at higher temperature than surrounding area. The high diffusive nature of the coating could be observed from fig. 5.17. The temperature differences produced by debond area decays very fast and attain equilibrium with surrounding area in short time period. The temperature difference observed in 0.016 s frame was completely decayed in 0.5 s frame. Hence the frame rate play an important role in PT, if low frame rate is chosen for high diffusive medium, there is a possibility of missing debond or defects in the thermal image. Figure 5.17 clearly reveals that debond areas are at higher temperature than surrounding areas. This is because there is an air gap between coating and the substrate at which the thermal wave interacts and reflects back on to the surface. Figure 5.17 reveals that there are some areas where temperature decay is in between that of sound area and debonded

area. Temperature response in log scale is plotted over different areas (area 1, 2 and 3) and is shown in fig. 5.18. Area 1 corresponds for sound area, area 2 and 3 corresponds for debonded area. Temperature response of area 3 is in between those of area 1 and area 2. From fig. 5.18 it is also observed that the temperature contrast lasts for long time in case of area 2 which is complete debonded area (1 sec), where as in case of area 3 temperature contrast decays in early stage (around 0.2 sec).

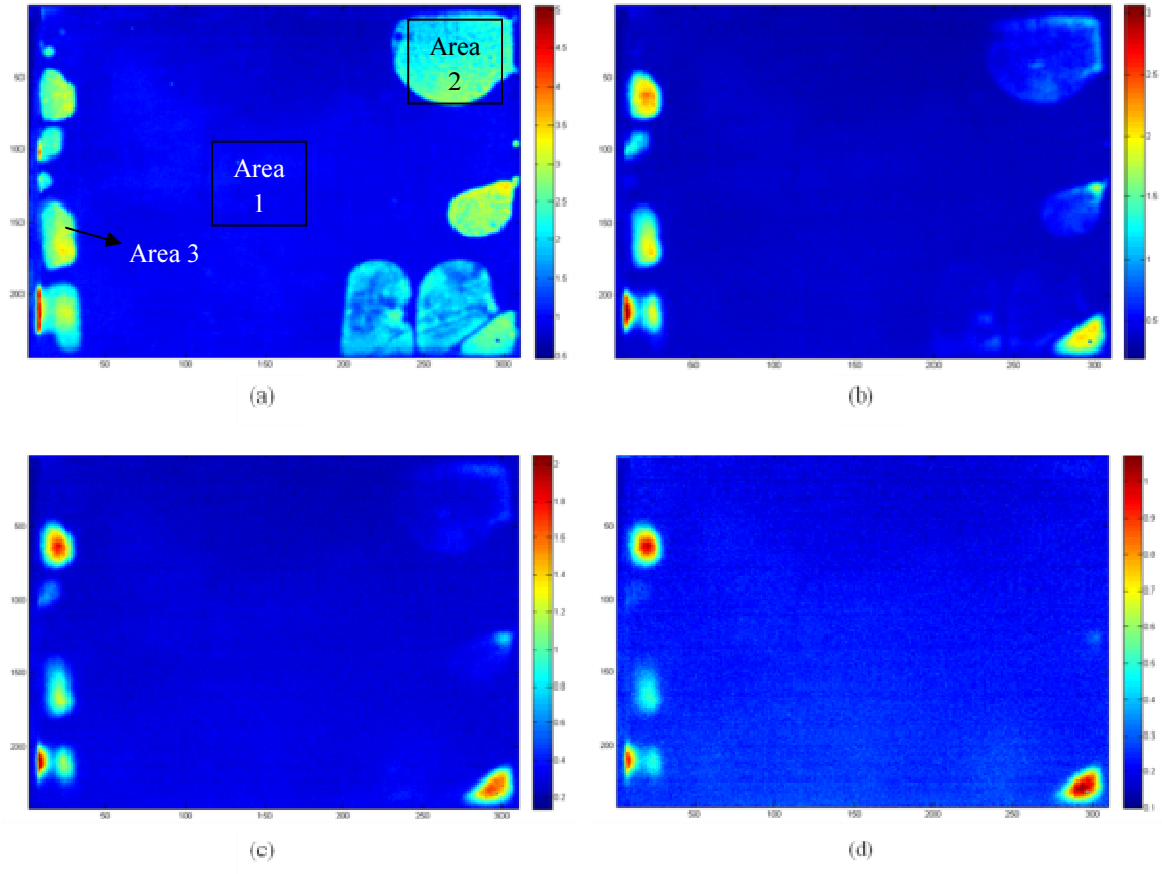

Figure 5.17: Thermal images at time intervals (a) 0.016 s (b) 0.12 s (c) 0.24 s (d) 0.48 s

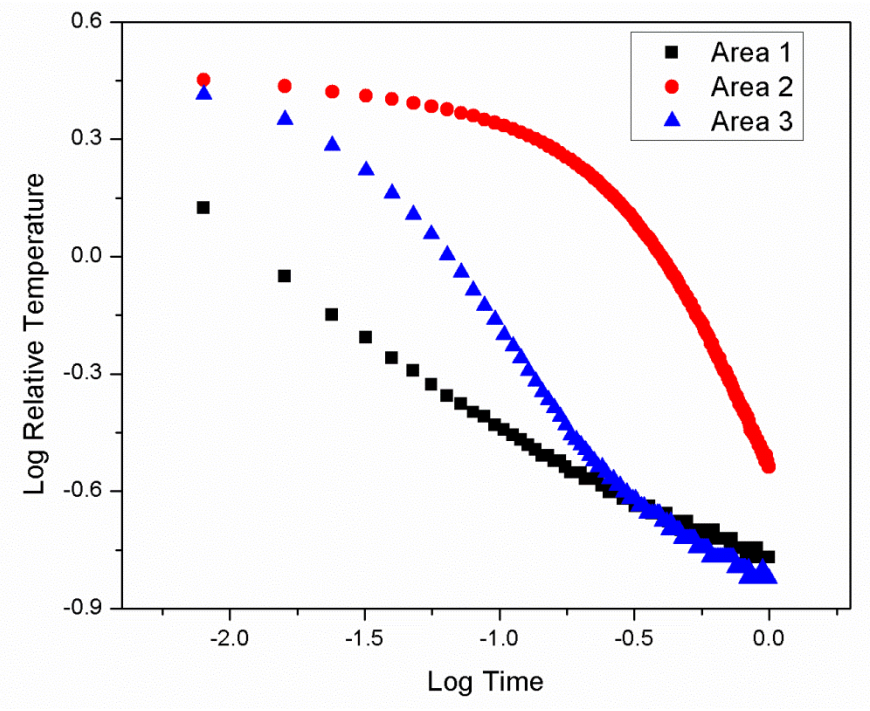

Figure 5.18: Temperature decay plot in logarithmic curve for areas 1, 2 and 3

Lock in Thermography: Lock in thermography was carried out in frequency range 0.01 to 1 Hz. Phase and amplitude images at frequencies 0.01, 0.1 and 0.7 Hz were shown in fig. 5.19. From the figure it is observed that phase image gives better information than amplitude image. Also at lower frequencies the complete information on debond was not observed but at higher frequencies (> 0.1 Hz) all debonds were clearly visible. This is true in case of amplitude images also. The phase angles over areas 1, 2 and 3 were measured and plotted as a function of frequency as shown in fig. 5.20 (a). From the figure it is observed that the phase angle variation of area 3 is in between that of area 1 and 2 (sound area and debonded area). The phase contrast was computed by taking the phase angle difference between the sound area and debonded area and plotted as a function of frequency as shown in fig. 5.20 (b). From the figure it was observed that phase contrast for area 2 increases as a function of frequency at initial stage then gradually decreases. The phase contrast reaches zero at particular frequency (blind frequency) and above this

frequency phase inversion occurs. Phase inversion can be clearly seen in fig. 5.19 at 0.7 Hz. But in case of area 3 no phase inversion was observed.

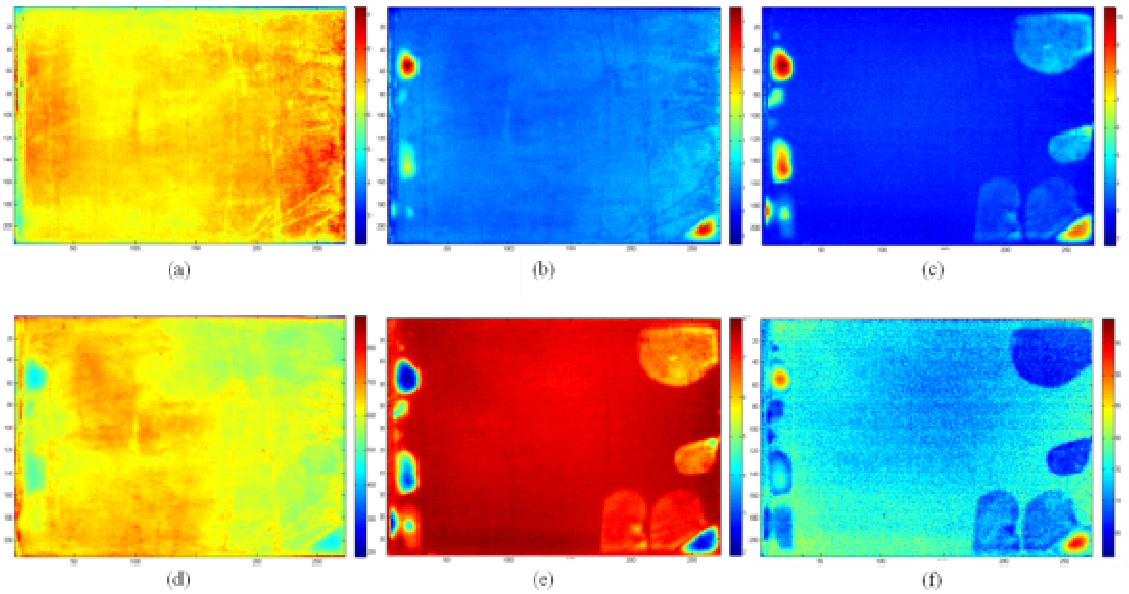

Figure 5.19: Phase images at frequencies (a) 0.01 Hz (b) 0.1 Hz (c) 0.7 Hz and Amplitude images at (d) 0.01 Hz (e) 0.1 Hz (f) 0.7 Hz

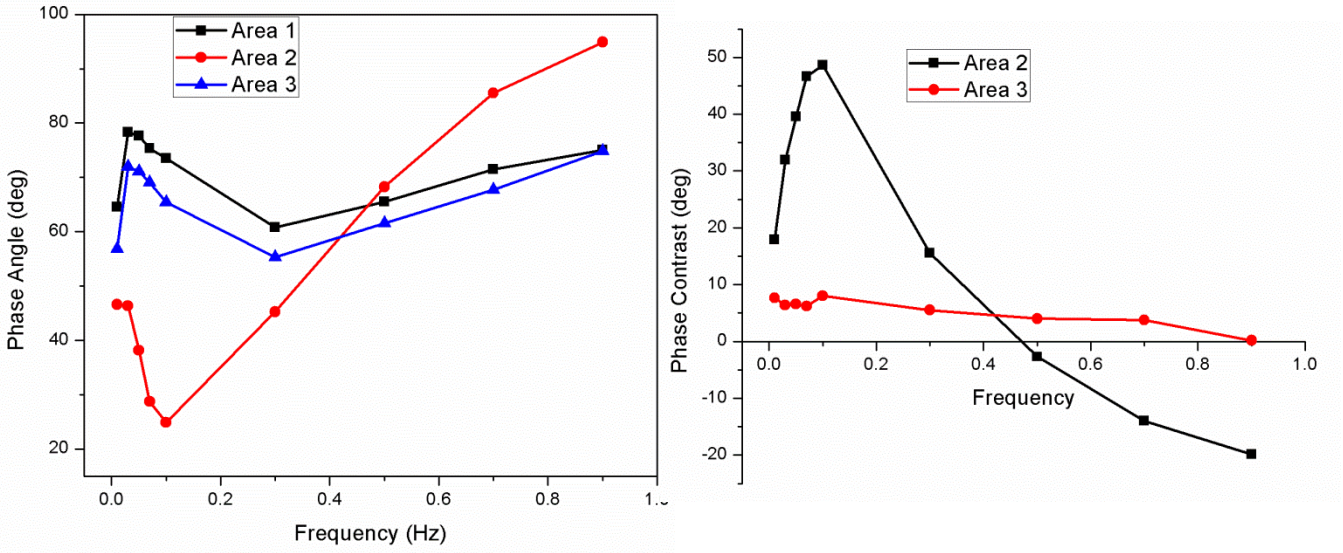

(a) (b)

Figure 5.20: (a) Phase angle variation as a function of frequency for area 1, 2 and 3 (b) Phase contrast variation as a function of frequency for area 2 and 3 (area 1 as reference)

Ultrasonic Immersion Scanning: Ultrasonic Testing (UT) is one of the conventional NDE techniques which is used widely in process, nuclear and other industries. UT can be carried out in reflection and transmission mode. In the present study the experiment was conducted in reflection mode. In reflection mode (pulse echo method) a high frequency sound wave (Ultrasound) is passed through the material using a piezoelectric crystal transmitter. The ultrasound wave propagates inside the material and some part of it is reflected from the rear side of the material and propagates back to surface which can be detected by a receiver and the signal is called back wall echo. When a defect is present, the ultrasonic waves are attenuated and reflect back to the surface. Hence an intermediate peak is observed between the initial pulse and back wall echo which indicates the presence of defect. Couplants are used between the transducer and the testing object surface for better transmission of ultrasonic waves. Advances in electronics, sensors and robotics helped in developing conventional UT to advanced UT techniques like phased array UT, guided wave UT and immersion UT techniques. In immersion UT the testing material is immersed in liquid which acts as couplant and the transducer is mounted on computer controlled mechanical handle which can scan in all 5 directions with good precision. In immersion UT, the spatial resolution given for recording the signal decides the resolution of the image. UT has been successfully used for debond detection in composites [183, 184] and also for kissing bond detection [185, 186].

Experimental Setup: Water was chosen as the medium for UT immersion scanning test. 5 axes scanner, developed by Trotix robots, was used for scanning the sample. A 200 MHz band width pulsar supplied by Panametric NDT was used to generate and control the ultrasonic waves. A 15 MHz transducer of focused type with 2 inch focal length and 9.5 mm diameter was used for the experiment. 150 mm x 100 mm roaster scanning was carried out with scanning resolution of 0.5 mm x 0.5 mm. The software used for the

analysis was acqUT from Dhvani research and development solution centre. The tank was filled with water. The water column height was adjusted in such a way that the second reflection from the front surface comes after the first back wall echo. Using this software we could analyze the A scan (Amplitude information), B scan (Cross-sectional information) and C scan (Area information or image) after the completion of scanning. The schematic diagram of the experimental set up is given in fig. 5.21.

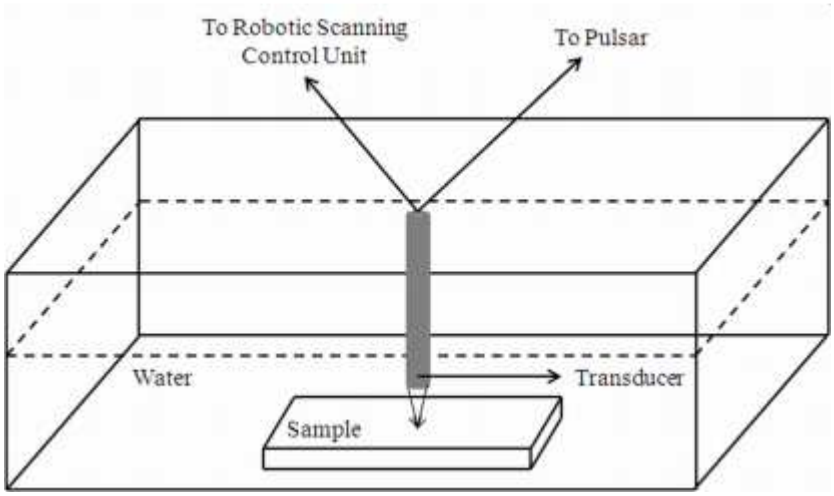

Figure 5.21: Schematic diagram of the ultrasonic immersion experimental set up

Results and Discussion: The sample was immersed in water bath and C scan was carried out using UT probe with 0.2 mm x 0.2 mm resolution. The back wall echo signal was considered for evaluation. The B scans over debonded and sound area were given in fig. 5.22 (a) and (b). There is no back wall signal received from the debonded area, since they will not allow the ultrasonic waves to pass through. Figure 5.23 shows the C scan image of the sample. From fig. 5.23 it is clearly seen that all the debonded areas were seen in C scan image. Areas 2 and 3 showed no difference. The sound area has high intensity values when compared to debonded areas because back wall echo is more in case of sound area where as there is no back wall echo in case of debonded area. The ultrasonic immersion test showed that all the areas are debonded and no kissing bond area is present. If the

kissing bond area is present, then part of ultrasonic waves would travel through it, which is not the case. Hence all the areas are completely debonded but with varying air gap thickness.

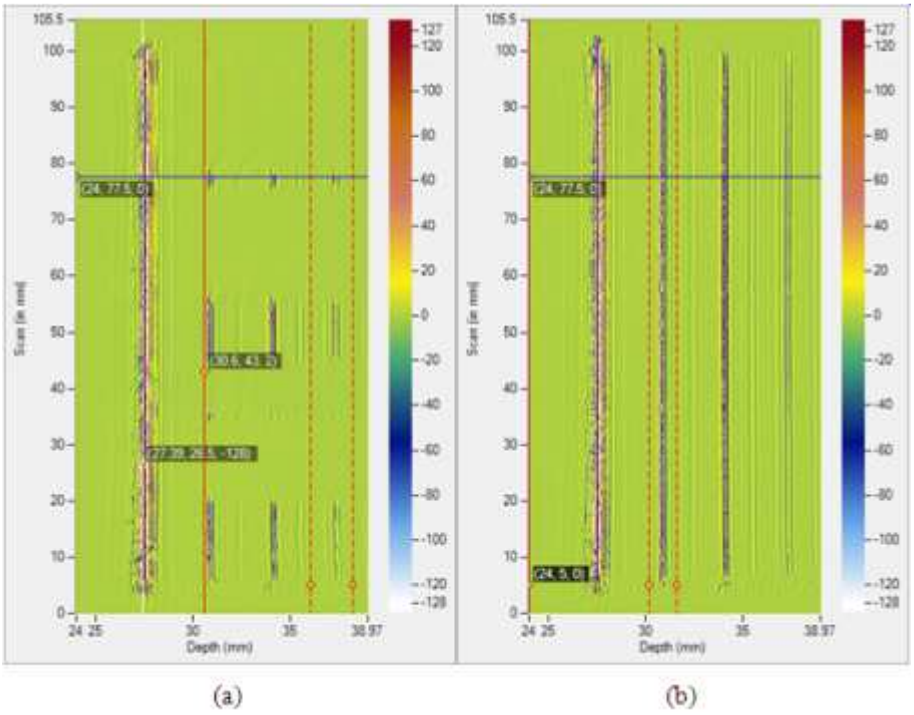

Figure 5.22: B Scan image taken over (a) debonded area (a) sound area

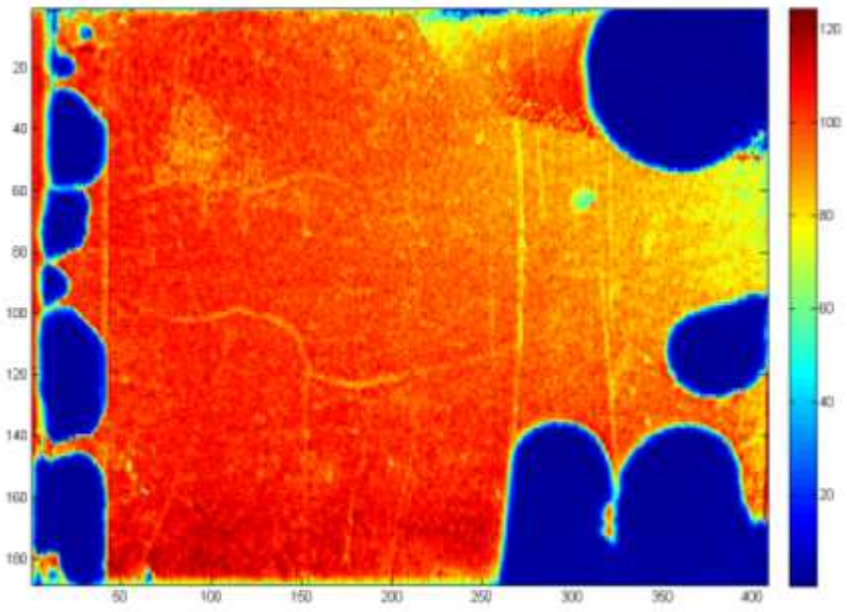

Figure 5.23: C Scan image of the coating obtained using ultrasonic immersion testing

To confirm the effect of air gap thickness on thermal signal, numerical modelling was carried out using ThermoCalc 6 L software. Ni-B coating on AISI grade 316 L was considered for analysis. Air gaps of varying thickness were introduced at the coating - substrate interface. The parameters used for the simulation are given in table 5.5. The temperature decay plot in logarithmic domain for air gap of thickness 5 µm, 50 µm and 500 µm are shown in fig. 5.24. The figure clearly shows that as the air gap of defect increases the strength of thermal signal. The analysis also showed that air gap of thickness 50 µm and 500 µm have almost similar temperature decay while 5 µm has deviated largely from other two air gaps. Hence if the air gap is very thin, then only thermal waves will pass through the defect otherwise they will diffuse around the defect.

	NiB	**Air**	**AISI 316 L**
Density (kg/m^3)	8,200	1.125	8990
Thermal Conductivity (W/m-K)	8	0.0257	16.2
Specific Heat (J/kg-K)	500	1005	500
Thermal Diffusivity (m^2/s)	$2x10^{-6}$	$22.73x10^{-6}$	$4x10^{-6}$

Table 5.4: Thermo physical properties of NiB – 316 L SS coating system

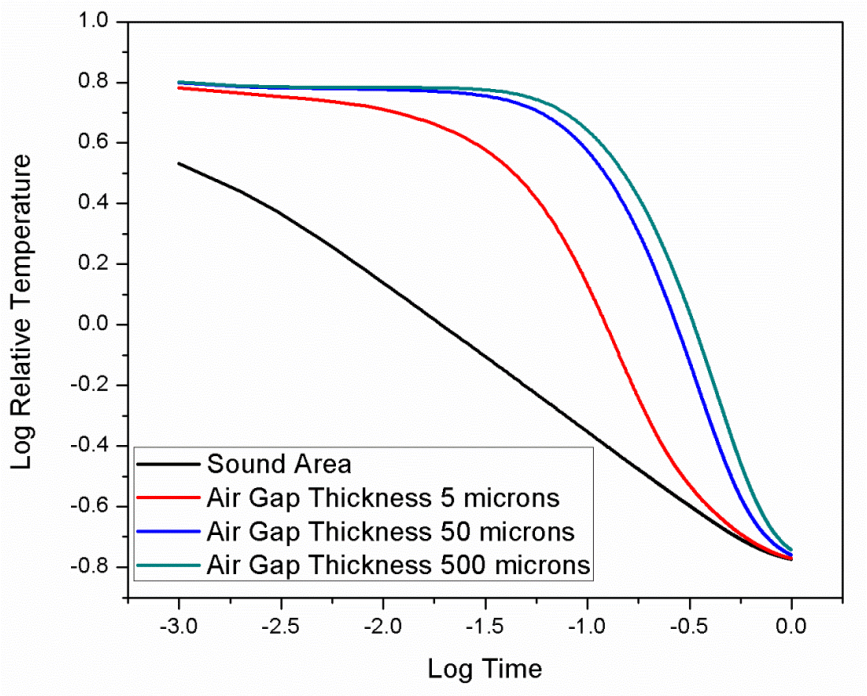

Figure 5.24: Temperature decay curve in logarithmic domain obtained from ThermoCalc 6L simulation for air gap of different thickness

In this chapter, a comparative study of PT and LT was carried out and the study revealed that LT gives superior SNR and better defect visualization. Two improve the defect detectability in PT, second derivative image was considered in which defect detectability was comparable with LT. Based on the experimental experience, PT and LT were used for brazing quality inspection of PFC and debond detection in coatings. Both PT and LT clearly revealed tiles which are not brazed in PFC. The results were validated using Hot and Cold Simulation technique. In coating inspection, PT and LT successfully detected the debonded areas. Thermographic signals were affected by air gap thickness which was confirmed using numerical simulation. The results were validated using Ultrasonic immersion technique.

CHAPTER 6
SUMMARY, CONCLUSION AND FUTURE DIRECTION

6.1 Summary and Conclusion

The reliability of any component or product is determined by its conformity to specifications and its ability to perform the required functions under stated conditions for stated period of time. This can best be achieved through stringent application of conventional and advanced non destructive testing and evaluation methods. In a strategic industry like nuclear, NDE practices start right from the initial inspection of raw materials, consumables through fabrication, pre service and in service inspection. A variety of conventional and advanced NDE methods and techniques are adopted such as liquid penetrant testing, radiography, ultrasonics, eddy current to ensure the fitness for purpose of the materials. Since nuclear materials have more stringent codal requirements, advanced NDE methods such as phased array, time of flight diffraction, computed tomography, magnetic Barkhausen noise etc are indispensable aids especially when challenging inspection situations arise. Infrared thermography is one such advanced NDE which is now an integral part of NDE applications in nuclear fuel cycle.

Austenitic stainless steels have been chosen as the major structural materials for the currently operating and planned Fast Breeder Reactors all over the world in view of their adequate high temperature mechanical properties, compatibility with liquid sodium coolant, good weld ability, availability of design data and above all the fairly vast and satisfactory experience in the use of these steels for high temperature service. In the Prototype Fast Breeder Reactor being setup at Kalpakkam, AISI type 316 SS has been used for main vessel, safety vessel fuel clad, subassembly etc. During the welding of thin

walled weldments such as Hexcan assembly or fuel pins defects such as cracks and micropores are likely. While large cracks can be easily detected tight cracks pose problems. Thus advanced NDE methods are needed to resolve such challenges. Infrared thermography is well suited for the detection of surface breaking defects where other NDE methods have limitations. The added advantage of IR thermography is the large area coverage and faster inspection times.

Over the last three decades, there has been a constant transformation on NDT & E techniques. From a qualitative go no approach, NDT became NDE including evaluation of defect size. With greater emphasis on fracture mechanics and need for complete dimensional details of defects NDE was required to completely characterize the defect including determine the depth of the defect. A review of literatures revealed that while extensive work has been done on the application of IR imaging especially active techniques for defect detection in composite materials, its application to metallic materials especially steels was far and few. Further no systematic work had been undertaken based on modeling and experimentation to establish the limits of detectability in an important structural material like SS. This motivated the author to take up this problem.

The first chapter gave a general overview of NDE, IR principles and its potential applications. The motivation behind the problem chosen, the international status and also objectives of the work were outlined clearly. The second chapter discussed the theoretical aspects of pulsed and lock in techniques, clearly identified the figures of merit for an infrared imaging system, material and experimental approach and theoretical and numerical tools used in the study. Chapter 3 discussed the defect characterization using PT including depth quantification by temperature contrast method, contrast derivative method, log first derivative method and log second derivative method. Chapter 4 describes the application of Lock in methods for defect characterization and highlighted the role of

optimum and blind frequency. A comparison of pulsed and lock in techniques is presented in chapter 5 with two interesting case studies. This Chapter presents in a nutshell the significance of the results. The areas that need further experimentation and possible future directions of the work are also highlighted.

Significant Results: The results presented in this thesis represent the first successful experimental attempt backed by modeling and simulation on the application of PT and LT for defect depth quantification and sizing in AISI grade 316 L stainless steel. In PT, log second derivative method was found to be independent of defect size and shape and predicts the defect depth with good accuracy. In LT, phase contrast method was used for depth quantification with proposed normalized parameter 'square root of defect area to depth ratio' (S), which is independent of defect size and shape. The sizing of defect using LT showed that, at frequencies, where thermal diffusion length is equal to thickness of material, the error in sizing measurement is minimum. A comparative study of PT and LT showed LT has superior SNR and defect detectability than PT. With the aid of signal process (TSR, 2^{nd} derivative image), defect detectability in PT is comparable to LT. Based on the laboratory experience gained on PT and LT, two important case studies are taken up, the brazing quality inspection of plasma facing components and the debond detection study in coatings. Both PT and LT successfully evaluated the brazing quality and debond detection in coatings.

In PT, four methods were considered for depth quantification, namely temperature contrast method, contrast derivative method, log first derivative method and log second derivative method. Thermal Signal Reconstruction (TSR) was carried to reduce the noise in thermal images sequences. Numerical and analytical simulations were carried out to validate the experimental results. Good correlation was observed between simulated and experimental results. The depth prediction study showed that the uncertainty associated

with temperature contrast method was high when compared to other techniques due to the lateral diffusion of heat. Contrast derivative method and log second derivative methods gave good accuracy in depth prediction. The study of effect of defect size and shape showed that temperature contrast method and log first derivative method were affected by the defect size and shape while contrast derivative and log second derivative methods were least affected. This behavior was mainly due to the effect of lateral diffusion of heat and explained by conducting 1 D analytical modelling. The study showed that in PT, any depth quantification method, if it predicts the peak time at early stage, the error associated with depth prediction would be less. The study showed that contrast derivative method and log second derivative methods were better method for depth prediction. Contrast derivative method has the inherent disadvantage of require of reference area for computing the contrast where as log second derivative method does not require any reference. Hence log second derivative method is best for depth prediction. Defect size was calculated by measuring the FWHM at different interval and plotting as a function of time. The intercept of the plot gives the actual size of the defect. The study showed that the sizing of defect could be predicted with good accuracy.

In LT, one should have idea about thermal diffusion length, blind frequency and phase inversion. The choice of frequency is important in LT. Two methods were discussed for depth quantifications, namely blind frequency method and phase contrast method. Blind frequency method was used in PPT for depth quantification, while in LT no detailed study has been reported. Defect length is directly proportional to the thermal diffusion length determined at blind frequency. Bennett and Patty (BP) model was carried out to evaluate the value of constant C. BP model is 1 D analytical modeling developed mainly for photo acoustic method. The analysis showed that the value of C is 1.57 for stainless steel system. Then experimental study was carried out. The study showed that the results

largely deviated from the theoretical prediction. The experimental blind frequency was less when compared to theoretical blind frequency. The value of C was found to be a function of defect depth. To understand the deviation from theoretical results, effect of defect size and shape on blind frequency was carried out. The study showed that blind frequency strongly depends on defect size and shape. Hence blind frequency is a function of defect depth, size and shape which was not considered in analytical simulation. Other factor affecting blind frequency is the choice of reference region. In theoretical analysis, semi-infinite, thermally thick reference is assumed, but in an real situation, the reference region has finite thickness. Hence blind frequency method is not an ideal parameter for depth quantification unless defect size and shape are taken in account. Phase contrast method is a good alternative for depth quantification and depth prediction using the calibration plot was observed to be accurate with errors associated being less than 10 %. The study of effect of defect size on phase contrast showed that phase contrast decreases as defect size decreases for a particular defect depth. To consider the effect of defect size, a normalized parameter was defined called defect size to depth ratio and the plot of defect size to depth ratio and phase contrast followed a trend which could be fitted with polynomial of order 3. But this parameter holds good for square defect not for rectangular shaped defect. To make the phase contrast independent of both size and shape, new parameter called square root of defect area to defect depth ratio (S) was considered. The experiment was conducted on different samples with defects of different size and shape and phase contrast was plotted as a function of S in a single plot. The plot followed a non linear trend and polynomial of order 4 was fitted and this plot was used as calibration plot. Then defect sizing was carried out using LT. FWHM was used to calculate the defect size. The defect size increases as frequency increases, at frequency 0.05 Hz, the error associated was least, since at this frequency the thermal diffusion length is equivalent to the sample

thickness. At this frequency the error associated was less than 4 %. The error was more for near surface defect when compared to deeper defect due to diffusion effects.

The comparison study between PT and LT showed that LT gives better defect visualization than PT. The SNR in case of LT was better than PT. The error associated in depth prediction and defect sizing incase of LT was better than PT. To improve the defect visualization in PT, second derivative image was considered. The second derivative image gives better defect visualization, comparable to LT, due to the early prediction where no lateral heat diffusion is present. The study showed that both PT and LT are capable of predicting defect depth and size with good accuracy. LT has superior defect detectability properties than PT.

Two case studies are considered, the brazing quality inspection of PFC and debond detection in coatings. The PFC samples were received from IPR, Ahmadabad for inspection of quality of brazing of graphite material to copper heat sink. The PFC was inspected using hot cold simulation in transmission mode and 5 tiles were identified as defective tiles. The PT was carried out and temperature decay plot showed that 3 tiles were detected as defective tiles. The second derivative image showed all the defective tiles. Two tiles, which were missing in the thermal image, were moderately brazed to the heats sink. Using LT, three tiles were clearly seen as defective while one was moderately brazed. 5^{th} tile was observed as defective, but the hot and cold simulation and temperature plot in PT showed it as good tile. Hence PT and LT both could differentiate between defective, moderately brazed and well brazed tiles. Another case study was debond detection in coating system. NiB coating on AISI grade 316 L SS with coating thickness 75 μm. Both PT and LT successfully detected debond. There were areas which had signals between debond and sound areas. This might be due to either varying air gap thickness or due to kissing bonds. To confirm the type of effect, ultrasonic immersion testing was

carried out. The ultrasonic immersion test showed that all were debonded area revealing that the variation in the signal was due to the varying air gap thickness. Numerical simulation of PT was carried out with varying air gap and the results clearly showed the air gap thickness has effect on thermal signal.

The present work clearly showed the ability of PT and LT for depth quantification and sizing. In both PT and LT, one should have knowledge about the material used for testing, experimental parameters and the camera type used. By considering all these aspects while performing experiment, LT and PT could be successfully used for defect characterization. Based on the experimental experience, two case studies were carried out. The study showed that PT and LT are excellent NDE tool for brazing quality inspection in PFC and debond detection in coatings.

6.2 Future Direction

It is well known that detailed characterization in the laboratory is the key to successful exploitation of the techniques in the field and industry. Any work is a start in itself. The application of pulsed and lock in techniques for defect detection and characterization is just a start. The focused studies have clearly revealed that while lock in techniques hold advantage, pulsed methods are also capable of defect depth quantification. The areas that can be explored further include

Pulsed Thermography

- In the present study, the flat bottom holes are used. But in real case, the air gap thickness will vary and the defects won't be flat bottom holes. Hence experiments has to carry out on defects of varying air gap thickness
- The application of PT in field for defect depth quantification and defect sizing

- Image processing applications for defect sizing and to reduce the heat diffusion effects to predict accurate size

Lock in Thermography

- Study has to be carried out on bind frequency. Depth quantification using blind frequency has to be done accounting for effect of defect size and shape
- Developing inverse problem for phase contrast, which is a direct problem
- Numerical simulations has to carry out in LT and both blind frequency and phase contrast methods have to be validated
- Defect sizing by image processing applications so to reduce the error in sizing measurement of near surface defects

References

1. Warren J. McGonnagle, Non Destructive Testing, 2nd Edition, Gordon and Breach, New York (1969)

2. R. Halmshaw, Non Destructive Testing, Edward Arnold, London (1987)

3. Baldev Raj and B. Venkatraman, Horst Czichos (Ed), *Handbook of Technical Diagnostics*, Chapter 4, Overview of Diagnostics and Monitoring Methods and Techniques, 43-68, Springer (2013)

4. Non Destructive Handbook Series Volume 2, 4-5, 7- 9, 3rd edition, ASNT, USA

5. X. P. Maldague, Theory and Practice of Infrared Technology for Non Destructive Testing, Wiley, New York (2001)

6. Xavier P. V. Maldague, Patrick O. Moore (Ed), Non Destructive Testing Handbook, 3rd Edition, Volume 3, ASNT, USA

7. Tuli S, Mulaveesala R, Frequency modulated wave thermography for non destructive testing, *QIRT Proceedings,* (2004) H 6.1-6.6

8. William Herschel, Experiments on the refrangibility of the invisible rays of the sun, *The Philosophical Magazine,* **8** (1880) 9-15

9. William Herschel, Experiments on the solar and terrestrial that occasion heat with a comparative view of the laws to which light and heat or rays which occasion them are subject, in order to determine whether they are the same or different, *The Philosophical Magazine,* **8** (1880) 16-29

10. T. I. Hurley, X. P. V. Maldague (Ed), *Infrared Methodology and Technology*, Part 2, Chapter 8, Infrared techniques for electric utilities, Gordon and Breach Publisher (1994) 265-318

11. R.V. Williams, Monitoring the condition of machinery, *Physics in Technology,* (1976) 166–171

12. Z. Ge, X. Du, L. Yang, Y. Yang, Y. Li, Y. Jin, Performance monitoring of direct air-cooled power generating unit with infrared thermography, *Applied Thermal Engineering,* **31** (2011) 418–424

13. ASTM International Standards, E 1934-99a, Standard guide for examining electrical and mechanical equipment with infrared thermography (2010)

14. D. Dumpert, X. P. V. Maldague (Ed), *Infrared Methodology and Technology*, Part 2, Chapter 7, Infrared techniques for Printed Circuit Board (PCB) Evaluation, Gordon and Breach Publisher (1994) 253-264

15. R. K. Vishwakarma, V. Mahule, M. Shahid, Fault diagnosing of a high density electronic card employing multiple power supplies using infrared thermography, *Journal of Non destructive Testing and Evaluation,* **7** (2008) 28–31

16. Rumsey M. A, Musial W., Application of infrared thermography nondestructive testing during wind turbine blade Tests, *Journal of Solar Energy Engineering,* **123** (2001) 271

17. Fausto Pedro García Márquez, Andrew Mark Tobias, Jesús María Pinar Pérez, Mayorkinos Papaelias, Condition monitoring of wind turbines: Techniques and methods, *Renewable Energy,* **46** (2012) 169-178

18. B.A. Chin, N.H. Madsen, J.S. Goodling, Infrared thermography for sensing the arc welding process, *Welding Journal,* **62** (1983) 227–234

19. Mansoor A. Khan, Neis H. Madsen, John S. Goodling, Bryan A. Chin, Infrared thermography as a control for the welding process, *Optical Engineering,* **25** (1986) 799-805

20. C.C. Doumanidis, D.E. Hardt, Simultaneous in-process control of heat affected zone and cooling rate during arc welding, *Welding Journal* **69** (1990) 186-196

21. H. C. Wikle III, S. Kottilingam, R. H. Zee, B. A. Chin, Infrared sensing technique for penetration depth control of the submerged arc welding process, *Journal of Materials Process and Technology,* **113** (2001) 228-233

22. W. H. Chen, B. A. Chin, Monitoring joint penetration using infrared sensing techniques, *Welding Journal* **69** (1990) 181-185

23. M. Menaka, M. Vasudevan, B. Venkatraman, Baldev Raj, Estimating bead width and depth of penetration during welding by infrared thermal imaging, *Insight,* **47** (2005) 564-568

24. G. Bruggemann, A. Mahrle, T. Benziger, Comparison of experimental determined and numerical simulated temperature fields for quality assurance at laser beam welding of steels and aluminium alloyings, *NDT & E International,* **33** (2000) 453–463

25. A. Lebar, M. Junkar, A. Poredos, M. Cvjeticanin, Method for online quality monitoring of AWJ cutting by infrared thermography, *CIRP Journal of Manufacturing Science and Technology,* **2** (2010) 170–175

26. S. Lee, J. Nam, W. Hwang, J. Kim, B. Lee, A study on integrity assessment of the resistance spot weld by infrared thermography, Procedia Engineering 10 (2011) 1748–1753

27. E. Grinzato, C. Meola (Ed.), *Infrared Thermography Recent Advances and Future Trends*, Chapter: State of the art and perspective of infrared thermography applied to building science, Bentham eBooks, (2012) 200–229

28. S. A. Ljungberg, X. P. V. Maldague (Ed), *Infrared Methodology and Technology*, Part 2, Chapter 6, Infrared techniques in buildings and structures: Operation and maintenance, Gordon and Breach Publisher (1994) 211-252

29. ASTM International Standards, D 4788 – 03, Standard Test Method for Detecting Delaminations in Bridge Decks Using Infrared Thermography (2007)

30. ASTM International Standards, C1060 – 11a, Standard Practice for Thermographic Inspection of Insulation Installations in Envelope Cavities of Frame Buildings

31. ASTM International Standards, C1153 – 10, Standard Practice for Location of Wet Insulation in Roofing Systems Using Infrared Imaging

32. J. W. K. Louis, M. Gautherie, Long term assessment of breast cancer risk by thermal imaging, *Progress in Biological and Clinical Research*, (1982) 279–301

33. N. Arora, D. Martins, D. Ruggerio, E. Tousimis, A. J. Swistel, M. P. Osborne, R. M. Simmons, Effectiveness of a noninvasive digital infrared thermal imaging system in the detection of breast cancer, *The American Journal of Surgery,* **196** (2008) 523–526

34. P. I. Branemark, S. E. Fagerberg, L. Langer, J. Save-Soderbergh, Infrared thermography in diabetes mellitus a preliminary study, *Diabetologia,* **3** (1967) 529-532

35. S. Sivanandam, M. Anburajan, B. Venkatraman, M. Menaka, D. Sharath, Medical thermography: a diagnostic approach for type 2 diabetes based on non-contact infrared thermal imaging, *Endocrine,* **42** (2012) 343-351

36. P. Morgan, A. Tullo, N. Efron, Infrared thermography of the tear film in dry eye, *Eye (London, England,)* **9** (1995) 615–618

37. R. A. Thomas, K. E. Donne, M. Clement, M. N. Kiernan, Optimized laser application in dermatology using infrared thermography, *Proceedings of SPIE*, **4710** (2002) 424–435

38. B. R. Mason, A. J. Graff, S. P. Pegg, Colour thermography in the diagnosis of the depth of burn injury, *Burns,* **7** (1981) 197–202

39. W. J. Parker, R. J. Jenkins, C. P. Butler, G. L. Abbott, Flash method of determining thermal diffusivity, heat capacity and thermal conductivity, *Journal of Applied Physics,* **32** (1961) 1679-1684

40. Robert D. Cowan, Pulse method of measuring thermal diffusivity at high temperatures, *Journal of Applied Physics,* **34** (1963) 962-963

41. K. B. Larson, Karl Koyama, Correction for finite pulse time effects in very thin samples using the flash method of measuring thermal diffusivity, *Journal of Applied Physics,* **38** (1967) 465-474

42. Kazimierz Rozniakowski, Tomasz W. Wojtatowicz, Thermal diffusivity of building materials measured by the laser flash method, *Journal of Materials Science Letters,* **5** (1986) 995-996

43. Daniel L. Balageas, Thermal diffusivity measurement by pulsed methods, *High Temperatures-High Pressures,* **21** (1989) 85-96

44. J. E. Graebner, Measurement of thermal diffusivity by optical excitation and infrared detection of a transient thermal grating, *Review of Scientific Instruments*, **66** (1995) 3903-3906

45. Robert L. McMasters, Modeling flash diffusivity experiments in two dimensions for thick samples, *Journal of Thermophysics and Heat Transfer,* **23** (2009) 399-403

46. P. Cielo, Pulsed photothermal evaluation of layered materials, *Journal of Applied Physics,* **56** (1984) 230-234

47. D. L. Balageas, J. C. Krapez, P. Ceilo, Pulsed photothermal modeling of layered materials, *Journal of Applied Physics,* **59** (1986) 348-357

48. S. K. Lau, D. P. Almond, P. M. Patel, Transient thermal wave techniques for the evaluation of surface coatings, *Journal of Physics D: Applied Physics,* **24** (1991) 428-436

49. U. Netzelmann, G. Walle, High speed thermography of thin metallic coatings, *AIP Conference Proceedings,* **463** (1998) 401-403

50. Golam Newaz, Xiaoqun Chen, Progressive damage assessment in thermal barrier coatings using thermal wave imaging technique, *Surface and Coatings Technology,* **190** (2005) 7-14

51. Jeffrey I. Eldridge, Charles M. Spuckler, Monitoring Delamination Progression in Thermal Barrier Coatings by Mid-Infrared Reflectance Imaging, *International Journal of Applied Ceramic Technology,* **3** (2006) 94-104

52. Otto Renius, Laser illumination for infrared nondestructive testing, *Materials Evaluation*, (1973), 80-84

53. P. V. McLaughlin Jr., M. G. Mirchandani, P. V. Ciekurs, Infrared thermographic flaw detection in composite laminates, *Journal of Engineering Materials and Technology,* **109** (1987) 146-150

54. V. Vavilov, Infrared nondestructive testing of bonded structures: Aspects of theory and practice, *British Journal of NDT,* **22** (1980) 175-183

55. C. M. Sayers, Detectability of defects by thermal nondestructive testing, *British Journal of NDT,* (1984) 28-33

56. S. F. Burch, J. T. Burton and S. J. Cocking, Detection of defects by transient thermography: A comparison of predictions from two computer codes with experimental results, *British Journal of NDT,* (1984) 36-44

57. P. Cielo, X. Maldague, A. A. Deom, R. Lewak, Thermographic nondestructive evaluation of industrial materials and structures, *Materials Evaluation,* **45** (1987) 452-460

58. D. L. Balageas, A. A. Deom, D. M. Boscher, Characterization of nondestructive testing of carbon epoxy composites by a pulsed photothermal method, *Materials Evaluation,* **45** (1987) 461-465

59. W. N. Reynolds, Inspection of laminates and adhesive bonds by pulse video thermography, *NDT International,* **21** (1988) 229-232

60. Y. A. Wong, R. C. Thomas, G. F. Hawkins, Surface and subsurface structure of solids by laser photoacoustic spectroscopy, *Applied Physics Letters,* **32** (1978) 538-539

61. S. K. Lau, D. P. Almond, J. M. Milne, A quantitative analysis of pulsed video thermography, *NDT & E International,* **24** (1991), 195-202

62. V. Vavilov, X. Maldague, B. Dufort, F. Robitaille, J. Picard, Thermal nondestructive testing of carbon epoxy composites: Detailed analysis and data processing, *NDT & E International,* **26** (1993), 85-95

63. J. G. Sun, Analysis of pulsed thermography methods for defect depth prediction, *Journal of heat transfer,* **128** (2006) 329-338

64. Harry I. Ringermacher, Raymond J. Archacki Jr., William A. Veronesi, Nondestructive Testing: Transient depth thermography, (1998) US Patent No. 5,711,603

65. C. Deemer, J. G. Sun, W. A. Ellingson, S. Short, Front flash thermal imaging characterization of continuous fiber ceramic composites, *Ceramic Engineering and Science Proceedings,* **20** (1999) 317-324

66. N. P. Avdelidis, B. C. Hawtin, D. P. Almond, Transient thermography in the assessment of defects of aircraft composites, *NDT & E International,* **36** (2003), 433-439

67. Zhi Zheng, Chunguang Li, Ning Tao, Lichun Feng, Cunlin Zhang, Depth prediction of non air interface defect using pulsed thermography, *NDT & E International,* **48** (2012), 39-45

68. D. P. Almond, S. K. Lau, Defect sizing by transient thermography I: An analytical treatment, *Journal of Physics D: Applied Physics,* **27** (1994) 1063-1069

69. M. B. Saintey, D. P. Almond, Dfect sizing by transient thermography II: A numerical treatment, *Journal of Physics D: Applied Physics,* **28** (1995) 2539-2546

70. D. P. Almond, S. K. Lau, Edge effects and a method of defect sizing for transient thermography, *Applied Physics Letters,* **62** (1993) 3369-3371

71. A. R. Hanzah, P. Delpech, M. B. Saintey, D. P. Almond, The experimental investigation of defect sizing by transient thermography, *Insight,* **38** (1996) 167-171

72. Steven M. Shepard, , James R. Lhota, Bruce A. Rubadeux, David Wang, Tasdiq Ahmed, Reconstruction and enhancement of active thermographic image sequences, *Optical Engineering,* **42** (2003) 1337-1342

73. S. M. Shepard, Y. Hou, T. Ahmed, J. R. Lhota, Reference free interpretation of flash thermography data, *Insight,* **48** (2006), 298-301

74. S. M. Shepard, T. Ahmed, B. A. Rubadeux, D. Wang, J. R. Lhota, Synthetic processing of pulsed thermographic data for inspection of turbine components, *Insight,* **43** (2001) 587-589

75. Richard E. Martin, Andrew L. Gyekenyesi, Steven M. Shepard, Interpreting the results of pulsed thermography data, *Materials Evaluation,* **61** (2003) 611-616

76. N. Rajic, Principal component thermography, (2002) DSTO technical report TR-345

77. N. Rajic, Principal component thermography for flaw contrast enhancement and flaw depth characterization in composite structures, *Composite Structures,* **58** (2002) 521-528

78. V. P. Vavilov, D. A. Nesteruk, V. V. Shiryaev, W. Swiderski, Application of principal component analysis in dynamic thermal testing data processing, *Russian Journal of Nondestructive Testing,* **44** (2008) 509-516

79. C. Ibarra-Castanedo, D. Gonzalez, M. Klein, M. Pilla, S. Vallerand, X. Maldague, Infrared image processing and data analysis, *Infrared Physics and Technology,* **46** (2004) 75-83

80. S. Marinetti, E. Grinzato, P. G. Bison, E. Bozzi, M. Chimenti, G. Pieri, O. Salvetti, Statistical analysis of IR thermographic sequences by PCA, *Infrared Physics and Technology,* **46** (2004) 85-91

81. M. A. Omar, R. Parvataneni, Y. Zhou, A combined approach of self referencing and principal component thermography for transient, steady and selective heating scenarios, *Infrared Physics and Technology,* **53** (2010) 358-362

82. V. Feuillet, L. Ibos, M. Fois, J. Dumoulin, Y. Candau, Defect detection and characterization in composite materials using square pulse thermography coupled with singular value decomposition analysis and thermal quadrupole modeling, *Infrared Physics and Technology,* **51** (2012) 58-67

83. Allan Rosencwaig, Allen Gersho, theory of the photoacoustic effect with solids, *Journal of Applied Physics,* **47** (1976) 64-69

84. Allan Rosencwaig, Theoretical aspects of photoacoustic spectroscopy, *Journal of Applied Physics,* **49** (1978) 2905-2910

85. F. Alan McDonald, Grover C. Wetsel Jr., Generalized theory of the photoacoustic effect, *Journal of Applied Physics,* **49** (1978) 2313-2322

86. M. Luukkala, A. Penttinen, Photoacoustic microscope, *Electronics Letters,* **15** (1979) 325-326

87. F. Alan McDonald, Photoacoustic effect and the physics of wave, *American Journal of Physics,* **48** (1980) 41-47

88. Y. H. Wong, R. L. Thomas, G. F. Hawkins, Surface and subsurface structure of solids by laser photoacoustic spectroscopy, *Applied Physics Letters,* **32** (1978) 538-539

89. Y. H. Wong, R. L. Thomas, J. J. Pouch, Subsurface structures of solids by scanning photoacoustic microscopy, *Applied Physics Letters,* **35** (1979) 368-369

90. R. L. Thomas, J. J. Pouch, Y. H. Wong, L. D. Favro, P. K. Kuo, Subsurface flaw detection in metals by photoacoustic microscopy, *Journal of Applied Physics,* **51** (1980) 1152-1156

91. G. Busse, Allan Rosencwaig, Subsurface imaging with photoacoustics, *Applied Physics Letters,* **36** (1980) 815-816

92. G. Busse, Optoacoustic phase angle measurement for probing a metal, *Applied Physics Letters*, **35** (1979) 759-760

93. C. A. Bennett Jr., R. R. Patty, Thermal wave interferometry: A potential application of the photoacoustic effect, *Applied Optics,* **21** (1982) 49-54

94. G. Busse, Photothermal transmission probing of a metal, *Infrared Physics,* **20** (1980) 419-422

95. Per-Erik Nordal, Svein Otto Kanstad, Photothermal radiometry, *Physica Scripta,* **20** (1979) 659-662,

96. Svein Otto Kanstad, Per-Erik Nordal, Experimental aspects of photothermal radiometry, *Canadian Journal of Physics,* **64** (1986) 1155-1164

97. Gerd Busse, Optoacoustic and photothermal material inspection techniques, *Applied Optics,* **21** (1982) 107-110

98. G. Busse, P. Eyerer, Thermal wave remote and nondestructive inspection of polymers, *Applied Physics Letters,* **43** (1983) 355-357

99. A. C. Boccara, D. Fournier, J. Badoz, Thermo-optical spectroscopy: Detection by the mirage effect, *Applied Physics Letters,* **36** (1980) 130-132

100. J. C. Murphy, L. C. Aamodt, Photothermal spectroscopy using optical beam probing: Mirage effect, *Journal of Applied Physics,* **51** (1980) 4580-4588

101. L. C. Aamodt, J. C. Murphy, Photothermal measurements using a localized excitation source, *Journal of Applied Physics,* **52** (1981) 4903-4914

102. L. C. Aamodt, J. C. Murphy, Thermal effects in photothermal spectroscopy and photothermal imaging, *Journal of Applied Physics,* **54** (1983) 581-591

103. L. J. Inglehart, K. R. Grice, L. D. Favro, P. K. Kuo, R. L. Thomas, Spatial resolution of thermal wave microscope, *Applied Physics Letters,* **43** (1983) 446-448

104. F. Lepoutre, D. Fournier, A. C. Boccara, Nondestructive control of weldings using the mirage detection, *Journal of Applied Physics,* **57** (1985) 1009-1015

105. G. Busse, D. Wu, W. Karpen, Thermal wave imaging with phase sensitive modulated thermography, *Journal of Applied Physics,* **71** (1992) 3962-3965

106. J. C. Krapez, Compared performances of four algorithms used for modulation thermography, *Proceedings of QIRT*, (1998) 148-153

107. Liu Junyan, , Wang Yang, Dai Jingmin, Research on thermal wave processing of lock in thermography based on analyzing image sequences for NDT, *Infrared Physics and Technology,* **53** (2010) 348-357

108. J. Jaarinen, M. Luukkala, Numerical analysis of thermal waves in stratified media for non-destructive purpose, *Journal De Physique,* **44** (1983) C6-503 – C6-508

109. T. T. N. Lan, U. Seidel, H. G. Walther, Theory of microstructural depth profiling by photothermal measurements, *Journal of Applied Physics,* **77** (1995) 4739-4745

110. G. Goch, M. Reigl, Application of the finite-element method and the finite difference method to photothermal inspection, *Journal of Applied Physics,* **79** (1996) 9084-9089

111. S. Aithal, G. Rousset, L. Bertrand, Photoacoustic characterization of subsurface defects in plasma sprayed coatings, *Thin Solid Films,* **119** (1984) 153-158

112. D. P. Almond, P. M. Patel, I. M. Pickup, H. Reiter, An evaluation of the suitability of thermal wave interferometry for the testing of plasma sprayed coatings, *NDT International,* **18** (1985) 17-24

113. P. M. Patel, D. P. Almond, Thermal wave testing of plasma sprayed coatings and a comparison of the effects of coating microstructure on the propagation of thermal and ultrasonic waves, *Journal of Materials Science,* **20** (1985) 955-966

114. D. P. Almond, P. M. Patel, H. Reiter, the testing of plasma sprayed coatings by thermal wave interferometry, *Materials Evaluation,* **45** (1987) 471-475

115. P. M. Patel, D. P. Almond, H. Reiter, Thermal wave detection and characterization of sub surface defects, *Applied Physics B*, **43** (1987) 9-15

116. D. Wu, W. Karpen, K. Haupt, H. G. Walther, G. Busse, Application of phase sensitive thermography for nondestructive evaluation, *Journal De Physique,* **04** (1994) C7-567 – C7-570

117. G. Giorleo, C. Meola, A. Squillace, Analysis of defective carbon epoxy by means of Lock-in thermography, *Research in Nondestructive Evaluation,* **12** (2000) 241-250

118. Carosena Meola, Giovanni M. Carlomagno, Antonino Squillace, Giuseppe Giorleo, The use of infrared thermography for nondestructive evaluation of joints, *Infrared Physics and Technology,* **46** (2004) 93-99

119. Takahide Sakagami, Shiro Kubo, Development of a new nondestructive testing technique for quantitative evaluations of delamination defects in concrete structures bases on phase delay measurement using lock in thermography, *Infrared Physics and Technology,* **43** (2002) 311-316

120. Manyong Choi, Kisoo Kang, Jeonghak Park, Wontae Kim, Koungsuk Kim, Quantitative determination of a subsurface defect of reference specimen by lock in infrared thermography, *NDT & E International,* **41** (2008) 119-124

121. Liu Junyan, Tang Qingju, Liu Xun, Wang Yang, Research on the quantitative analysis of subsurface defects for nondestructive testing by lock in thermography, *NDT & E International,* **45** (2012) 104-110

122. C. Wallbrink, S. A. Wade, and R. Jones, The effect of size on the quantitative estimation of defect depth in steel structures using lock-in thermography, *Journal of Applied Physics,* **101** (2007) 104907 1-8

123. W. Bai, B. S. Wong, Photothermal models for lock in thermographic evaluation of plates with finite thickness under convection condition, *Journal of Applied Physics,* **89** (2001) 3275-3282

124. W. Bai, B. S. Wong, Evaluation of defects in composite plates under convective environments using lock-in thermography, *Measurement Science and Technology,* **12** (2001) 142-150

125. Sung Quek, Darryl Almond, Luke Nelson, Tim Barden, A novel and robust thermal wave signal reconstruction technique for defect detection in lock in thermography, *Measurement Science and Technology,* **16** (2005) 1223-1233

126. Simon Pickering, Darryl Almond, Matched excitation energy comparison of the pulse and lock in thermography NDE techniques, *NDT & E International,* **41** (2008) 501-509

127. Krishnendu Chatterjee, Suneet Tuli, Simon G. Pickering, Darryl P. Almond, A comparison of the pulsed, lock in and frequency modulated thermography nondestructive evaluation techniques, *NDT & E International,* **44** (2011) 655-667

128. Ahsan Mian, Xiaoyan Han, Sarwar Islam, Golam Newaz, Fatigue damage detection in graphite/epoxy composites using sonic infrared imaging technique, *Composites Science and Technology,* **64** (2004) 657-666

129. R. Montanini, F. Freni, Investigation of heat generation sources in sonic infrared thermography using laser Doppler vibrometry, Presented at 11th International Conference on Quantitative Infrared Thermography held at Naples, Italy (2012)

130. J. Rantala, D. Wu, G. Busse, NDT of polymer materials using lock in thermography with water coupled ultrasonic excitation, *NDT&E International,* **31** (1998) 43-49

131. X. Maldague, S. Marinetti, Pulse phase infrared thermography, *Journal of Applied Physics,* **79** (1996) 2694-2698

132. Sergio Marinetti, Yuri A. Plotnikov, William P. Winfree, Alberto Braggiotti, Pulse phase thermography for defect detection and visualization, *SPIE*, **3586** (1999) 230-238

133. Clemente Ibarra-Castanedo, Xavier P. V. Maldague, Pulsed phase thermography reviewed, *Quantitative Infrared Thermography Journal,* **1** (2004) 47-70

134. Clemente Ibarra-Castanedo, Xavier P. V. Maldague, Interactive methodology for optimized defect characterization by quantitative pulsed phase thermography, *Research in Non Destructive Evaluation,* **16** (2005) 175-193

135. X. Maldague, F. Galmiche, A. Ziadi, Advances in pulsed phase thermography, *Infrared Physics and Technology,* **43** (2002) 175-181

136. C. Ibarra-Castanedo, X. Maldague, Defect depth retrieval from pulsed phase thermographic data on Plexiglas and Aluminum samples, *Proceedings of SPIE*, **5405** (2004) 348-355

137. Clemente Ibarra-Castanedo, Nicolas P. Avdelidis, Xavier P. Maldague, Quantitative pulsed phase thermography applied to steel plates, *Proceedings of SPIE*, **5782** (2005) 342-351

138. L. C. Aamodt, J. W. Maclachlan Spicer, J. C. Murphy, Analysis of characteristic thermal transit times for time resolved infrared radiometry studies of multilayered coatings, *Journal of Applied Physics,* **68** (1990) 6087-6098

139. Robert Osiander, Jane W. M. Spicer, Time resolved infrared radiometry with step heating. A review, *Revue Générale de Thermique,* **37** (1998) 680-692

140. Mulaveesala Ravibabu, Suneet Tuli, Digitized frequency modulated thermal wave imaging for nondestructive testing, *Materials Evaluation*, **63** (2005) 1046-1050

141. Suneet Tuli, Ravibabu Mulaveesala, Defect detection by pulse compression in frequency modulated thermal wave imaging, *Quantitative Infrared Thermography Journal,* **2**(2005) 41-54

142. Ravibabu Mulaveesala, Suneet Tuli, Theory of frequency modulated thermal wave imaging for nondestructive subsurface defect detection, *Applied Physics Letters,* **89** (2006) 191913 1-3

143. Ravibabu Mulaveesala, Prem Pal, Suneet Tuli, Interface study of bonded wafers by digitized linear frequency modulated thermal wave imaging, *Sensors and Actuators A,* **128** (2006) 209-216

144. R. Mulaveesala, V. S. Ghali, V. Arora, Applications of non-stationary thermal wave imaging methods for characterisation of fibre-reinforced plastic materials, *Electronics Letters,* **49** (2013) 118-119

145. V. S. Ghali, R. Mulaveesala, M. Takei, Frequency-modulated thermal wave imaging for non-destructive testing of carbon fiber-reinforced plastic materials, *Measurement Science and Technology,* **22** (2011) 104018 1-4

146. Ravibabu Mulaveesala, Jyani Somayajulu Vaddi, Pushpraj Singh, Pulse compression approach to infrared nondestructive characterization, *Review of Scientific Instrument,* **79** (2008) 094901 1-6

147. V. S. Ghali, S. S. B. Panda, R. Mulaveesala, Barker coded thermal wave imaging for defect detection in carbon fibre-reinforced plastics, *Insight,* **53** (2011) 621-624

148. G. V. Subbarao, R. Mulaveesala, Quadratic frequency modulated thermal wave imaging for non-destructive testing, *Progress in Electromagnetics Research M,* **26** (2012) 11-22

149. Baldev Raj, Materials and manufacturing technologies for sodium cooled fast reactors and associated fuel cycle: Innovation and Maturity, Energy Procedia, 7 (2011) 186-198

150. S. C. Chetal, P. Chellapandi, P. Puthiyavinayagam, S. Raghupathy, V. Balasubramaniyan, P. Selvaraj, P. Mohanakrishnan, Baldev Raj, Current status of fast reactors and future plans in India, Energy Procedia, 7 (2011) 64-73

151. Burton Bernard, ABC's of Infrared, W. Foulsham & Co. Ltd, England (1970)

152. V. P. Vavilov, Non Destructive Testing Handbook – Thermal/Infrared Testing, Volume 5 (Book 1), Spektr, Moscow (2009)

153. M. Vollmer, K. P. Mollmann, Infrared Thermal Imaging – Fundamentals, Research and Applications, WILEY – VCH Verlag GmbH & Co. Germany (2010)

154. Standard Terminology for Nondestructive Examination, ASTM Standard E1316-10a

155. B. Venkatraman and Baldev Raj, Performance parameters for thermal imaging system, *Insight,* **45** (2003) 531-535

156. Colin Hockings, Infrared Equipment Terminology, *Materials Evaluation,* (1997) September 955-957

157. Darryl Almond and Pravin Patel, Photothermal science and techniques, Chapmn & Hall, London (1996)

158. M. A. J. Angstrom, New method of determining the thermal conductivity of bodies, *The Philosophical Magazine,* **25** (1863) 130-142

159. Datong Wu, Gred Busse, Lock in thermography for nondestructive evaluation of materials, *Revue Générale de Thermique* **37** (1998) 693-703

160. ThermoCalc 6L User Manual

161. Steven M Shepard, Temporal noise reduction, Compression and analysis of thermographic image data sequences, US Patent No. 6,516,084 B2 (2002)

162. J. G. Sun, Method for analyzing multi-layer materials from one-sided pulsed thermal imaging, US Patent No. 7,769,201 B2 (2010)

163. J. C. Krapez, D. Balageas, A. Deom and F. Lepoutre, Early detection by stimulated infrared thermography. Comparison with ultrasonic and Holo/Shearography *NATO ASI Series – Advances in Signal Processing for Nondestructive Evaluation of Materials,* **262** (1994) 303-321

164. Xiaoyan Han, L. D. Favro, P. K. Kuo and R. L. Thomas, Early-time pulse-echo thermal wave imaging *Review and Progress of Quantitative Nondestructive Evaluation.* **15A** (1996) 519-524

165. D. J. Roth, J. R. Bodis and C. Bishop, Thermographic imaging of high temperature composite materials - A defect detection study *Research in Nondestructive Evacuation.* **9** (1997) 147-169

166. M. Menaka, D. Sharath, B. Venkatraman and Baldev Raj, Precise depth detection of EDM notches by lock-in thermography, *Journal of Non destructive Testing and Evaluation*, **8** (2009), 15-18

167. Leon Kaufman, David M. Kramer, Lawrence E. Crooks, Douglas A. Ortendahl, Measuring signal to noise ratio in MR imaging, *Radiology,* **173** (1989) 265-267

168. Artsimovich, L. A., Tokamak Devices, *Nuclear Fusion* **12** (1972) 215–251

169. Weston M. Stacey Jr., Fusion Reactor Development: A Review, *Advances in Nuclear Sciences and Technology,* **15** (1983) 129-221

170. R. Tivey, M. Akiba, D. Driemeyer, I. Mazul, M. Merola, M. Ulrickson, ITER R&D: Vacuum Vessel and In-Vessel Components: Divertor Cassette, *Fusion Engineering and Design* **55** (2001) 219–229

171. M. Nakahira, H. Takahashi, K. Koizumi, M. Onozuka and K. Ioki, Progress and achievements of R&D activities for the ITER vacuum vessel, *Nuclear Fusion,* **41** (2001) 375-380

172. J. Linke, Plasma facing materials and components for future fusion devices – development, characterization and performance under fusion specific loading conditions, *Physica Scripta,* **T123** (2006) 45-53

173. R Causey, K Wilson, T Venhaus, W R. Wampler, Tritium retention in tungsten exposed to intense fluxes of 100 eV tritons, *Journal of Nuclear* Materials, **266-269** (1999) 467-471

174. R. Tivey, T. Ando, A. Antipenkov, V. Barabash, S. Chiocchio, G. Federici, C. Ibbott, R. Jakeman, G. Janeschitz, R. Raffray, M. Akiba, I. Mazul, H. Pacher, M. Ulrickson, G. Vieider, ITER divertor, design issues and research and development, *Fusion Engineering and Design,* **46** (1999) 207-220

175. Th Koppitz, G Pintsuk, U Reisgen, J Remmel, T Hirai, R Sievering, Y Rojas and V Casalegno, High-temperature brazing for reliable tungsten–CFC joints, *Physica Scripta,* **T128** (2007) 175-181

176. D. Satas, Coatings Technology Handbook (1991), Marcel Dekker Inc, New York

177. Frederick Adolph Lowenheim, Modern Electroplating, 3rd edition (1974), Electrochemical Scociety

178. T. S. N. Sankara Narayanan, K. Krishnaveni, S. K. Seshadri, Electroless Ni-P/Ni-B duplex coatings: Preparation and evaluation of microhardness, wear and corrosion resistance, *Materials Chemistry and Physics*, **82** (2003) 771-779

179. B. Oraon, G. Majumdar, B. Ghosh, Improving hardness of electroless Ni-B coatings using optimized deposition conditions and annealing, *Materials and Design*, **29** (2008) 1412-1418

180. Y. W. Riddle, T. O. Bailer, Friction and wear reduction via an Ni-B electroless bath coating for metal alloys, *JOM*, **57** (2005) 40-45

181. F. Delaunois, J. P. Petitjean P. Lienard, M. Jacob Duliere, Autocatalytic electroless nickel-boron plating on light alloys, *Surface and Coatings Technology*, **124** (2000) 201-209

182. R. C. Agarwala, Vijaya Agarwala, Electroless alloy/composite coatings: A review, *Sadhana*, **28** (2003) 475-493

183. F. Bastianini, A. Di Tommaso and G. Pascale, Ultrasonic non-destructive assessment of bonding effects in composite structural strengthenings, *Composite Structure*, **53** (2001) 463-467

184. Shi-Chang Wooh and Isaac M. Daniel, Real time ultrasonic monitoring of fiber-matrix debonding in ceramic-matrix composite, *Mechanics of Materials*, **17** (1994) 379-388

185. Ultrasonic testing of aerospace materials, Practice No. PT-TE-1422, NASA 1-6

186. T. Kundu, A. Maji. T. Ghosh, K. Maslov, Detection of kissing bonds by lamb waves, *Ultrasonics*, **35** (1998) 573-580